Localization of deformation in a non-collisional subduction orogen: the roles of dip geometry and plate strength on the evolution of the broken Andean foreland, Sierras Pampeanas, Argentina

Michaël Pons[1,2], Constanza Rodriguez Piceda[2,3,4], Stephan V. Sobolev[2,4], Magdalena Scheck-Wenderoth[5,6], and Manfred R. Strecker[2]

[1]Helmholtz Centre Potsdam, GFZ German Research Centre for Geosciences
[2]Universität Potsdam, Institut für Geowissenschaften, Germany
[3]University of Plymouth, School of Geography, Earth and Environmental Sciences, United Kingdom
[4]Helmholtz Centre Potsdam GFZ German Research Centre for Geosciences
[5]Helmholtz Centre Potsdam, GFZ German Research Centre For Geosciences
[6]RWTH Aachen University, Aachen, Germany

January 24, 2023

Abstract

The non-collisional subduction margin of South America is characterized by different geometries of the subduction zone and upper-plate tectono-magmatic provinces. The localization of deformation in the southern Central Andes (29°S–39°S) has been attributed to numerous factors that combine the properties of the subducting oceanic Nazca plate and the continental South American plate. In this study, the present-day configuration of the subducting oceanic plate and the continental upper plate were integrated in a data-driven geodynamic workflow to assess their role in determining strain localization within the upper plate of the flat slab and its southward transition to a steeper segment. The model predicts two fundamental processes that drive deformation in the Andean orogen and its foreland: eastward propagation of deformation in the flat-slab segment by a combined bulldozing mechanism and pure-shear shortening that affects the broken foreland and simple-shear shortening in the fold-and-thrust belt of the orogen above the steep slab segment. The transition between the steep and subhorizontal subduction segments is characterized by a 370-km-wide area of diffuse shear, where deformation transitions from pure to simple shear, resembling the transition from thick to thin-skinned foreland deformation in the southern Sierras Pampeanas. This pattern is controlled by the change in dip geometry of the Nazca plate and the presence of mechanically weak sedimentary basins and inherited faults.

Localization of deformation in a non-collisional subduction orogen: the roles of dip geometry and plate strength on the evolution of the broken Andean foreland, Sierras Pampeanas, Argentina

Michaël Pons*,** (1,2), Constanza Rodriguez Piceda* (1,2,3), Stephan V. Sobolev (1.2), Magdalena Scheck-Wenderoth (1,4), Manfred R. Strecker (1)

(1) Universität Potsdam, Institut für Geowissenschaften, Germany, (2) Helmholtz-Zentrum Potsdam GFZ - Deutsches GeoForschungsZentrum, Germany (3) Plymouth University, School of Geography Earth and Environmental Sciences, United Kingdom (4) RWTH Aachen University, Aachen, Germany

**these authors contributed equally to this work*

*** Corresponding author: Michaël Pons (ponsm@gfz-potsdam.com)*

Abstract

The non-collisional subduction margin of South America is characterized by different geometries of the subduction zone and upper-plate tectono-magmatic provinces. The localization of deformation in the southern Central Andes (29°S–39°S) has been attributed to numerous factors that combine the properties of the subducting oceanic Nazca plate and the continental South American plate. In this study, the present-day configuration of the subducting oceanic plate and the continental upper plate were integrated in a data-driven geodynamic workflow to assess their role in determining strain localization within the upper plate of the flat slab and its southward transition to a steeper segment. The model predicts two fundamental processes that drive deformation in the Andean orogen and its foreland: eastward propagation of deformation in the flat-slab segment by a combined bulldozing mechanism and pure-shear shortening that affects the broken foreland and simple-shear shortening in the fold-and-thrust belt of the orogen above the steep slab segment. The transition between the steep and subhorizontal subduction segments is characterized by a 370-km-wide area of diffuse shear, where deformation transitions from pure to simple shear, resembling the transition from thick to thin-skinned foreland deformation in the southern Sierras Pampeanas. This pattern is controlled by the change in dip geometry of the Nazca plate and the presence of mechanically weak sedimentary basins and inherited faults.

Plain language summary

The deformation in the Sierras Pampeanas in the foreland of the southern Central Andes involves sedimentary cover rocks and the underlying crust. The mechanisms driving this style of deformation are debated between two schools of thought, with one group proposing that the subhorizontal subduction of the oceanic

Nazca Plate beneath the continent (also known as the flat-slab area) allows stresses to be propagated away from the oceanic trench into the Sierras Pampeanas, far away from the oceanic trench. Conversely, another group proposes that shear zones and faults in the South American continental crust and lithosphere that are inherited from previous tectonic regimes contribute to weaken the crust, and deformation and uplift of basement blocks follow closely through the reactivation of pre-existing structures such as terrane boundaries or extensional faults. These discontinuities would be responsible for the localization and style of deformation in the foreland. In this study, we numerically simulate the present kinematic and thermomechanical conditions of the Sierras Pampeanas to deduce the factors controlling deformation.

1. Introduction

Flat subduction occurs at 10% of presently active convergent margins (Gutscher et al., 2000) and fundamentally influences the tectono-magmatic evolution of tectonically active orogens; similar configurations have repeatedly existed in the geological past as well (Dickinson & Snyder, 1978; Jordan et al., 1983; Jordan & Allmendinger, 1986; Haines et al., 2001; Mahlburg Kay & Mpodozis, 2002) highlighting the importance of this geodynamic process in governing the distribution of seismicity, volcanism and orogenic growth. The western continental margin of South America hosts the Cenozoic Andes, the type example of a non-collisional Cenozoic mountain belt. The more than 6000-km-long Andes include the Altiplano-Puna Plateau, the second largest orogenic plateau on Earth; segments without a volcanic arc; thick- and thin-skinned thrust belts, whose deformation and uplift have been linked with the characteristics of the subducting Nazca Plate; and inherited, crustal-scale heterogeneities of the upper plate (Jordan et al., 1983). In South America, the Nazca and the Pampean flat slabs are thought to be associated with the subduction of bathymetric anomalies of the Nazca and Juan-Fernandez Ridge (JFR), respectively (Figure 1; Kley et al., 1999; Gutscher et al., 2000; Yáñez et al., 2001; Bello-González et al., 2018). Due to the oblique subduction and form of these anomalies, it has been suggested that the Pampean flat slab in the southern Central Andes (SCA) has migrated from ~20°S lat to its present-day position at ~32°S lat within the last 35 Ma, accompanied by an increase in the magnitude of shortening in the Central Andes (Ramos et al., 2002b; Oncken, 2006; Oncken et al., 2012; Pilger, 1981). Therefore, examining the interaction between the subducting oceanic plate and the continental upper plate in light of inherited heterogeneities and different subduction geometries is vital for our understanding of the different factors that influence strain localization in a convergent-margin setting. In this study, we explore the role of different shortening contributors in the Southern Central Andes (SCA, ~27°S–40°S) by integrating the previously constrained structural and thermal configurations of the plates (Rodriguez Piceda et al., 2021; 2022). According to these configurations the flat slab domain also has a spatial correlation with a portion of the upper plate that has a thick mafic lower crustal unit. This region of the upper plate therefore is relatively colder and rheologically stronger than other parts of the upper plate (Rodriguez

Piceda et al., 2022a,b). Above the flat-slab segment, deformation extends across an a really extensive broken foreland and localizes at the border of the reverse-faulted, thick-skinned Sierras Pampeanas (Ramos et al., 2002b). This style of deformation contrasts with a thin-skinned deformation style in fold-and-thrust belts (FTB), where the sedimentary cover rocks of the foreland sectors are involved in the deformation (Isacks et al., 1982; Jordan, 1984; Jordan & Allmendinger, 1986; Kay & Abbruzzi, 1996; Ramos et al., 2002b). The SCA foreland is characterized by a transition from dominantly thick-skinned (~27°S–33°S) to thin-skinned deformation (>~36°S, Manceda & Figueroa, 1995; Giambiagi et al., 2012; Fuentes, 2016). Between ~33°S and 36°S, both styles of deformation occur together. The eastward propagation and localization of deformation away from the trench through time can be explained by two main mechanisms: The first one involves a bulldozing process of the flat slab directed at the keel of the continental lithosphere (e.g., Jordan, 1984; Ramos & Folguera, 2009; Horton, 2018; Gutscher, 2018), where shear stresses are transmitted from the subduction interface at the trench to the eastern edge of the flat-slab segment. The second mechanism involves the compressional reactivation of steeply dipping crustal faults inherited from previous tectonic regimes (Figure 1d, Mon & Salfity, 1995; Kley & Monaldi, 1998; Cristallini & Ramos, 2000; Mescua et al., 2014; Giambiagi et al., 2014; Lossada et al., 2017)). By investigating the relative importance of the key contributors to strain localization, we discuss the viability of each mechanism in the SCA.

We distinguish between shallow and deep-seated contributors that affect the deformation of the crust or the entire lithosphere, respectively. At the surface, topography and the strength of the sedimentary rocks and their distribution is primarily a function of the formation of individual sedimentary basins that developed during Mesozoic extensional processes; the normal faults that once bounded these sedimentary basins were subsequently reactivated during Cenozoic Andean compression (Mpodozis & Kay, 1990; Uliana et al., 1995; Kley, 1999; 2002; Hongn et al., 2007; Del Papa et al., 2013; Fennell et al., 2019). Low frictional strength of unconsolidated sediments or poorly lithified sedimentary rocks may favor strain localization and thin-skinned deformation (Allmendinger, 1997; Allmendinger & Gubbels, 1996; Kley, 1999; Babeyko & Sobolev, 2005; Liu et al., 2022). Therefore, by including these sedimentary units in our model, we examined the role of crustal-scale heterogeneities. At greater depths, strain localization can be affected by lithospheric-scale heterogeneities, which can be classified as inherited discrete discontinuities, such as suture zones that developed during the amalgamation of Paleozoic terranes (e.g., Ramos, 2010). Alternatively, they may constitute volumetric discontinuities associated with inherited variations in the composition and/or thickness of the layers of the continental lithosphere (i.e., crystalline crust and lithospheric mantle), which reflect the tectono-magmatic evolution of different sectors within the orogen and its foreland (Ibarra et al., 2018, 2019; Liu et al., 2022; Rodriguez Piceda et al., 2021). Overall, structural and geometric parameters may influence lithospheric strength and the localization of deformation (Horton et al., 2022, Ramos et al., 2002, 2010, GIambiagi et al., 2022, Barrionuevo et al, 2021).

Using data-driven geodynamic modelling we developed a numerical modeling workflow that integrated data-driven three-dimensional structural, density, and thermal models (Rodriguez Piceda et al., 2021; 2022) into a geodynamic model to simulate shortening in the lithosphere of the SCA. Ultimately, our analysis sheds new light on the long-standing debate on the role and degree of influence of flat-slab geometry and inherited crustal-scale heterogeneities on deformation styles in orogenic forelands (Ramos et al., , 2002; Ramos & Folguera, 2009; Horton, 2016; Lossada et al., 2017).

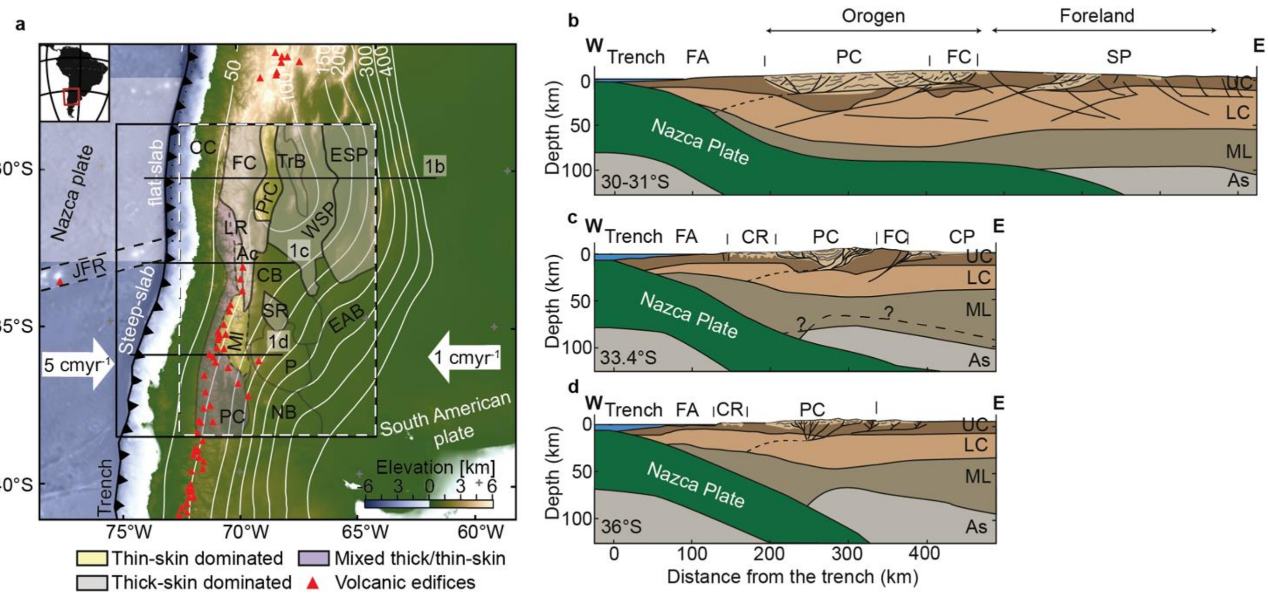

Figure 1 Structural cross sections and map of the Southern Central Andes. **a** topography and bathymetry of the model area based on ETOPO1 global relief model (Amante & Eakins, 2009), indicating the higher modelled resolved area (black rectangle) and the borders of the morphotectonic provinces (modified from Rodriguez Piceda et al., 2021) color-coded by the dominant style of deformation. The white-dashed rectangle outlines the extent of the gravity-constrained structural model (Rodriguez Piceda et al., 2021). Red triangles depict Cenozoic volcanic edifices. Depth contours of the top slab (Hayes et al., 2018) are shown in white lines. Dashed black lines in the oceanic domain delimit the Juan Fernandez Ridge (JFR). Oceanic and continental plate velocities are indicated by white arrows (Sdrolias & Müller, 2006; Becker et al., 2015). Abbreviations of main morphotectonic provinces: CB: Cuyo basin, CC: Coastal Cordillera, CP: Cerrilladas Pedemontanas, ESP: Eastern Sierras Pampeanas, NB: Neuquén basin; P: Payenia, PC: Principal Cordillera (LR= La Ramada fold-thrust belt, Ac: Aconcagua fold-thrust belt, Ml: Malargüe fold-thust belt), FC: Frontal Cordillera, FA: forearc, PrC: Precordillera, SR: San Rafael Block, TrB: Triassic basins, WSP: Western Sierras Pampeanas, EAB: Extra-Andean basins.. **b** Transect between 30-31°S (modified from Ramos et al., 2002b; Gans et al., 2011; Lossada et al., 2017; Stalder et al., 2020) **c** Transect at 33.4°S (modified from Barrionuevo

et al., 2021). **c** Transect at 36°S (modified from Barrionuevo et al., 2021). Abbreviations of lithospheric and asthenospheric units: UC: upper crust, LC: lower crust, ML: mantle listosphere, Ast: asthenosphere. Light-brown colored area indicates crustal regions with pronounced deformation. Slab dip based on CRUST 2.0 (Hayes et al., 2018).

2. Methods

2.1 Governing equations

We used the finite element code ASPECT (Advanced Solver for Problems in Earth's ConvecTion, version 2.3.0-pre, Kronbichler et al., 2012; Rose et al., 2017; Heister et al., 2017; Bangerth et al., 2021) to simulate brittle and ductile deformation. This code solves for conservation of the momentum (eq. 1), mass (eq. 2) and energy (eq. 3), together with the advection and reaction equations (eqs. 4-5).

$$-\nabla \cdot (2\eta\acute{\varepsilon}) + \nabla p = \rho g \, , \qquad (2)$$

$$\nabla \cdot \boldsymbol{u} = 0 \, , \qquad (2)$$

$$\varrho Cp\left(\frac{\partial T}{\partial t} + \boldsymbol{u} \cdot \nabla T\right) - \nabla \cdot k\nabla T = \varrho H + (2\eta\acute{\varepsilon}) : \acute{\varepsilon} - \alpha T \, \boldsymbol{u} \cdot g \, , \qquad (3)$$

$$\frac{\partial ci}{\partial t} + \boldsymbol{u} \cdot \nabla ci = qi \, , \qquad (4)$$

Where $\acute{\varepsilon} = \frac{1}{2}.(\nabla\boldsymbol{u} + (\nabla\boldsymbol{u})^T$, is the deviatoric strain rate tensor, $u = u(\vec{x}, t), p = p(\vec{x}, t)$ and $T = T(\vec{x}, t)$ are the velocity, pressure and thermal fields, respectively. Cp is the heat capacity, ρ and ϱ are the density and the reference density (see eq. 5), k is the thermal conductivity, α is the thermal expansivity, η is the viscosity, t is time, ci is the composition, and qi is the reaction rate. The energy equation (eq. 3) includes shear heating and adiabatic heating, while the contribution of radiogenic heating to the temperatures is already included in the initial thermal condition.

To simulate realistic densities, we used the equation of state of Murnaghan (1944, eq. 5) which takes into account pressure, although the latter is neglected in the mass-conservation conversion equation (eq. 2). This assumption can be considered as an acceptable approximation since in subduction models compressibility is considered to have a negligible effect (Fraters, 2015).

$$\rho f = \rho refi \left(1 + \left(P - \left(\frac{\alpha i}{\beta i}\right)(T - Tref)\right) ki\beta i\right)^{\frac{1}{ki}} , \qquad (5)$$

ρf and $\rho refi$ are the final and reference density for each composition at reference temperature (Tref = 293 K) and surface pressures. αi is the thermal expansivity, βi is the isothermal compressibility and ki is the isothermal bulk-modulus pressure derivative.

The dominant mechanism of deformation depends on the yield stress, which is defined as the maximum differential stress that a rock is able to withstand without experiencing permanent deformation (Goetze & Evans, 1979). Viscous (ductile) deformation is simulated by harmonic averaging of dislocation and diffusion-creep mechanisms (eq. 6, Glerum et al., 2018):

$$\eta_{\mathrm{diff|disl}} = 0.5\, A_{\mathrm{diff|disl}}^{\left(-\frac{1}{\mathrm{n}}\right)}\, d^m \dot{\varepsilon}_{\mathrm{e}}^{\frac{1.-\mathrm{n}}{\mathrm{n}}}\ \exp\left(\frac{Q_{\mathrm{diff|disl}} + P.V_{\mathrm{diff|disl}}}{nRT}\right), \qquad (6)$$

where A is the prefactor rescaled from uniaxial experiments, n is the stress exponent, d and m are the grain size and grain size exponent, $\dot{\varepsilon}_e$ is the square root of deviatoric strain rate, Q is the energy of activation, V is the volume of activation, P the pressure, R the gas constant, and T the temperature. Dislocation creep is grain-size independent, therefore the term d^m is removed from eq. (6) for n_{disl}. In turn, plastic (brittle) deformation is described by the Drucker-Prager criterion (eq. 7):

$$in\ 3D:\ \sigma y = \frac{6C.cos\Phi}{\sqrt{3(3-sin\Phi)}} + \frac{6P.sin\Phi}{\sqrt{3(3-sin\Phi)}}, \qquad (7)$$

where C, P and F hold for the cohesion, the pressure and the internal friction angle (radians), respectively. Additionally, we included a linear plastic strain softening for the crustal layers which depends on the integrated strain accumulation (Table 1).

Finally, the effective plastic viscosity is given by:

$$\eta = \frac{\sigma y}{2\dot{\varepsilon}}, \qquad (8)$$

The material and temperature fields used as input were defined on the basis of 3D lithospheric-scale models of the SCA (Rodriguez Piceda et al., 2021, 2022) and are described along the mechanical properties corresponding to the lithospheric layers in Section 2.2. Since each conservation equation is solved using the continuity equation, the deformation takes the appearance of shear zones in numerical geodynamic modeling. Therefore, highly deformed areas may potentially represent highly “faulted areas”.

2.2 Model setup

The geometries of the lithospheric layers were adopted from the 3D structural model of Rodriguez Piceda et al. (2021). This model is built upon the integration of geophysical and geological data and models, including the gravity field, and covers a region of 700 km x 1100 km x 200 km (Figure 1). Eight layers constituting the model were defined based on the principal density contrasts in the lithosphere: (1-2) oceanic and continental sediments (‘sediments’, Figure 2a); (3) upper continental crystalline crust (‘upper crust’, Figure 2c) ; (4) lower continental crystalline crust (‘lower crust’, Figure 2d); (5) continental lithospheric mantle (‘continental mantle’, Figure 2f); (6) oceanic crust; (7) oceanic lithospheric mantle (‘oceanic mantle’), and (8) asthenospheric mantle. For the geodynamic simulations, two main modifications were introduced to change the original model of Rodriguez Piceda et al. (2021). First, the model was extended 200 km in depth, 500 km in the E-W direction, and 200 km in the N-S direction. The resulting box model is 1700 x 1700 x 400 km, with a central area of interest of 600 x 600 x 400 km (Figure 3). Second, we introduced an interface representing the lithosphere-asthenosphere boundary (LAB) in the continental plate based on the thermal LAB model of Hamza & Vieira (2012). The main features of the model are depicted (Figure 2) in terms of the: (a) thickness of sediments; (b) thickness of the continental crust; (c) thickness of the upper crust; (d) thickness of the lower crust; (e) Moho depth, and (f) LAB depth.

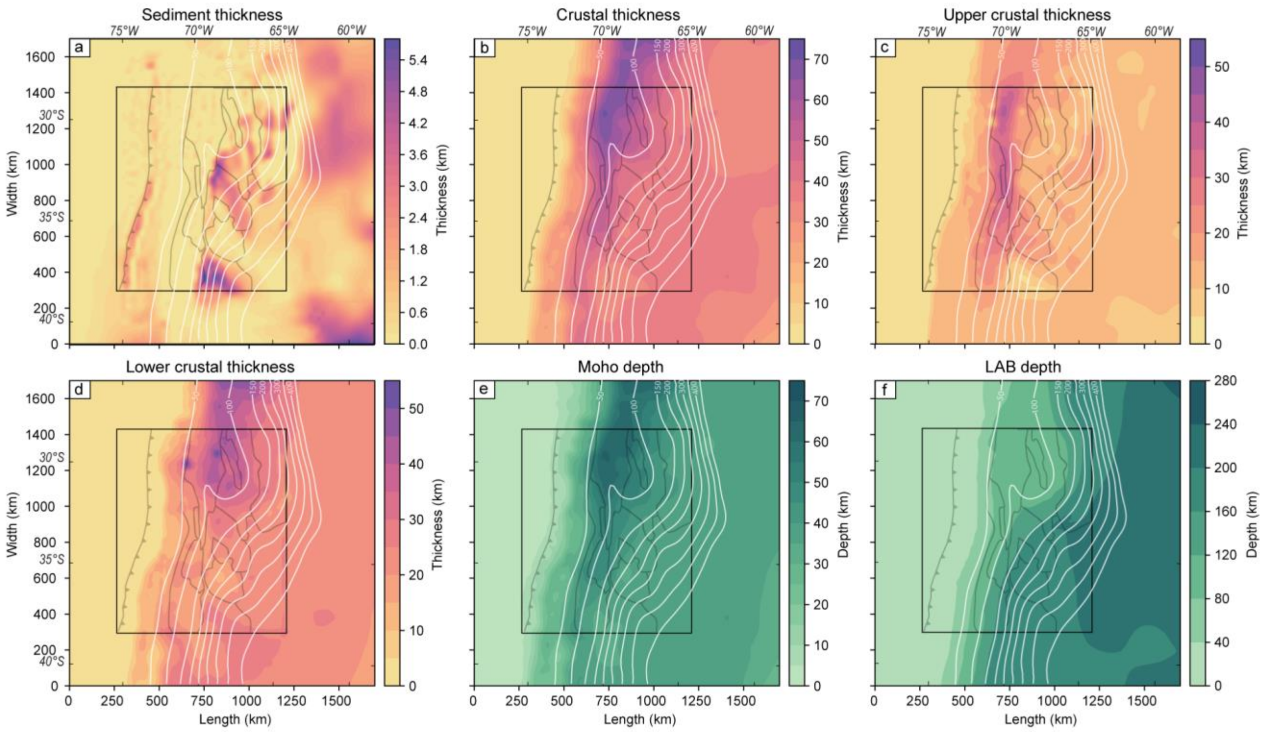

Figure 1 Layer thickness and depth map of the SCA. Main structural features of the SCA lithosphere from the model of Rodriguez Piceda et al. (2021). **a**, total crystalline crustal thickness; **b** upper continental crustal thickness; **c** lower continental crustal thickness; **d** sediment thickness; **e** Moho depth and **f** LAB depth taken from Hamza and Vieira (2012). The black rectangle shows the most refined model area.

The initial temperature field is based on a 3D thermal model of the SCA (Rodriguez Piceda et al., 2022), covering the same region as the structural model of Rodriguez Piceda et al. (2021). Temperatures were derived from the conversion of S-wave tomography (Schaeffer & Lebedev, 2013) together with steady-state conductive modeling, and were additionally validated by borehole temperatures and surface heat-flow data

(Rodriguez Piceda et al., 2022). One caveat of this model is related to the determination of the thermal structure of the oceanic slab through the conversion of S-wave tomography to temperature. The lack of seismic tomography resolution (0.5° longitudinally and 25km in depth) does not allow us to properly resolve the oceanic plate boundaries, which results in relatively high temperatures in comparison to the temperatures predicted by numerical solutions (Wada & Wang, 2009; van Keken et al., 2019). For this reason, we have assigned a conductive geotherm between 273 K and 1573 K from the top to the base of the oceanic plate as initial condition.

The thermomechanical properties of each model unit were assigned according to its lithological composition (Rodriguez Piceda et al., 2021; 2022). These lithologies were inferred from the comparison between gravity-constrained densities (Rodriguez Piceda et al., 2021) and mean *P*-wave velocities (Araneda et al., 2003; Contreras-Reyes et al., 2008; Pesicek et al., 2012; Marot, 2014; Scarfi & Barbieri, 2019), combined with rock-properties compiled from literature (Sobolev & Babeyko, 1994; Christensen & Mooney, 1995; Brocher, 2005) and other seismic properties (Wagner et al., 2005; Gilbert et al., 2006; Alvarado et al., 2007; Ammirati et al., 2013; 2015; 2018). The reference density for each composition was recalculated, so the estimated final density of each composition (i.e., after correcting for pressure and temperature, eq. 5, Table 1), is in the range of the density predicted by the structural model of Rodriguez Piceda et al (2021), and the resulting topography was compared to the present-day topography (Text B.S1 and Figure 1). The thermal properties used in the initial thermal field are from published average values for the lithology of each model unit (see references in Rodriguez Piceda et al., 2022a;

We assigned rheological properties to each composition for the viscous regime, dry olivine (Hirth & Kohlstedt, 2004, H&K2004) to the oceanic mantle (3321 kg/m³), diabase (Mackwell et al., 1998, Mck1998) to the lower crust (3129 kg/m³), wet olivine (Hirth & Kohlstedt, 2004) to the continental mantle (3388 kg/m³), wet quartzite (Gleason & Tullis, 1995, G&T1995) to the upper crust (2812 kg/m³), the oceanic and continental sedimentary layer (2300 and 2400 kg/m³) , and wet olivine (Hirth & Kohlstedt, 2004) to the upper mantle to represent the hydrated mantle wedge.

For the oceanic crust (2857 kg/m³), we prescribed a weak quartzite rheology (Ranalli, 1997) to simulate the visco-plastic behavior of a quartz-dominated “mélange”, which is characteristic of the subduction interface (Sobolev et al., 2006; Muldashev & Sobolev, 2020), with a relatively low friction coefficient of 0.015, which produces an appropriate maximum shear stress of 20 to 40 MPa, depending on the temperature and the dip of the oceanic plate (Figure S4; Lamb & Davis, 2003; Sobolev et al., 2006).

For the plastic regime, we set a cohesion of 40 MPa and a friction angle of 30° to the mantle layers. The short model runtime prevents the layers from weakening by accumulating plastic strain, thus we assigned a weak plastic rheology to the sedimentary layer (i.e., a friction angle of 3° and a cohesion of 2 MPa). The minimum viscosity was set to 1e19 Pas during the first 100 ka of model run, and subsequently changed to 2.5e18 Pas.

Here, we refer to the second invariant of the square root of the deviatoric strain rate in the plastic and viscous domains as plastic strain rate and viscous strain rate, respectively. The plastic strain represents the integrated plastic strain rate over time and allows us to see the regions of the model that have been deformed and weakened during the model run. We used adaptive mesh refinement (Figure 3) to resolve the central and outer domains, with a resolution of ~6km and 12.5km, respectively. We ran the model simulation for ~250 ka while applying velocities of 5 cm/yr and 1 cm/yr to the oceanic and continental plates, respectively (Sdrolias & Müller, 2006), whereas the left and right asthenosphere borders were left open. To fulfill the volume conservation constraint, we prescribed an equivalent volume outflow to the bottom boundary equal to the prescribed inflow from the plate velocity. We use the advantages of the ASPECT code by prescribing a dynamically deformable mesh in order to simulate present-day topography. In particular, the topography in the model is uplifted and advected using the ASPECT-FastScape coupling (Braun & Willett, 2013; Bovy, 2021; Neuharth et al., 2021).

		Asthenosphere (AST)	Oceanic plate			Continental plate			
	Units	Upper mantle	Weak Gabbro	Lithomantle	Oceanic sediments	Continental Sediments	UpperCrust	LowerCrust	Lithomantle
Lithology	/	Harzburgite	Gabbro +melange (serpentinite)	Moderately depleted Lherzolite	Siliclastic	Siliclastic	Diorite	Mafic Granulite	Wet olivine
Reference	/	H&K2004	Ranalli, 1997	H&K2004	G&T1995	G&T1995		Mck1998	H&K2004
Composition used in the model	/	Dry olivine	Wet quartzite	Dry olivine	Wet quartzite	Wet quartzite		Maryland diabase	Wet olivine
Grain size	m	1e-3	1e-3	1e-3	1e-3	1e-3		1e-3	1e-3
Creep pre-exponential factor Bd / Bn	$Pa^{-ndiff/ndisl}.\ s^{-1}$	1e-9 / 8.49e-15	- / 2.25e-17	2.25e-15 / 2.96e-16	- / 8.57e-28	- / 8.57e-28		- / 7.13e-18	1e-9 / 2.96e-14
Grain-size exponents	mm	0	-	3	-	-		-	0
Activation energies Ed / En	kJ/mol	335 / 540	- / 154	375 / 535	- / 223	- / 223		- / 345	335 / 515
Activation volume Vd / Vn	m^3/mol	4.8e-6 / 12e-6	- / 0	10e-6 / 14e-6	- / 0	- / 0		- / 0	4.8e-6 / 14e-6
Stress exponents	n	3.5	2.3	3.5	4	4		3	3.5
Internal angle of friction	degree	30	0.8594	30	30 -> 6	3	30 -> 6	30 -> 6	30
Cohesion	MPa	40	0.1	40	20 -> 10	2	20	40 -> 20	40
Plastic strain weakening interval	none	-	0 - 0.3	-	0.5 - 1.5	0 - 1.5	0.5 - 1.5	0 - 1.5	0 - 1.5
Thermal conductivity	W/K/m	3.3	2.5	3.3	2.2	2.2	2.5	2.6	3.3
Densities	kg/m^3	3347	2857	3321	2300	2400	2812	3129	3388

Table 1 Model parameters for each composition. G&T1995 : Gleason & Tullis, 1995. Mck1998 : Mackwell et al., 1998. H&K2004.Hirth & Kohlstedt, 2004. Lithology corresponds to the one defined in Rodriguez Piceda et al., (2020) whereas representative compositions in the model are defined based on deformation experiments. Prefactors (A) were scaled from uniaxial compression experiments (Dannberg et al., 2017). We applied wet olivine (Hirth & Kohlstedt, 2004) to the upper mantle to be representative of the hydrated mantle wedge and mantle lithosphere caused by the long-term subduction at the Chile margin (Babeyko et al., 2006).

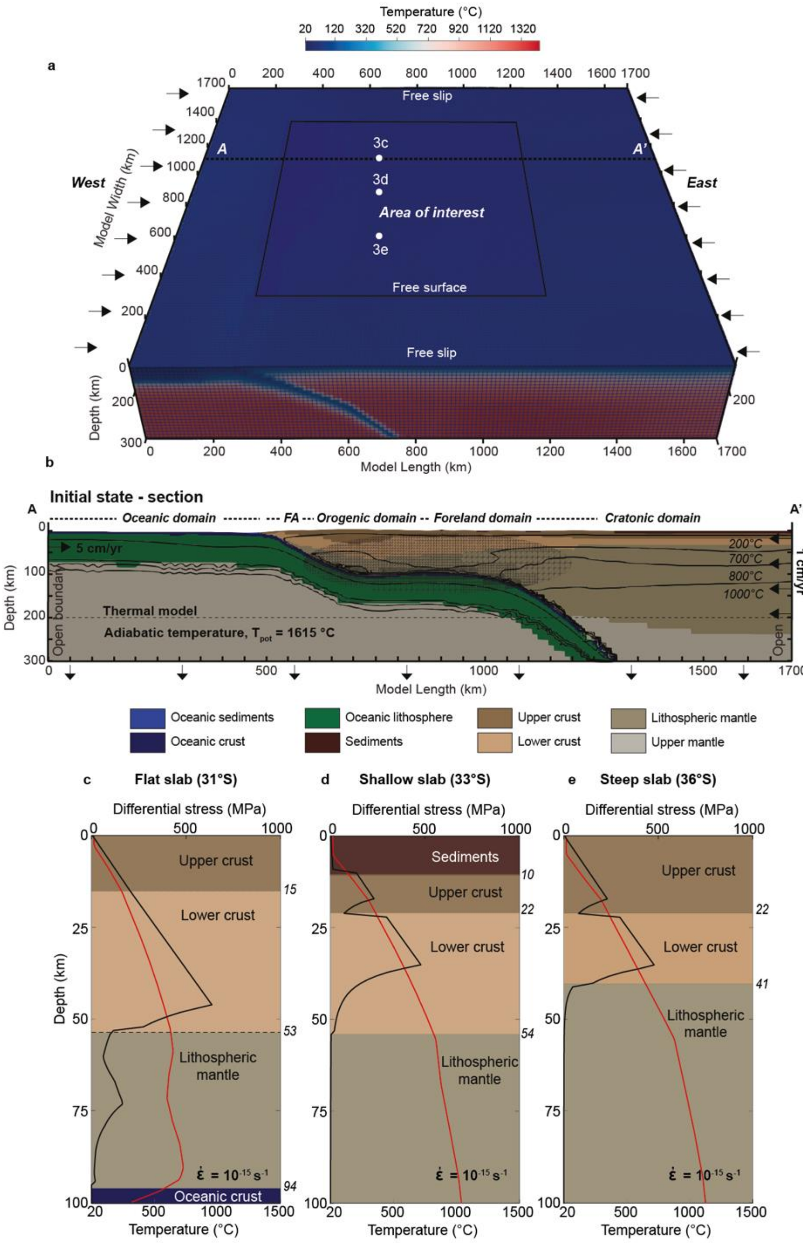

Figure 2 Model setup. **a** 3d model geometry, mesh refinement and temperature. **b** 2D W-E cross section long with location indicated in **a**, showing: boundary and initial conditions, refinement of the interface, composition of the lithospheric layers and temperature. T_{pot} indicates the mantle potential temperature and FA the forearc domain. **c-e** yield strength (black line) and temperature (red line) profiles of the upper plate at: **c** flat-slab. **d** shallow slab. **e** steep slab.

First, we computed the reference model (S1) using the parametrization discussed above (section 2.2). Subsequently, we ran a series of models (S2, S3, S4 and S5, Table 2) with varying multiple parameters to investigate the relative contribution of key factors with respect to the strain localization in the upper plate.

3. Modeling results

3.1 Reference model (S1)

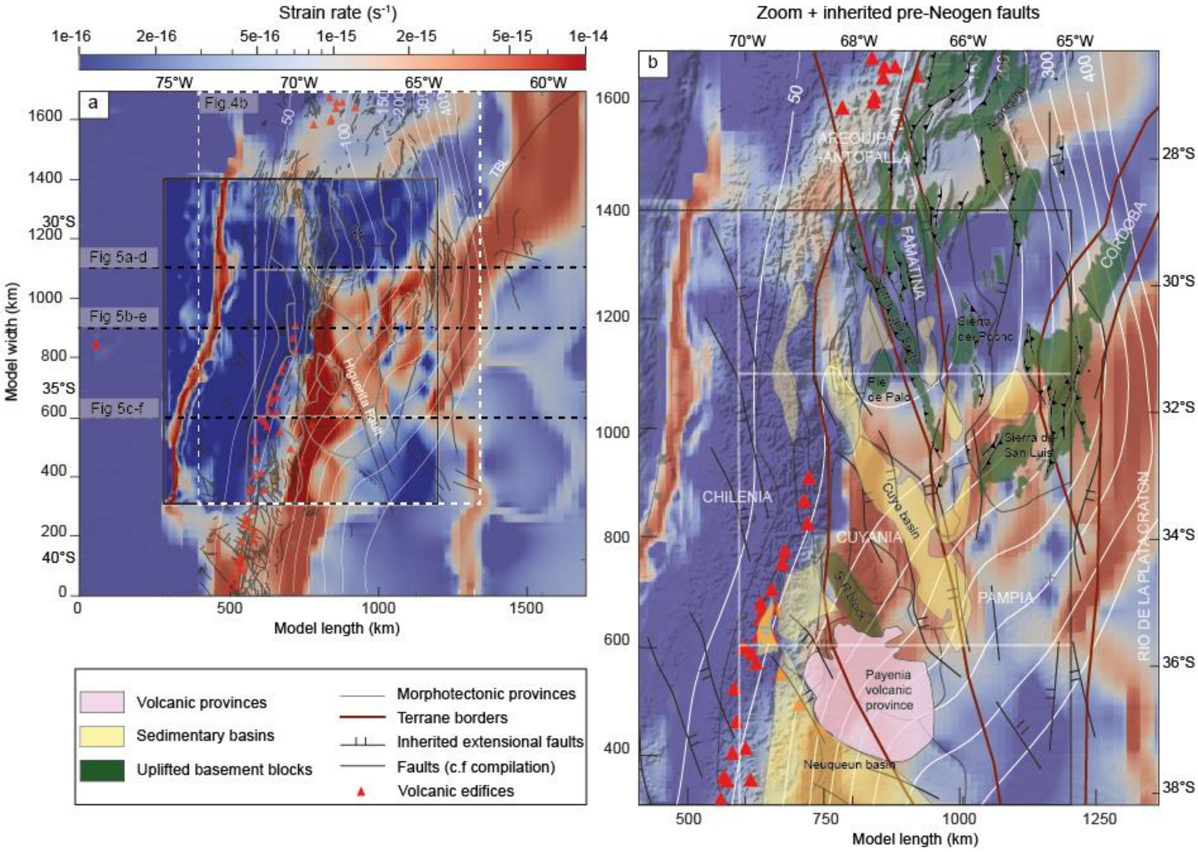

Figure 1 Surface-strain rate of the Reference model. **a.** Strain rate superposed with compiled faults (Moscoso & Mpodozis, 1988; García, 2001; Giambiagi et al., 2003; Broens & Pereira, 2005; Folguera & Zárate, 2011; Martino et al., 2016; Litvak et al., 2018; Martínez et al., 2017; Sánchez et al., 2017; Meeßen et al., 2018; Riesner et al., 2018; Olivar et al., 2018; Jensen, 2018; Melnick et al., 2020; Costa et al., 2020; Eisermann et al., 2021). **b.** Close-up of the Sierras Pampeanas morphotectonic province and extensional faults and terrane sutures in red (Ramos et al., 2002a; Wimpenny, 2022). Green structures indicate uplifted Sierras Pampeanas ranges. The timing of uplift is indicated by filled coloured circles (Table B.S1). White lines are isobaths of the top of the subducting oceanic plate. Red triangles indicate the position of known volcanic edifices. Major structures and morphotectonic provinces are highlighted by different colours in the legend.

Reference model S1 is built upon the known values for plate convergence, subduction-interface coefficient, sediment strength, and present-day topography (see Methods section). From south to north, deformation migrates to the east, with the strain localizing in the southern part, while in the northern part it is distributed over multiple faults (Figures 4 and 5). This shift is related to a change in the shortening mode from simple shear to pure shear. When considered in a strain-rate snapshot, simple-shear shortening occurs when the plastic strain-rate band in the upper crust connects with the viscous strain-rate band in the lower crust to form a shear zone (Figure 5c–d), which is expressed by thin-skinned deformation in the FTBs. Conversely, if no connection occurs between the plastic and viscous strain-rate localization zones, pure-shear shortening involving multiple faults is favored, leading to distributed deformation within the crystalline basement, which corresponds to a thick-skinned foreland-deformation style. The resulting surface strain-rate field indicates three distinct north-to-south oriented branches (Figure 4a) characterized by a distinct shortening mode:

(i) *A Western branch between 75°W and 73°W*, which corresponds to the trench. At the trench, both plates are decoupled by the weak subduction interface, where most of the deformation localizes. Conversely, the crust of the adjacent cold and mechanically strong forearc is virtually undeformed.

(ii) *A Central branch between 73°W and 70°W,* which comprises the orogen and the adjacent foreland. Strain distribution varies from north to south. In the flat-slab segment, the strain localizes in the eastern front of the orogen and intensifies southward and the foreland crust is almost undeformed. In the shallow-slab segment, the strain distributes in the foreland over multiple oblique or en échelon, crustal-scale structures that connect to the Eastern branch and which are associated with pure-shear shortening. In the steep-slab segment, strain localizes in front of the orogen and in the foreland by simple-shear shortening.

(iii) An Eastern branch between 60°W and 65°W, where deformation localizes in front of the flat slab by pure-shear shortening, as well as along regions that spatially correlate with Pre-Andean cratonic structures related to the amalgamation of terranes during the formation of Gondwana, such as the Transbrazilian Lineament (Fairhead & Maus, 2003; Ramos, 2010). In the south, the deformation localizes within smaller structures that straddle the Rio de la Plata craton.

On a lithospheric scale, these three branches interact spatially. The Sierras Pampeanas morphotectonic province appears as a large-scale shear zone that accommodates deformation via en-échelon structures associated with the uplift of isolated rigid basement blocks. The deformation at the borders of these blocks is accommodated by diffuse dextral strike-slip deformation (Pons et al., 2023, will be submitted with this paper).

We also distinguish three slab segments of the subducting Nazca Plate (Figure 5): a flat segment (27°W to 32°W, 1000–1400 km model width-coordinates), a shallow segment (32°W to 35°W , a 600–1000 km model width-coordinates), and a steep segment (35°W to 41°W, 0–600 km model width-coordinates). The E-W-oriented cross sections across the reference model (Figure 5) illustrate how the plastic (brittle) and viscous deformation is accommodated in the continental plate along the segments with different slab geometry (Figure 5a–c), and how stresses are distributed within the plates (Figure 5d–f). Above the steep segment, the upper plate is characterized by simple-shear shortening at the front of the orogenic thrust wedge (Figure 5c). Above the shallow subduction segment, the model predicts a mixture of simple and pure-shear shortening

(Figure 5b). No significant deformation occurs above the flat-slab segment, while pure-shear deformation takes place at its eastern edge (Figure 5a).

The greatest horizontal stress is effectively transmitted throughout the continental plate to weak regions where the deformation localizes. In the flat-slab section (Figure 5a), deformation takes place more than ~700 km away from the trench and is localized over a 200-km-wide band in the eastern broken foreland of the Sierras Pampeanas. The model predicts local plastic (equivalent to brittle in reality) deformation (Figure 5a) on top of the colder flat-slab segment at a 100 km depth (Figure 5c), which also correlates with the bending of the slab (i.e., internal shear stress, Figure 5a, d). Horizontal stresses of > 200 MPa are generated locally in the crust and in the colder lithospheric mantle of the forearc, where the BDT is deeper, but they are not sufficiently large to cause significant deformation. The thick and warmer orogen shows no significant deformation despite being weaker, which is illustrated by the shallower BDT (Figure 5a). On top of the flat-slab segment, the greatest horizontal stress is mainly generated by the subducting plate as shown by the eastward-pointing velocity vectors (Figure 5d). The horizontal stresses also build up within the cold and strong lithospheric mantle of the foreland. Despite the presence of a weak sedimentary basin at the surface, deformation does not localize and stresses are partially transmitted eastward from the base of the upper crust to the Eastern Sierras Pampeanas. Finally, crustal shortening results in a stress drop in the eastern Sierras Pampeanas, and the polarity of the velocity field switches from east to west, indicating that velocity is now determined by the upper plate (Figure 5d).

Shortening is distributed over multiple faults within a relatively wide area (~200 km), similar to pure-shear shortening. In the shallow-slab section (Figure 5b), the plastic and viscous strain rates merge in front of the orogen (at ~800 km model coordinates) to form a deep shear zone dominated by simple-shear shortening. In the foreland, the deformation distributes over multiple faulted areas along a wide area, with rigid crustal blocks with a shallower BDT. Similarly to the previous section the deformation terminates in the transition with the cratonic domain and a thick-skinned style of deformation, which results from pure-shear shortening. The horizontal stress also builds up locally in the cold forearc (>~200 MPa; Figure 5e), where the great mechanical strength of the rocks prevents failure and causes a transmission of stresses to the orogen. Additionally, the horizontal stress builds up in the lower crust and partially transmitted to the Eastern Sierras Pampeanas. Strain localizes at the orogenic front by simple-shear shortening and is accommodated y pure-shear shortening in the foreland and at the transition with the cratonic domain. In the steep-slab section, the deformation strongly localizes in front of the orogen (~800 km model length; Figure 5c).

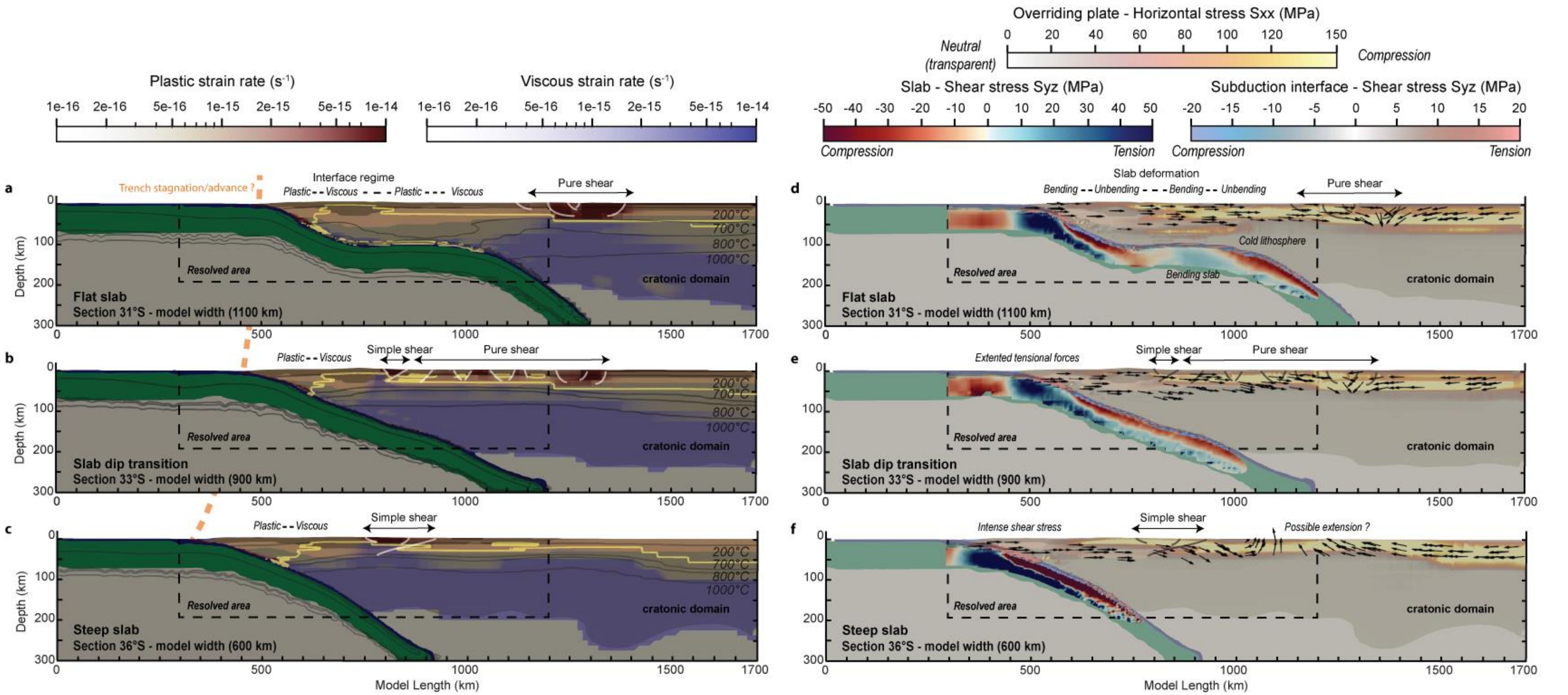

Figure 2 Representative cross sections of the subduction segments for the reference model (see location in Figure 1): Strain rate **(a-c)** and stress (**d-f**). **a-d** Flat-slab (31°S). **b-e** Shallow slab (33°S) and **c-f** Steep slab (36°S). **a-c** white lines are interpreted faults, yellow lines show the depth of the brittle-ductile transition (BDT), and dark lines indicate isotherms. **d-f** black lines indicate the interpreted faults, arrows indicate the sense of the velocity for the crust.

297

3.2 Model variations

In this section, we test the relative contribution of four key parameters on the resulting surface strain-rate distribution: (1) the friction coefficient at the oceanic plate interface, (2) the strength of continental sediments, (3) the topography, and (4) the velocity applied to the model boundaries. The friction coefficient at the oceanic plate interface is varied between 0.005 and 0.05 (models S2a-c) in agreement with the models of the long-term evolution of the Central Andes (Sobolev et al., 2006; Sobolev & Babeyko, 2005). The internal friction angle (Φ) and cohesion (C) of the sediments is varied from 3° to 30° (friction coefficient 0.05 to 0.5) and from 2 to 20 MPa, respectively (Figure 6, models S3a-d). In addition, we tested the effect of topography on the strain distribution by removing the topographic relief in the initial configuration with and without applied velocities at the boundaries (Figure 6, models S4a-d). Finally, the oceanic and continental plate velocities are varied between 0 cm/yr and 6 cm/yr, covering the range of possible velocities (Figure 6, models S5a-d). Table 2 summarizes the alternative model runs. In order to discuss the relative effect of each key parameter to the strain localization we computed the residual surface strain rate between the model variant and the reference model (Figure S3). To estimate the variation in strain localization above the trench related to flat, shallow, and steep subduction, we divided the surface of each model into sub-domains. For each domain, we calculated an average of the strain rate using the root mean square. Finally, we calculated the relative change between the domains of the model variants and of the reference model. Thus, we obtained a summary of the relative percentage of contribution of each key parameter to the reference model for each domain (Figure 7). Note that for a similar budget of force between the reference model and the model variants, if the strain at the surface localizes further in one of the branches (section 3.1), it may decrease in another one to keep the balance. Because part of the forces might be redistributed outside of the area of interest, the net percentage of the domains might not be equal to 100%.

Group	Name	Variation
Friction coefficient of the subduction interface (μ_{int})	S2a	μ_{int} = 0.005
	S2b	μ_{int} = 0.035
	S2c	μ_{int} = 0.05
	S2d	μ_{int} = 0.07
Sediment strength (internal friction angle Φ and cohesion C)	S3a	Φ = 30° ,C = 20 MPa
	S3b	Φ = 30°, C = 2 MPa
	S3c	Φ = 15°, C = 20 MPa
	S3d	Φ = 3°, C = 20 MPa
Model with variation of the topography	S4a	no initial topography w/ boundary velocity
	S4b	no initial topography, w/o boundary velocity
	S4c	no topography w/ boundary velocity
	S4d	no topography w/o boundary velocity
Velocities of the subducting plate (SP) and the overriding plate (OP)	S5a	SP= 0 cm/yr , OP= 1 cm/yr
	S5b	SP= 5 cm/yr, OP = 0 cm/yr
	S5c	SP = 6 cm/yr, OP = 0 cm/yr
	S5d	SP = 0 cm/yr, OP = 6 cm/yr

Table 1 Model variations with respect to the reference model.

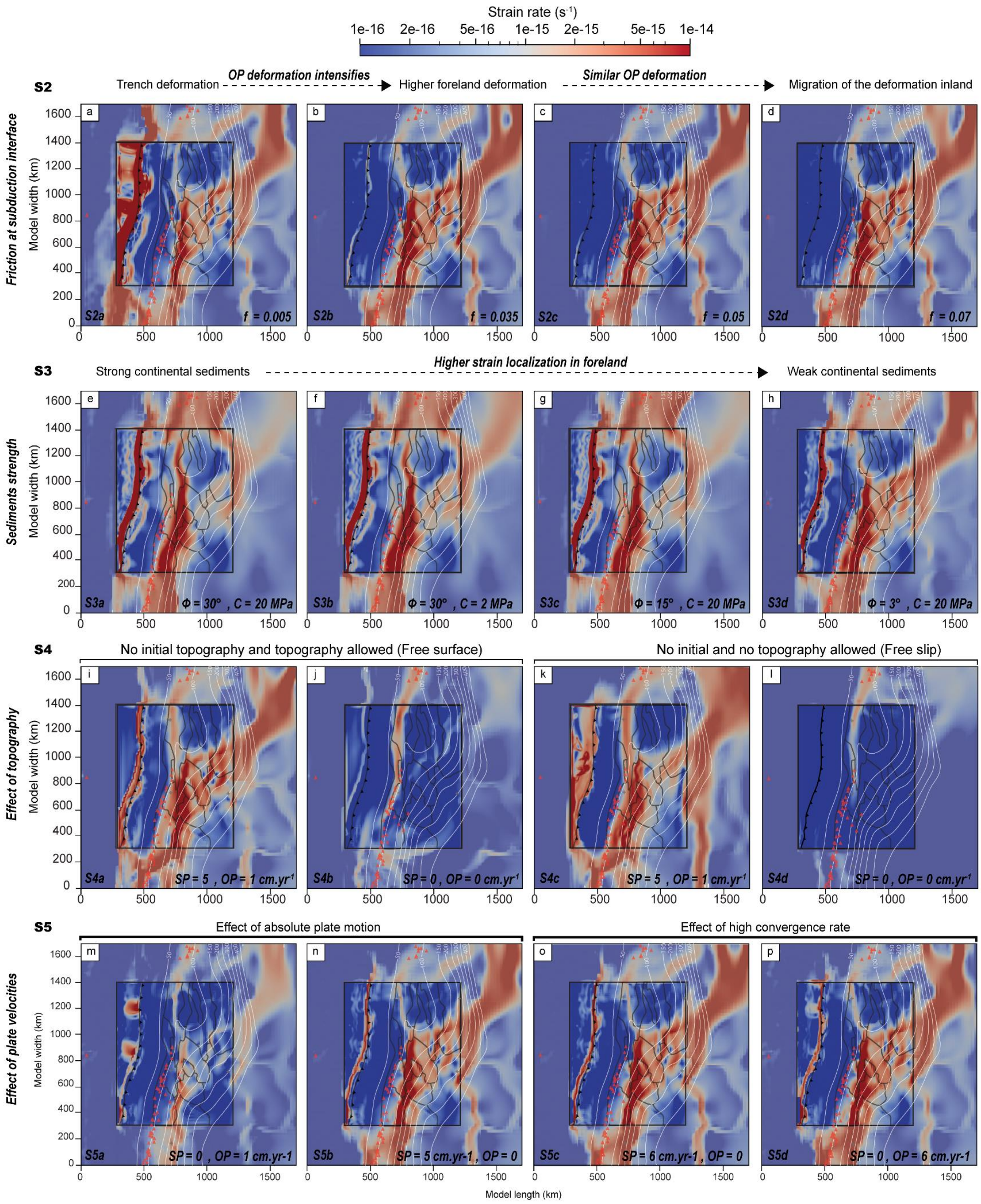

Figure 3 Strain-rate distribution in various models. **a-d** Models with variable friction coefficients (f) at the subduction interface: **a** S2a, f 0.005. **b** S2b, f 0.035. **c** S2c, f 0.05. **d** S2d, f 0.07. **e-h** Models with alternative strength (Φ internal friction angle, and C cohesion) of the sedimentary layer. **e** S3a, Φ = 30° C = 20 MPa. **f** S3b, Φ = 30° C= 2 MPa. **g** S3c, Φ = 15° C= 20 MPa. **h** S3d Φ =3° C=20 MPa. **i-l** Models without prescribing initial topography. **i-j** Free surface with advection of the topography allowed. **k-l**

Free-slip, no advection of topography allowed. **l, k** models with plate velocity, SP = 5 cmyr-1 and OP =1 cmyr-1 . **j,l** models without velocity, SP and OP = 0 cmyr-1. For abbreviations of plate velocities, see table 2. **m-p** Models with variations of prescribed plate velocity. **m** Absolute overriding plate velocity orthogonal to the trench, no subducting plate velocity. **n** Absolute subducting plate velocity orthogonal to the trench, no overriding plate velocity. **o** Convergence velocity, applied only to the subducting plate. **p** Convergence velocity, applied only to the overriding plate. Black rectangle is the resolved area; dark line indicates the boundaries of the morphotectonic provinces, red triangles denote position of volcanic edifices.

3.2.1 Models with variable slab-interface friction (S2a-d)

The greatest differences between the reference and alternative models related to the slab interface friction occurs along the trench (Figure 6). With low slab interface friction (S2a; Figure 6a), the strain strongly localizes more at the trench (x18 or +994%, Figure 7). Less strain localizes within the overriding plate (-27 to -54%), including the orogen and the back-arc. Conversely, higher interplate friction (S2b-c; Figure 6b-d) translates into a twofold lower strain localization at the trench (-92 to 97%), and slightly higher overriding plate deformation (+6%, Figure 7). Therefore, for these short simulations the increase of friction at the interface results in similar intensity of upper-plate deformation with respect to the reference model S1.

3.2.2 Strength of continental sediments (S3a-d)

Modifying sediment strength results in a significant change in strain-rate distribution. Weaker sediments lead to a higher degree of strain localization adjacent to the orogen and the foreland basins (S3a-d, Figure 6e-h). A decrease in the internal friction angle (S3c and S3d, Figure 6f and h) decreases the strength significantly more than a decrease of cohesion (S3b and S1, Figure 6g and Figure 4), promoting the compressional reactivation of foreland structures. With high friction and cohesion (S3a, Figure 6e), the strain rate in the foreland appears to be more diffuse and less localized (-35 and -40%), causing strain to localize closer to the orogen and the trench (+220%) compared to the reference model (Figure 7). With weaker continental sediments, the major component of deformation switches from the orogen interior outward to its front. Overall, stronger sediments result in more active shallow deformation near the trench and in the orogen above the flat slab (S3a, 423%), and less pronounced deformation in the foreland above the shallower and steeper domains (~-40%, Figure 7).

3.2.3 Models with topography variations (S4a-d)

By initializing the model without present-day topography, we aim to look at the effect of internal forces related to the density and thickness configuration of the overriding plate layers. In models S4a and S4b, we allow for the topography to evolve with and without plate velocities, respectively (Figure 6i-j). S4a exhibits a strain-rate distribution similar to S1 (cf. Figure 6a), but with higher strain localization at the trench and in the orogen on top of the flat-slab (+25 and 38%, Figure 7). In S4b, although no horizontal velocity is prescribed, the strain rate is higher in the orogen on top of the flat slab (+30%) and lower elsewhere. To investigate the effect of topography on the strain distribution, we ran two alternative models inhibiting topographic growth, with and without plate velocities (models S4b-c; Figure 6j-l). In the model with plate velocities (S4c) the strain rate is higher at the trench and the orogen on top of the flat-slab (+128 and 101%), and it is more diffuse and lower in the foreland of the shallow and steep-subduction domains (-23% and -36%). Without plate velocities (S4d), the strain rate only localizes in a narrow corridor along the orogen and otherwise decreases elsewhere.

3.2.4 Velocity boundary conditions (S5a-d)

Varying the prescribed boundary velocity allows us to determine the contribution of each plate to the intensity of strain localization in the overriding plate. In model S5a (Figure 6m), where velocities are only prescribed to the overriding plate (1cm yr^{-1}; Figure 6m), the intensity of the deformation in the foreland is lower by 58 to 83% in all domains compared to model S1 (Figure 7) because the deformation slightly localizes at the trench in specific places. In model S5b, where the overriding plate does not advance trenchward, the deformation decreases everywhere by 15 to 30%, likely because the strain efficiently localizes in the orogen and the foreland (Figure 6n). Models S5c and S5d (Figure 6n-o) show that a deformation intensity similar to the reference model can be reached if the total convergence velocity is applied to either the lower or the upper plates. Overall, a fast convergence rate controls the intensity of the deformation and its localization. In these models, the contribution of the subducting plate velocity seems more important than that of the overriding plate, although a fast overriding plate velocity (S5d) can lead to similar degree of deformation as in the reference model. The strain-rate distribution in the overriding plate does not depend on the side of the prescribed velocity. The models that prescribe velocity from the west with the subducting plate (S5c) or from the east with the overriding upper plate (S5d) show similar structures and patterns (Figure 6o-p).

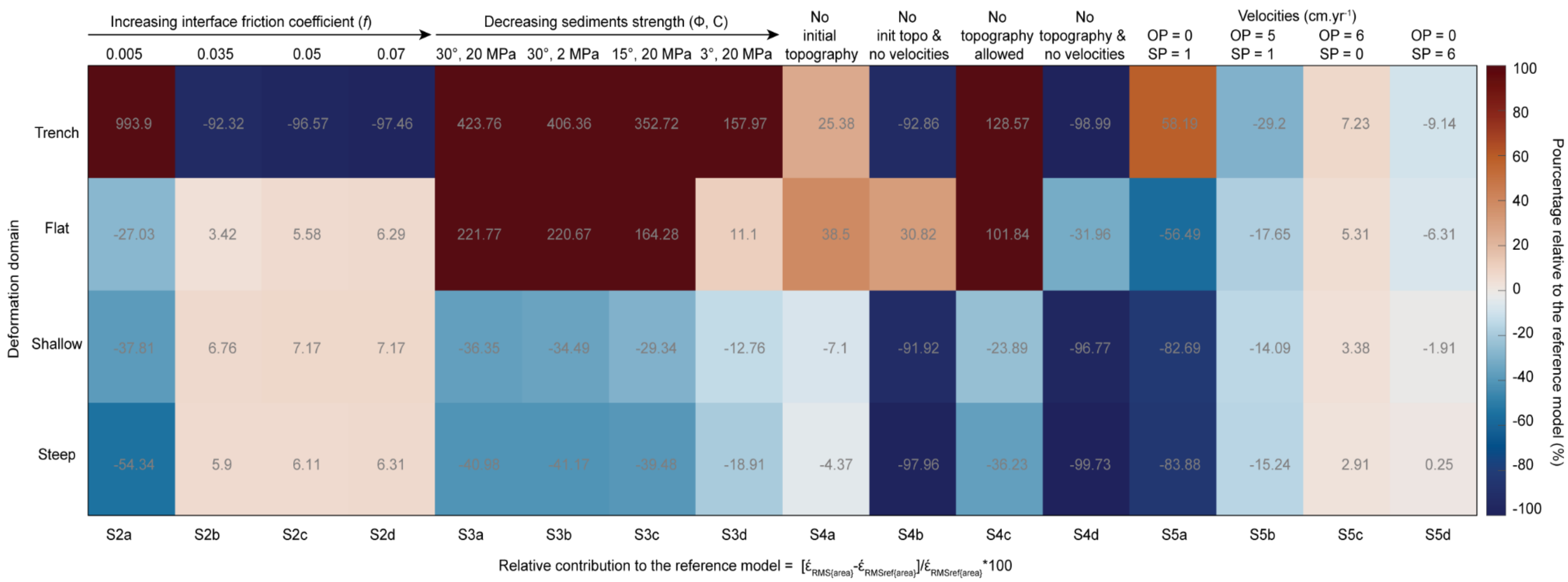

Figure 4 Relative surface strain-rate difference between the reference and the model variants. Relative change of strain rate in percentage $[\dot{\varepsilon}\mathrm{RMS(area)} - \dot{\varepsilon}\mathrm{RMSref(area)}] / \dot{\varepsilon}\mathrm{RMSref(area)} * 100$ with respect to the reference model in each deformation domain for each model variant.

4. Discussion

To analyze the roles of inherited heterogeneities in the continental plate and oceanic plate geometry we assess the relative contribution of the overriding plate strength with respect to strain localization along-strike. We first compare the distribution of modeled strain-rate patterns with the mapped structures (Section 4.1). Next, we discuss each of the tested key factors and how they affect the strength in our model, and their contribution to strain localization. We then discuss the role of shallow and deep-seated structures (e.g., sediment strength, topography, and the thermal state and thickness of the lithosphere, section 4.2, Figure 8). Finally, we examine the effect of slab geometry (flat, shallow, and steep subduction) regarding the distribution and style of deformation in the foreland (section 4.3).

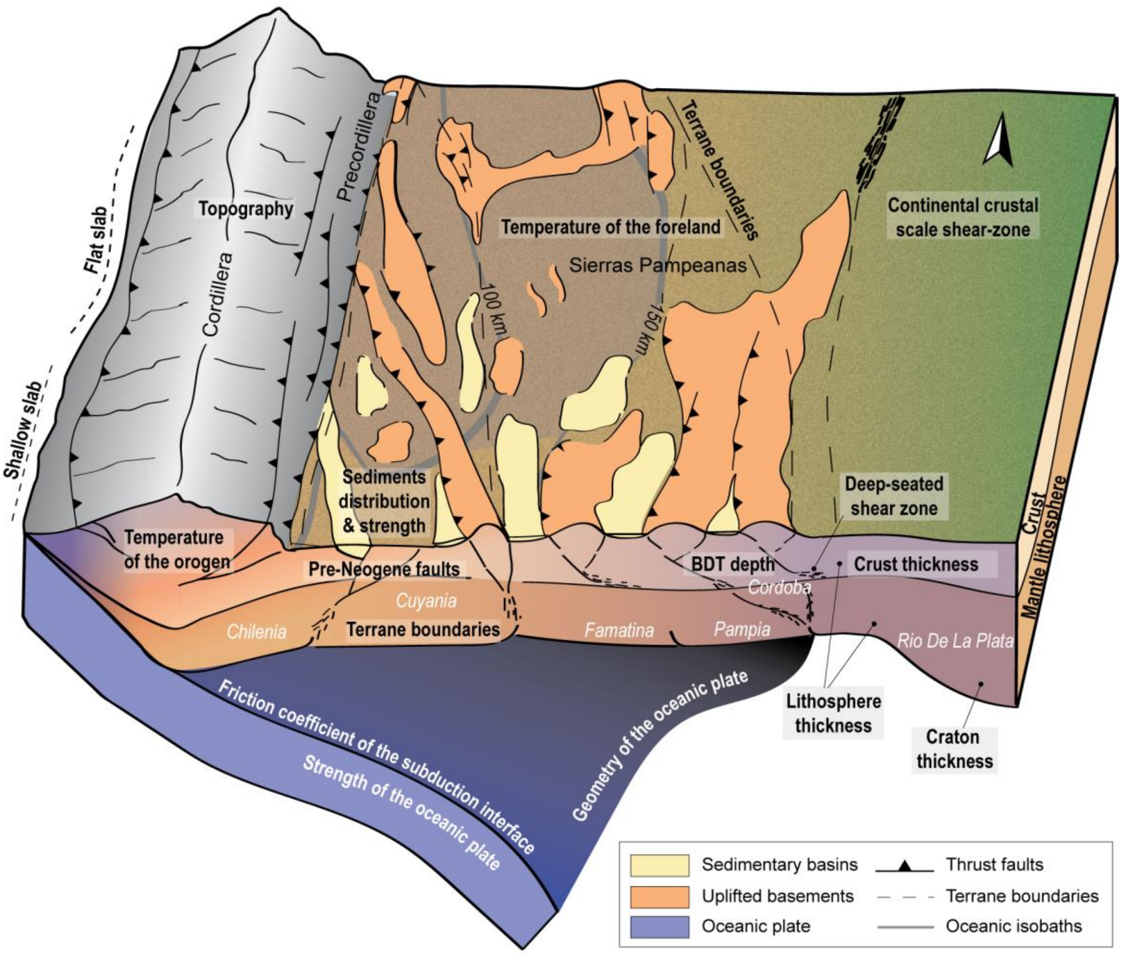

Figure 8 Schematic 3D diagram showing the possible processes (in bold) and inherited structures that can affect strain localization and the tectonic foreland deformation style in the Sierras Pampeanas.

4.1 Correlation with mapped structures

Our modelling results can be compared with observed surface faulting. Although we do not implement faults in the models explicitly, sediment accumulation is partly associated with their activity. In the investigated area, Mesozoic deposits are controlled by normal-fault bounded, extensional basins, while reverse faults cause sediment accumulation at their footwalls. Therefore, sediment strength and pre-existing faults related to a different kinematic regime may strongly affect the location of deformation and the reactivation of shallow inherited faults, which explains why structures resulting from the strain-rate map of the reference model are spatially well correlated with exposed faults (Figure 4a-b). In particular, the strain-rate distribution in the reference model correlates with Quaternary faults located at the front of the orogen in the foreland fold-and-thrust belts (e.g., Malargue, San Rafael FTB), at the borders of the basins (e.g., Cuyo Basin), and with the faults uplifiting the Sierras Pampeanas basement blocks. In some cases, inherited Pre-Andean structures have been reactivated that were associated with the amalgamation of Paleozoic crustal terranes at the western margin of Gondwana (Introcaso & Ruiz, 2001; Vietor & Echtler, 2006; Ortiz et al., 2021). For instance, faults associated with the Desaguadero-Bermejo lineament (DBL) close to the Sierra Valle Fértil in the western Sierras Pampeanas (Figure 4b, Introcaso & Ruiz, 2001) are associated with structures related to the Ordovician collision of the Cuyania and Pampia terranes (Ramos, 2010). This strike-slip fault was reactivated during the Neogene (Introcaso & Ruiz, 2001). The model also predicts the reactivation of the Transbrazilian lineament (TBL), a major Proterozoic transpressive shear zone that borders the thicker mantle lithosphere of the Rio de la Plata craton (Figure 4b, Cordani et al., 2013; Casquet et al., 2018). In contrast, the forearc is subjected to a low degree of deformation and acts as a rigid body (Tassara & Yáñez, 2003; Tassara, 2005; Hackney et al., 2006), although previous studies have shown that the forearc experienced a certain degree of Quaternary deformation (González et al., 2003; Melnick et al., 2006; Regard et al., 2010). The mobility of the forearc is controlled by the long-term weakening associated with strain partitioning that is caused by oblique plate convergence (Melnick et al., 2006; Rosenau et al., 2006; Eisermann et al., 2021), which is not considered in our model. Other regions that exhibit a low degree of deformation include the foreland above the flat-slab segment (Figure 5a) and the back-arc in the steep-slab segment (Figure 5c). In the latter case, most of the deformation is related to pre-Neogene structures (e.g., Folguera & Zárate, 2009).

4.2 Upper-plate control on strain localization

The strength of the overriding plate controls strain localization and results from contributions exerted by the frictional (brittle) and viscous (ductile) strength (Babeyko et al., 2006; Mouthereau, 2013; Jammes & Huismans, 2012; Liu et al., 2022). Several processes may weaken the plate and influence the localization of deformation. In our study we distinguished between shallow and deep-seated contributors, depending on their control on the frictional and viscous strength, respectively.

An important component of the stress is transmitted through the frictional regime (Figure 5), thus shallow contributors can significantly affect strain localization through frictional weakening. The variations in frictional strength are related to the tectonic history of the region, and are modulated by several features. These include the sediment strength relative to the underlying structures (Babeyko et al., 2006; Erdős et al., 2015; Mescua et al., 2016; Liu et al., 2022), the presence of inherited (Pre-Andean) faults and fabrics and their orientation with respect to the convergence direction (Allmendinger et al., 1983; Kley, 1999; Kley & Monaldi, 2002), and topography (Molnar & Tapponnier, 1975; Chen & Molnar, 1983; Stüwe, 2007; Mareschal & Jaupart, 2011; Liu et al., 2022). In turn, the deep-seated contributors are those affecting the strength of the crust and the lithospheric mantle through temperature variations. The extent to which shallow and deep-seated contributors interact and affect the strength of the overriding plate in the SCA, is discussed in the following sections.

4.2.1 Shallow structures

Previous studies have shown the important role of the thickness and strength of sediments in shallow strain localization (Babeyko et al., 2006; Erdős et al., 2015; Mescua et al., 2016; Liu et al., 2022). In the Central Andes, the presence of mechanically weak and porous Palaeozoic sediments in the foreland spatially correlates with a change of deformational style from thin-skinned to thick-skinned deformation in strain rate map the transition between the Subandean FTB and the broken foreland province of the Santa Barbara System of northwestern Argentina (Allmendinger et al., 1983; McGroder et al., 2015; Pearson et al., 2013). Previous numerical models have shown that a low friction coefficient of the sediments (<0.05) promotes asymmetric deformation, a simple-shear shortening and thin-skinned deformation style, which may constitute a necessary condition to initiate foreland underthrusting of the Brazilian Shield (Sobolev et al., 2006; Liu et al., 2022; Pons et al., 2022). Additionally, Ibarra et al. (2019) have proposed that deformation tends to localize within the areas with large lateral variations of crustal strength, such as the foreland where a thick sedimentary layer is present. Our results show that the distribution of sediments inherited from past tectonic events largely control shallow strain localization (Figure 2d, Figure 6 and 7, S3a-c). Sediments tend to accumulate at the footwall of the faults or close to uplifted basement blocks. In addition, some of these depocenters had already formed during Palaeozoic to early Mesozoic extension, which could also have weakened the basement (Mescua et al., 2016). In our model, efficient simple-shear shortening is favored by the thick sedimentary layer of the foreland basin, which generates a detachment fault connecting plastic (brittle) and viscous strain rates in the upper and lower crust, respectively (Figure 5). In case that such a connection is not possible, shortening is accommodated by pure shear and deformation distributes along multiple symmetrical faults (Figure 5). Model variations S3a-d show that weaker sediments are required to localize the deformation along specific discrete faults and structures (e.g., at the borders of the uplifted basement blocks or the Bermejo basin; Figure 6, S3c). Conversely, strong sediments (e.g. model S3a) with a small strength contrast with respect to the upper crust lead to a broad, diffuse shear zone in the foreland above the flat-slab segment (Figure 6e-h).

An additional factor that is proposed to exert major control on strain localization is topography. In the orogen, the gravitational potential energy constitutes an important resistive force to orogenic growth (Molnar & Tapponnier, 1975; Chen & Molnar, 1983; Stüwe, 2007; Mareschal & Jaupart, 2011; Liu et al., 2022). If horizontal forces are not sufficiently strong to overcome gravitational stresses exerted by the topography of the orogen, the horizontal stresses migrate laterally to the periphery of the orogen and strain localized in the foreland. This effect is highlighted in Model S4c (Figure 6k), where no topography is allowed to grow, thus the deformation is less efficiently transmitted and localized in the weak areas of the foreland. Topography can also exert an indirect effect on deformation localization if the uplifted foreland basement blocks are bounded by faults and adjacent sediment depocenters, which promotes the localization of deformation as discussed previously in this section. In the alternative models without initial topography (Model S4a, Figure 6i) or where no topography is allowed to grow (Model S4c, Figure 6k), the removal of the orogenic load fosters strain localization in the orogen. Additionally, the models without prescribed velocities (Models S4b, Figs. 6j and l) indicate that a low portion of the strain rate in the northern orogen in the model could result from some dynamic effect of the flowing mantle asthenosphere.

4.2.2 Effect of deep-seated inherited structures.

The viscous strength of the continental crust and mantle lithosphere strongly depends on their composition, inherited thickness and on their thermal state because of the strong dependence of viscosity on temperature (Sippel et al., 2017; Anikiev et al., 2020; Ibarra et al., 2021; Rodriguez Piceda et al., 2022b). In the orogen, higher temperatures decrease the depth of the brittle-ductile transition favoring viscous deformation and crustal flow which may facilitate the connection with the plastically deforming foreland sediments, ultimately promoting simple-shear deformation (Liu et al., 2022). Additionally, for an orogenic crust of more than 60 km thickness, simple shear is almost always the preferred mode of foreland deformation (Liu et al., 2022). In contrast, a cold, rigid lithosphere can act as an indenter by transmitting horizontal stresses to its front, localizing the deformation at the transition between strong and weak domains (Calignano et al., 2015; Tesauro et al., 2015; Rodriguez Piceda et al., 2022b, Ibarra et al., 2021).

The lithospheric thermal field in the SCA is the result of the contributions from the compositional and thickness configuration of the lithospheric layers and the basal lithospheric heat flow (Rodriguez Piceda et al., 2022a). The crustal thermal field mainly depends on the volumetric heat capacity of the radiogenic upper crust, whereas the thermal field of the mantle is strongly perturbed by the cooling effect of the subducting slab, which changes as a function of the slab dip and geometry (Rodriguez Piceda et al., 2022a). In the northern part of the orogen, the effect of the thick felsic radiogenic crust (Figure 2) overprints the cooling effect of the flat slab (Rodriguez Piceda et al., 2022a). Therefore, the northern part of the orogen would be expected to deform actively, which contradicts our model results and the lack of observed seismicity in the area (ISC catalog, Rodriguez Piceda et al., 2022b; Figure S2). To explain this apparent contradiction (i.e., no deformation of the upper plate), an additional mechanism must be invoked (further discussed in Section 4.3). Conversely, the lithosphere in the northern foreland is characterized by a thinner radiogenic upper crust (Figure 2) which does not overprint the cooling effect of the flat-slab, thus resulting in a colder and stronger lithosphere. This strengthening allows for an efficient stress transmission from the oceanic plate to the continental plate between western and eastern domain above the flat-slab segment. Additionally, the strong, thick cratonic domain (Figure 2f) allows for an efficient transmission of stresses to the west. Consequently, the deformation localizes at the eastern edge of the broken foreland where the effects of forces applied from the subducted plate and the cratonic part of the continental plate meet (Figure 5a). Finally, the deformation is intensified by the overlying weak sediments.

Other deep lithospheric processes, such as eclogitization of the crust and delamination of the lithospheric mantle, are not considered in our models, they could also weaken the overriding plate and facilitate strain localization (Babeyko et al., 2006; Sobolev et al., 2006). However, in the southern Central Andes, there is no evidence of delamination and extensive eclogitization below the Western Sierras Pampeanas and Precordillera (Alvarado et al., 2007, 2009; Ammirati et al., 2013; 2015; 2018; Gilbert et al., 2006b; Marot et al., 2014). Thick, warm orogenic crust (>~45 km) can also be subjected to intracrustal convection and partial melting, further weakening the overriding plate (Babeyko et al., 2006). Nevertheless, such thickness values are only reached (Assumpção, 2013; Rodriguez Piceda et al., 2021) where the lack of volcanism between ~27°S - 33°S (Figure 1) indicates a decrease in the lithospheric basal heat flux during the last ~6 Ma (Barazangi & Isacks, 1976; Isacks et al., 1982; Jordan et al., 1983; Kay et al., 1987; 1991; Jordan et al., 1993; Ramos et al., 2002a; Ramos & Folguera, 2009; Rodriguez Piceda et al., 2022b), preventing partial melting and crustal convection in the southern Central Andes.

4.3 Lower-plate control on strain localization

In the SCA, the role of the flat-slab on the stress regime and the localization of deformation in the upper plate is a matter of ongoing debate (Jordan et al., 1983; Gutscher et al., 2000; Folguera et al., 2009; Gutscher, 2018; Horton, 2018; Martinod et al., 2020). Along the tectonically active Pacific rim steep subduction is associated with a low degree of coupling, upper-plate extension, and back-arc spreading (Mariana type), while low-angle subduction cause close plate coupling, upper-plate compression and shortening (Chile type) (Barazangi & Isacks, 1976; Uyeda & Kanamori, 1979; Ramos & Folguera, 2009; Horton, 2018). Eastward-directed compression in the Central Andes is driven by basal shear stress exerted by the underlying flat-slab (Gutscher et al., 2000). Additionally, the passage of the flat-slab weakens the overriding plate mechanically by scraping the continental lithospheric mantle, ('bulldozed mantle-keel' model, Liu & Currie, 2016; Gutscher, 2018; Axen et al., 2018) and thermally by exposing the remaining lithosphere to the warmer asthenosphere (Isacks, 1988). More recent studies, however, have emphasized that the stress regime of the overriding plate is probably more influenced by the velocity difference between the overriding plate and the trench rather than by the subduction angle (Lallemand et al., 2008; Faccenna et al., 2017, 2021). The velocity of trench retreat can be perturbed by a rapid change in the subduction angle, which can be caused by the interaction between the slab and the mantle transition zone (Čížková & Bina, 2013; Cerpa et al., 2015; Briaud et al., 2020; Pons et al., 2022). The absolute motion of the South American plate prescribed in model S1 is considered to be the driving force of the Andean orogeny (Sobolev and Babeyko, 2005; Husson et al., 2008; Martinod et al., 2010); nevertheless, when viewed at shorter geological timescales, model variants such as model S5b-d, illustrate that a similar strain rate as in model S1 can be achieved with a different redistribution of plate velocities while maintaining a similar convergence rate (Figure 6 and 7). This implies that at shorter timescales, the parameter convergence rate is potentially more important than absolute plate velocity.

In our simulations, the subduction angle of the oceanic slab also controls the distribution of strain localization in the upper plate. The flat slab propagates stresses eastward causing shortening to take place in front of the flat slab, as proposed by the ‘bulldozed mantle-keel’ models (‘slab bulldozing’, Gutscher, 2018; Axen et al., 2018). Strain localization could be favoured by inherited crustal-scale structures such as the Transbrazilian lineament in the SCA (see Section 4.2.1). Conversely, the cratonic domain also transmits horizontal stresses westward across the continental plate and amplifies the intensity of deformation (Figure 5). Interestingly, our results predict almost no deformation in the upper plate overlying the flat-slab segment (27°S–32°S). This is consistent with limited seismic activity observed in the orogenic domain overlying the flat slab segment (Figure S2). We suggest that this is the result of upper-plate strengthening at these latitudes due to cooling as discussed above (cf. section 4.2.2) and caused by the underplated oceanic slab at the base of the continental lithosphere. The notion that the upper plate is shielded from deformation in the flat-slab segment is also supported by the decrease in shortening in the Precordillera at ~9Ma at 30°S following the arrival of the Juan Fernandez Ridge at 12 Ma (Yáñez et al., 2001; Allmendinger & Judge, 2014; Bello-González et al., 2018).

The colder subduction interface along the flat-slab segment (Figure 5a) also contributes to an increase in the coupling between the plates, and can locally reach shear stresses >35 MPa (Figure S4). Moreover, the low temperatures of the subduction interface combined with its low frictional strength could deepen the BDT of this discontinuity to 100 km depth (Figure 5a). The shear stresses at the plate interface decrease southward, which is supported by the increased thickness of the trench-fill sediments south of 33°S (Bangs & Cande, 1997; Völker et al., 2013). A comparison with the average shear stress at the plate interface suggested by Lamb & Davis (2003; Figure S4) shows that our reference model (f=0.015) may underestimate the shear stress at the flat-slab interface, whereas model S2d (f=0.07) may overestimate it.

In contrast to the flat-slab segment, deformation in the steep-slab segment (36°S–40°S) localizes along the front of the orogen, which shows that deformation cannot be efficiently propagated to the eastern domain if the oceanic slab is steeply dipping. Alternatively, the transition between the steep and flat-slab geometry results in the formation of an intermediary shallow segment (32°S–36°S). Above this segment a large crustal shear zone develops in the broken foreland that results from the offset of strain localization between the flat and steep slabs. In such a scenario deformation takes place via multiple faults that border the basement ranges of the Sierras Pampeanas (Figure 5d), and the strain localization along these faults is enhanced by the presence of weak sediments (Models S2, Figure 6a-d). From a dynamic point of view, we suggest that the shallowing of the slab generates crustal contraction prior to slab flattening in response to a large transpressive shear zone in the southern Sierras Pampeanas. Accordingly, deformation could be accommodated by a combination of strike-slip deformation at the borders of the uplifted basement blocks and block rotation. This mechanism, that we name “flat-slab conveyor”, is further investigated in a related publication (Pons et al., 2023, related manuscript).

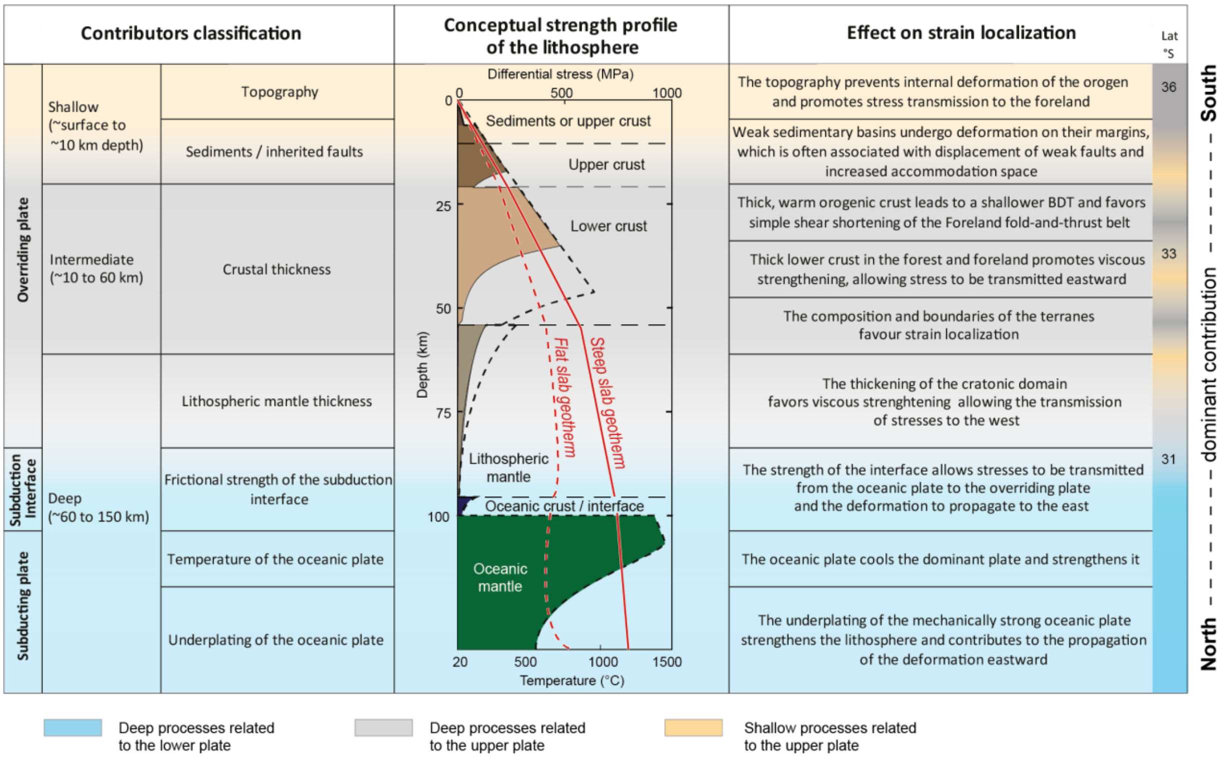

Figure 9 Summary of the main contributors to strain localization in the Southern Central Andes indicates a north-south-directed switch from deep to shallow-seated factors.

5. Conclusions

Using 3D data-driven geodynamic subduction modeling, we analyzed the relative contribution of subducting plate geometry and shallow and deep-seated crustal-scale and lithospheric structures of the overriding plate on strain localization in the SCA. Our modelling results provide a better understanding the Cenozoic interaction between the Pampean flat slab and the South American plate in the region of the southern Central Andes between 27° and 32°S and within the transition to a steeper subduction segment farther south. The flat slab controls upper-plate deformation in the northern part of the SCA by strengthening the lithosphere of the upper-plate and by cooling the overriding plate through underplating, thus shielding the upper plate of the flat-slab subduction system from pronounced deformation. Consequently, deformation propagates toward the eastern edge of the flat slab by a bulldozing effect. This deformation is accommodated in the eastern broken foreland, where the slab is already dipping steeply.

The inherited structures in the overriding plate contribute to the strain localization in multiple different ways. (i) In the compressional Cenozoic setting of the flat-slab region sediment distribution can be viewed as a proxy for the distribution of major faults, because depocenters usually form at their footwalls. Weaker sediments, and therefore weaker faults, significantly intensify deformation in the flat-slab segment. (ii) Inherited crustal-scale fault zones, such as the TBL located within the transition to the cratonic domain, may be preferentially reactivated and localize deformation as seen in the eastern Sierras Pampeanas. (iii) The localization of deformation in the forearc may be controlled by strain partitioning and long-term strain weakening related to the obliquity of convergence. (iv) A thick crust may control the temperature of the continental crust due to the contribution of radiogenic heating, thus affecting the depth of the brittle-ductile transition (BDT). For a thicker felsic crust the BDT is shallower, which promotes the development of deep-seated, asymmetric décollements and simple-shear shortening in the fold-and-thrust belts. In contrast, a thinner upper continental crust causes a deeper BDT as observed in the Sierras Pampeanas and fosters the activity of multiple symmetric faults and pure-shear shortening. (v) Surface topography may also exert a significant influence on strain localization within the orogen by transmitting horizontal stresses toward the foreland.

6. Acknowledgements

This research was funded by the DeutscheForschungsgemeinschaft (DFG) and the Federal State of Brandenburg under the guidance of the International Research Training Group IGK2018 “SuRfAce processes, TEctonics and Georesources: The Andean foreland basin of Argentina” (STRATEGy DFG 373/34-1). The authors thank the Computational Infrastructure for Geodynamics (geodynamics.org), which is funded by the National Science Foundation under award EAR-0949446 and EAR-1550901, for supporting the development of ASPECT. The computations of this work were supported by the North-German Supercomputing Alliance (HLRN). Stephan V Sobolev was funded by the ERC Synergy Grant Project MEET (Monitoring Earth Evolution through Time, Grant 856555). The authors thank Corinna Kallich for her comments and suggestions on the design of the figures.

7. Data availability

The input files to reproduce the results of this paper are available at the following link https://dataservices.gfz-potsdam.de/panmetaworks/review/ff12e9fd34522339dfaf9c7e6bb578a085072f2addfc921cf09b470 10c4213ee/ (https://doi.org/10.5880/GFZ.2.5.2023.001, Temporary link for review from the GFZ metadata service). Figures in the paper were made with Paraview and Illustrator. The color scales were taken from Crameri (10.5281/zenodo.5501399).

8. Code availability

The ASPECT code is open source and hosted on github https://github.com/geodynamics/aspect. The models were run with the ASPECT version 2.3.0-pre built with the 9.2.0 version of Deal.ii. We have modified the main ASPECT branch to implement new custom plugins necessary for the model set up and the postprocessing accessible at https://github.com/Minerallo/aspect/tree/Paper_Data_driven_model_Southern_Andes.

9. Author contributions

Michaël Pons: Conceptualization, software, Formal Analysis, Data curation, Investigation, Visualization, Writing - original draft, Writing - review & editing, Constanza Rodriguez Piceda : Conceptualization, Formal Analysis, Data curation, Investigation, Visualization, Writing - original draft, Writing - review & editing, Stephan V Sobolev: Methodology, Supervision, Validation, Writing - review & editing, Magdalena Scheck-Wenderoth : Methodology, Supervision, Validation, Writing - review &

editing, Manfred Strecker : Project administration, Funding acquisition, Supervision, Validation, Writing - review & editing

10. Supplementary information

Supplementary text S1, Supplementary figures 1 to 4.

11. References

Allmendinger, R. W., & Gubbels, T. (1996). Pure and simple shear plateau uplift, Altiplano-Puna, Argentina and Bolivia. *Tectonophysics*, *259*(1-3 SPEC. ISS.), 1-13. https://doi.org/10.1016/0040-1951(96)00024-8

Allmendinger, R. W., Jordan, T. E., Kay, S. M., & Isacks, B. L. (1997). The evolution of the Altiplano-Puna plateau of the Central Andes. *Annu Rev Earth Planet Sci*, *25*, 139-174. https://doi.org/10.1146/annurev.earth.25.1.139

Allmendinger, R. W., & Judge, P. A. (2014). The Argentine Precordillera : A foreland thrust belt proximal to the subducted plate. *Geosphere*, *10*(6), 1203-1218. https://doi.org/10.1130/GES01062.1

Allmendinger, R. W., Ramos, V. A., Jordan, T. E., Palma, M., & Isacks, B. L. (1983). Paleogeography and Andean structural geometry, northwest Argentina. *Tectonics*, *2*(1), 1-16. https://doi.org/10.1029/TC002i001p00001

Alvarado, P., Barrientos, S., Saez, M., Astroza, M., & Beck, S. (2009). Source study and tectonic implications of the historic 1958 Las Melosas crustal earthquake, Chile, compared to earthquake damage. *Physics of the Earth and Planetary Interiors*, *175*(1), 26-36. https://doi.org/10.1016/j.pepi.2008.03.015

Alvarado, P., Beck, S., & Zandt, G. (2007). Crustal structure of the south-central Andes Cordillera and backarc region from regional waveform modeling. *Geophysical Journal International*, *170*(2), 858-875. https://doi.org/10.1111/j.1365-246x.2007.03452.x

Amante, C., & Eakins, B. (2009). *ETOPO1 1 Arc-Minute Global Relief Model : Procedures, data sources and analysis*. https://doi.org/10.7289/V5C8276M

Ammirati, J. B., Alvarado, P., & Beck, S. (2015). A lithospheric velocity model for the flat slab region of Argentina from joint inversion of Rayleigh wave phase velocity dispersion and teleseismic receiver functions. *Geophysical Journal International*, *202*(1), 224. https://doi.org/10.1093/gji/ggv140

Ammirati, J.-B., Alvarado, P., Perarnau, M., Saez, M., & Monsalvo, G. (2013). Crustal structure of the Central Precordillera of San Juan, Argentina (31°S) using teleseismic receiver functions. *Journal of South American Earth Sciences*, *46*, 100-109. https://doi.org/10.1016/j.jsames.2013.05.007

Ammirati, J.-B., Venerdini, A., Alcacer, J. M., Alvarado, P., Miranda, S., & Gilbert, H. (2018). New insights on regional tectonics and basement composition beneath the eastern Sierras Pampeanas (Argentine back-arc region) from seismological and gravity data. *Tectonophysics*, *740-741*, 42-52. https://doi.org/10.1016/j.tecto.2018.05.015

Anikiev, D., Cacace, M., Bott, J., Gomez Dacal, M. L., & Scheck-Wenderoth, M. (2020). Influence of Lithosphere Rheology on Seismicity in an Intracontinental Rift : The Case of the Rhine Graben. *Frontiers in Earth Science*, *8*, 492. https://doi.org/10.3389/feart.2020.592561

Araneda, M., Asch, G., Bataille, K., Bohm, M., Bruhn, C., Giese, P., Lüth, S., Quezada, J., Rietbrock, A., & Wigger, P. (2003). A crustal model along 39° S from a seismic refraction profile-ISSA 2000. *Revista geológica de Chile*, *30*(1), 83-101. http://dx.doi.org/10.4067/S0716-02082003000100006

Assumpção, M., Feng, M., Tassara, A., & Julià, J. (2013). Models of crustal thickness for South America from seismic refraction, receiver functions and surface wave tomography. *Tectonophysics*, *609*, 82-96. https://doi.org/10.1016/j.tecto.2012.11.014

Axen, G. J., van Wijk, J. W., & Currie, C. A. (2018). Basal continental mantle lithosphere displaced by flat-slab subduction. *Nature Geoscience*, *11*(12), Art. 12. https://doi.org/10.1038/s41561-018-0263-9

Babeyko, A. Y., & Sobolev, S. V. (2005). Quantifying different modes of the late Cenozoic shortening in the central Andes. *Geology*, *33*(8), 621-624. https://doi.org/10.1130/G21126.1

Babeyko, A. Y., Sobolev, S. V., Vietor, T., Oncken, O., & Trumbull, R. B. (2006a). Numerical Study of Weakening Processes in the Central Andean Back-Arc. *The Andes - Active subduction orogeny*, 495-512. https://doi.org/10.1007/978-3-540-48684-8

Bangerth, W., Dannberg, J., Fraters, M., Gassmoeller, R., Glerum, A., Heister, T., & Naliboff, J. (2021). *ASPECT v2.3.0*. Zenodo. https://doi.org/10.5281/zenodo.5131909

Bangs, N. L., & Cande, S. C. (1997). Episodic development of a convergent margin inferred from structures and processes along the southern Chile margin. *Tectonics*, *16*(3), 489-503. https://doi.org/10.1029/97TC00494

Barazangi, M., & Isacks, B. L. (1976). Spatial distribution of earthquakes and subduction of the Nazca plate beneath South America. *Geology*, *4*(11), 686-692. https://doi.org/10.1130/0091-7613(1976)4<686:SDOEAS>2.0.CO;2

Barrionuevo, M., Liu, S., Mescua, J., Yagupsky, D., Quinteros, J., Giambiagi, L., Sobolev, S. V., Piceda, C. R., & Strecker, M. R. (2021). The influence of variations in crustal composition and lithospheric strength on the evolution of deformation processes in the southern Central Andes : Insights from geodynamic models. *International Journal of Earth Sciences 2021 110:7*, *110*(7), 2361-2384. https://doi.org/10.1007/S00531-021-01982-5

Becker, T. W., Schaeffer, A. J., Lebedev, S., & Conrad, C. P. (2015). Toward a generalized plate motion reference frame. *Geophysical Research Letters*, *42*(9), 3188-3196. https://doi.org/10.1002/2015GL063695

Bello-González, J. P., Contreras-Reyes, E., & Arriagada, C. (2018). Predicted path for hotspot tracks off South America since Paleocene times : Tectonic implications of ridge-trench collision along the Andean margin. *Gondwana Research*, *64*, 216-234. https://doi.org/10.1016/j.gr.2018.07.008

Bovy, B. (2021). *fastscape-lem/fastscape : Release v0.1.0beta3*. Zenodo. https://doi.org/10.5281/zenodo.4435110

Braun, J., & Willett, S. D. (2013). A very efficient O(n), implicit and parallel method to solve the stream power equation governing fluvial incision and landscape evolution. *Geomorphology*, *180-181*, 170-179. https://doi.org/10.1016/j.geomorph.2012.10.008

Briaud, A., Agrusta, R., Faccenna, C., Funiciello, F., & van Hunen, J. (2020). Topographic Fingerprint of Deep Mantle Subduction. *Journal of Geophysical Research: Solid Earth*, *125*(1), e2019JB017962. https://doi.org/10.1029/2019JB017962

Brocher, T. (2005). Empirical relations between elastic waves peeds and density in the Earth's crust. *Bull Seismol Soc Am*, *95*(6), 2081-2092. https://doi.org/10.1785/0120050077

Calignano, E., Sokoutis, D., Willingshofer, E., Gueydan, F., & Cloetingh, S. (2015). Strain localization at the margins of strong lithospheric domains : Insights from analog models. *Tectonics*, *34*(3), 396-412. https://doi.org/10.1002/2014TC003756

Casquet, C., Dahlquist, J. A., Verdecchia, S. O., Baldo, E. G., Galindo, C., Rapela, C. W., Pankhurst, R. J., Morales, M. M., Murra, J. A., & Mark Fanning, C. (2018). Review of the Cambrian Pampean orogeny of Argentina; a displaced orogen formerly attached to the Saldania Belt of South Africa? *Earth-Science Reviews*, *177*, 209-225. https://doi.org/10.1016/j.earscirev.2017.11.013

Cermak, V., & Rybach, L. (1982). 4.1.1 Introductory remarks. In G. Angenheister (Éd.), *Subvolume A: Vol. c* (p. 305-310). Springer-Verlag. https://doi.org/10.1007/10201894_62

Cerpa, N. G., Araya, R., Gerbault, M., & Hassani, R. (2015). Relationship between slab dip and topography segmentation in an oblique subduction zone : Insights from numerical modeling. *Geophysical Research Letters*, *42*(14), 5786-5795. https://doi.org/10.1002/2015GL064047

Chen, W.-P., & Molnar, P. (1983). Focal depths of intracontinental and intraplate earthquakes and their implications for the thermal and mechanical properties of the lithosphere. *Journal of Geophysical Research: Solid Earth*, *88*(B5), 4183-4214. https://doi.org/10.1029/JB088iB05p04183

Christensen, N. I., & Mooney, W. D. (1995). Seismic velocity structure and composition of the continental crust : A global view. *Journal of Geophysical Research: Solid Earth*, *100*(B6), 9761-9788. https://doi.org/10.1029/95JB00259

Čížková, H., & Bina, C. R. (2013). Effects of mantle and subduction-interface rheologies on slab stagnation and trench rollback. *Earth and Planetary Science Letters*, *379*, 95-103. https://doi.org/10.1016/j.epsl.2013.08.011

Contreras-Reyes, E., Grevemeyer, I., Flueh, E. R., & Reichert, C. (2008). Upper lithospheric structure of the subduction zone offshore of southern Arauco peninsula, Chile, at ∼38°S. *Journal of Geophysical Research*, *113*(B7), B07303. https://doi.org/10.1029/2007JB005569

Cordani, U., Pimentel, M., Ganade, C., & Fuck, R. (2013). The significance of the Transbrasiliano-Kandi tectonic corridor for the amalgamation of West Gondwana. *Brazilian Journal of Geology*, *43*, 583-597. https://doi.org/10.5327/Z2317-48892013000300012

Cristallini, E. O., & Ramos, V. A. (2000). Thick-skinned and thin-skinned thrusting in the La Ramada fold and thrust belt. *Tectonophysics*, *317*(3-4), 205-235. https://doi.org/10.1016/s0040-1951(99)00276-0

Dannberg, J., Eilon, Z., Faul, U., Gassmöller, R., Moulik, P., & Myhill, R. (2017). The importance of grain size to mantle dynamics and seismological observations. *Geochemistry, Geophysics, Geosystems*, *18*(8), 3034-3061. https://doi.org/10.1002/2017GC006944

Del Papa, C., Hongn, F., Powell, J., Payrola, P., Do Campo, M., Strecker, M. R., Petrinovic, I., Schmitt, A. K., & Pereyra, R. (2013). Middle Eocene-Oligocene broken-foreland evolution in the Andean Calchaqui Valley, NW Argentina : Insights from stratigraphic, structural and provenance studies. *Basin Research*, *25*(5), 574-593. https://doi.org/10.1111/BRE.12018

Dickinson, W. R., & Snyder, W. S. (1978). Plate tectonics of the Laramide orogeny. *Memoir of the Geological Society of America*, *151*, 355-366. https://doi.org/10.1130/MEM151-P355

Eisermann, J. O., Göllner, P. L., & Riller, U. (2021). Orogen-scale transpression accounts for GPS velocities and kinematic partitioning in the Southern Andes. *Communications Earth & Environment*, *2*(1), 167. https://doi.org/10.1038/s43247-021-00241-4

Erdős, Z., Huismans, R. S., & van der Beek, P. (2015). First-order control of syntectonic sedimentation on crustal-scale structure of mountain belts. *Journal of Geophysical Research: Solid Earth*, *120*(7), 5362-5377. https://doi.org/10.1002/2014JB011785

Fuentes, F., Horton, B. K., Starck, D., & Boll, A (2016). Structure and tectonic evolution of hybrid thick- and thin-skinned systems in the Malargüe fold-thrust belt, Neuquén basin, Argentina. *Geol Mag*, *153*(5-6), 1066-1084. https://doi.org/10.1017/s0016756816000583

Ibarra, F., Liu, S., Meeßen, C. (2019). 3D data-derived lithospheric structure of the Central Andes and its implications for deformation : Insights from gravity and geodynamic modelling. *Tectonophysics*, *766*, 453-468. https://doi.org/10.1016/j.tecto.2019.06.025

Faccenna, C., Becker, T. W., Holt, A. F., & Brun, J. P. (2021). Mountain building, mantle convection, and supercontinents : Holmes (1931) revisited. *Earth and Planetary Science Letters*, *564*.

Faccenna, C., Oncken, O., Holt, A. F., & Becker, T. W. (2017). Initiation of the Andean orogeny by lower mantle subduction. *Earth and Planetary Science Letters*, *463*, 189-201. https://doi.org/10.1016/J.EPSL.2017.01.041

Fairhead, J. D., & Maus, S. (2003). CHAMP satellite and terrestrial magnetic data help define the tectonic model for South America and resolve the lingering problem of the pre-break-up fit of the South Atlantic Ocean. *The Leading Edge*, *22*(8), 779-783. https://doi.org/10.1190/1.1605081

Fennell, L. M., Iannelli, S. B., Encinas, A., Naipauer, M., Valencia, V., & Folguera, A. (2019). Alternating contraction and extension in the Southern Central Andes (35°–37°S). *American Journal of Science*, *319*(5), 381-429. https://doi.org/10.2475/05.2019.02

Folguera, A., Naranjo, J. A., Orihashi, Y., Sumino, H., Nagao, K., Polanco, E., & Ramos, V. A. (2009). Retroarc volcanism in the northern San Rafael Block (34°-35°30’S), southern Central Andes : Occurrence, age, and tectonic setting. *Journal of Volcanology and Geothermal Research*, *186*(3-4), 169-185. https://doi.org/10.1016/J.JVOLGEORES.2009.06.012

Folguera, A., & Zárate, M. (2009). La sedimentación neógena continental en el sectorextrandino de Argentina central. *Revista de la Asociación Geológica Argentina*, *64*(4), 692-712.

Fraters, M. (2015). *Thermo-mechanically coupled subduction modelling with ASPECT Master ’ s thesis by Menno Fraters*. *April*. https://doi.org/10.13140/RG.2.1.1061.0720

Gans, C. R., Beck, S. L., Zandt, G., Gilbert, H., Alvarado, P., Anderson, M., & Linkimer, L. (2011). Continental and oceanic crustal structure of the Pampean flat slab region, western Argentina, using receiver function analysis : New high-resolution results. *Geophysical Journal International*, *186*(1), 45-58. https://doi.org/10.1111/J.1365-246X.2011.05023.X

Giambiagi, L., Mescua, J., Bechis, F., Tassara, A., & Hoke, G. (2012). Thrust belts of the southern Central Andes : Along-strike variations in shortening, topography, crustal geometry, and denudation. *Bulletin of the Geological Society of America*, *124*(7-8), 1339-1351. https://doi.org/10.1130/B30609.1

Giambiagi, L., Mescua, J., Heredia, N., Farías, P., García-Sansegundo, J., Fernández, C., Stier, C., Pérez, D., Bechis, F., Moreiras, M., & Lossada, A. (2014). Reactivation of Paleozoic structures during Cenozoic deformation in the Cordón del Plata and Southern Precordillera ranges (Mendoza, Argentina). *Journal of Iberian Geology*, *40*(2). https://doi.org/10.5209/rev_JIGE.2014.v40.n2.45302

Gilbert, H., Beck, S., & Zandt, G. (2006a). Lithospheric and upper mantle structure of central Chile and Argentina. *Geophysical Journal International*, *165*(1), 383-398. https://doi.org/10.1111/J.1365-246X.2006.02867.X

Gilbert, H., Beck, S., & Zandt, G. (2006b). Lithospheric and upper mantle structure of central Chile and Argentina. *Geophysical Journal International*, *165*(1), 383-398. https://doi.org/10.1111/j.1365-246X.2006.02867.x

Gleason, G. C., & Tullis, J. (1995a). A flow law for dislocation creep of quartz aggregates determined with the molten salt cell. *Tectonophysics*, *247*(1-4), 1-23. https://doi.org/10.1016/0040-1951(95)00011-B

Gleason, G. C., & Tullis, J. (1995b). A flow law for dislocation creep of quartz aggregates determined with the molten salt cell. *Tectonophysics*, *247*(1-4), 1-23. https://doi.org/10.1016/0040-1951(95)00011-B

Glerum, A., Thieulot, C., Fraters, M., Blom, C., & Spakman, W. (2018). Nonlinear viscoplasticity in ASPECT: Benchmarking and applications to subduction. *Solid Earth*, *9*(2), 267-294. https://doi.org/10.5194/SE-9-267-2018

Goetze, C., & Evans, B. (1979). Stress and temperature in the bending lithosphere as constrained by experimental rock mechanics. *Geophysical Journal of the Royal Astronomical Society*, *59*(3), 463-478. https://doi.org/10.1111/J.1365-246X.1979.TB02567.X

González, G., Cembrano, J., Carrizo, D., Macci, A., & Schneider, H. (2003). The link between forearc tectonics and Pliocene–Quaternary deformation of the Coastal Cordillera, northern Chile. *Journal of South American Earth Sciences*, *16*(5), 321-342. https://doi.org/10.1016/S0895-9811(03)00100-7

Gutscher, M. A., Spakman, W., Bijwaard, H., & Engdahl, E. R. (2000). Geodynamics of flat subduction : Seismicity and tomographic constraints from the Andean margin. *Tectonics*, *19*(5), 814-833. https://doi.org/10.1029/1999TC001152

Gutscher, M.-A. (2018). Scraped by flat-slab subduction. *Nature Geoscience*, *11*(12), 889-890. https://doi.org/10.1038/s41561-018-0264-8

Hackney, R. I., Echtler, H. P., Franz, G., Götze, H.-J., Lucassen, F., Marchenko, D., Melnick, D., Meyer, U., Schmidt, S., Tašárová, Z., Tassara, A., & Wienecke, S. (2006). The Segmented Overriding Plate and Coupling at the South-Central Chilean Margin (36–42°S). In O. Oncken, G. Chong, G. Franz, P. Giese, H.-J. Götze, V. A. Ramos, M. R. Strecker, & P. Wigger (Éds.), *The Andes* (p. 355-374). Springer Berlin Heidelberg. https://doi.org/10.1007/978-3-540-48684-8_17

Haines, P. W., Hand, M., & Sandiford, M. (2001). Palaeozoic synorogenic sedimentation in central and northern Australia : A review of distribution and timing with implications for the evolution of intracontinental orogens. *Australian Journal of Earth Sciences*, *48*(6), 911-928. https://doi.org/10.1046/j.1440-0952.2001.00909.x

Hamza, V. M., & Vieira, F. P. (2012). Global distribution of the lithosphere-asthenosphere boundary : A new look. *Solid Earth*, *3*(2), 199-212. https://doi.org/10.5194/se-3-199-2012

Hasterok, D., & Chapman, D. (2011). Heat production and geotherms for the continental lithosphere. *Earth and Planetary Science Letters*, *307*(1-2), 59-70. https://doi.org/10.1016/j.epsl.2011.04.034

Hayes, G. P., Moore, G. L., Portner, D. E., Hearne, M., Flamme, H., Furtney, M., & Smoczyk, G. M. (2018). Slab2, a comprehensive subduction zone geometry model. *Science*, *362*(6410), 58-61. https://doi.org/10.1126/science.aat4723

He, L., Hu, S., Huang, S., Yang, W., Wang, J., Yuan, Y., & Yang, S. (2008). Heat flow study at the Chinese Continental Scientific Drilling site : Borehole temperature, thermal conductivity, and radiogenic heat production. *Journal of Geophysical Research*, *113*(B2), B02404. https://doi.org/10.1029/2007JB004958

Heister, T., Dannberg, J., Gassmöller, R., & Bangerth, W. (2017). High accuracy mantle convection simulation through modern numerical methods—II: realistic models and problems. *Geophys J Int*, *210*(2), 833-851. https://doi.org/10.1093/gji/ggx195

Hirth, G., & Kohlstedt, D. (2004). Rheology of the upper mantle and the mantle wedge : A view from the experimentalists. *Geophysical Monograph Series*, *138*, 83-105. https://doi.org/10.1029/138GM06

Hongn, F., Papa, C. del, Powell, J., Petrinovic, I., Mon, R., & Deraco, V. (2007). Middle Eocene deformation and sedimentation in the Puna-Eastern Cordillera transition (23°-26°S) : Control by preexisting heterogeneities on the pattern of initial Andean shortening. *Geology*, *35*(3), 271-274. https://doi.org/10.1130/G23189A.1

Horton, B. (2018). Tectonic regimes of the Central and Southern Andes : Responses to variations in plate coupling during subduction. *Tectonics*, *37*(2), 402-429. https://doi.org/10.1002/2017tc004624

Horton, B. K., Fuentes, F., Boll, A., Starck, D., Ramirez, S. G., & Stockli, D. F. (2016). Andean stratigraphic record of the transition from backarc extension to orogenic shortening : A case study from the northern Neuquén Basin, Argentina. *J S Am Earth Sci*, *71*, 17-40. https://doi.org/10.1016/j.jsames.2016.06.003

Husson, L., Conrad, C. P., & Faccenna, C. (2008). *Tethyan closure , Andean orogeny , and westward drift of the Paci fi c Basin*. *271*, 303-310. https://doi.org/10.1016/j.epsl.2008.04.022

Ibarra, F., Meeßen, C., Liu, S., Prezzi, C., & Sippel, J. (2018). *Density structure and rheology of northern Argentina : From the Central Andes to the foreland basin*. *20*(April), 16756-16756.

Ibarra, F., Prezzi, C. B., Bott, J., Scheck-Wenderoth, M., & Strecker, M. R. (2021). Distribution of Temperature and Strength in the Central Andean Lithosphere and Its Relationship to Seismicity and Active Deformation. *Journal of Geophysical Research: Solid Earth*, *126*(5). https://doi.org/10.1029/2020JB021231

Introcaso, A., & Ruiz, F. (2001). Geophysical indicators of Neogene strike-slip faulting in the Desaguadero–Bermejo tectonic lineament (northwestern Argentina). *Journal of South American Earth Sciences*, *14*(7), 655-663. https://doi.org/10.1016/S0895-9811(01)00057-8

Isacks, B. (1988). Uplift of the Central Andean Plateau and bending of the Bolivian Orocline. *J Geophys Res*, *93*(B4), 3211. https://doi.org/10.1029/jb093ib04p03211

Isacks, B., Jordan, T., Allmendinger, R., & Ramos, V. (1982). La segmentación tectónica de los Andes Centrales y su relación con la Placa de Nazca subductada. *Congreso Latinoamericano de Geología*, *5*, 587-606.

Jammes, S., & Huismans, R. S. (2012). Structural styles of mountain building : Controls of lithospheric rheologic stratification and extensional inheritance. *Journal of Geophysical Research: Solid Earth*, *117*(B10). https://doi.org/10.1029/2012JB009376

Jordan, T. E., & Allmendinger, R. W. (1986). The Sierras Pampeanas of Argentina : A modern analogue of Rocky Mountain foreland deformation. *American Journal of Science*, *286*(10), 737-764. https://doi.org/10.2475/AJS.286.10.737

Jordan, T. E., Allmendinger, R. W., Damanti, J. F., & Drake, R. E. (1993). Chronology of motion in a complete thrust belt : The Precordillera, 30-31°S, Andes Mountains. *Journal of Geology*, *101*(2), 135-156. https://doi.org/10.1086/648213

Jordan, T. E., Isacks, B. L., Ramos, V. A., & Allmendinger, R. W. (1983). Mountain building in the central Andes. *Episodes*, *1983*(3), 20-26. https://doi.org/10.18814/EPIIUGS/1983/V6I3/005

Jordan, T. E., Ramos, V. A. ,. Allmendinger, R. W. ,. &. Isacks, B. L. (1984). *Andean tectonics related to geometry of subducted Nazca plate : Discussion and reply : Reply*. *July*, 877-880. https://doi.org/10.1130/0016-7606(1984)95<877

Kay, S. M. (1991). Magma source variations for mid-late Tertiary magmatic rocks associated with a shallowing subduction zone and a thickening crust in the central Andes (28 to 33°S). *pecial Paper of the Geological Society of America*, *265*, 113-137. http://dx.doi.org/10.1130/SPE265-p113

Kay, S. M., & Abbruzzi, J. M. (1996). Magmatic evidence for Neogene lithospheric evolution of the central Andean « flat-slab » between 30°S and 32°S. *Tectonophysics*, *259*(1-3 SPEC. ISS.), 15-28. https://doi.org/10.1016/0040-1951(96)00032-7

Kay, S. M., Maksaev, V., Moscoso, R., Mpodozis, C., & Nasi, C. (1987). Probing the evolving Andean Lithosphere : Mid-Late Tertiary magmatism in Chile (29°–30°30’S) over the modern zone of subhorizontal subduction. *Journal of Geophysical Research: Solid Earth*, *92*(B7), 6173-6189. https://doi.org/10.1029/JB092iB07p06173

Kley, J. (1999). Geologic and geometric constraints on a kinematic model of the Bolivian orocline. *Journal of South American Earth Sciences*, *12*(2), 221-235. https://doi.org/10.1016/S0895-9811(99)00015-2

Kley, J., & Monaldi, C. R. (1998). Tectonic shortening and crustal thickness in the Central Andes : How good is the correlation-? *Geology*, *26*(8), 723-726. https://doi.org/10.1130/0091-7613(1998)026<0723:TSACTI>2.3.CO;2

Kley, J., & Monaldi, C. R. (2002). Tectonic inversion in the Santa Barbara System of the central Andean foreland thrust belt, northwestern Argentina. *Tectonics*, *21*(6), 11-1-11-18. https://doi.org/10.1029/2002TC902003

Kley, J., Monaldi, C. R., & Salfity, J. A. (1999). Along-strike segmentation of the Andean foreland : Causes and consequences. *Tectonophysics*, *301*(1-2), 75-94. https://doi.org/10.1016/S0040-1951(98)90223-2

Kley, J., & Monaldi, C. R. (2002). Tectonic inversion in the Santa Barbara System of the central Andean foreland thrust belt, northwestern Argentina. *Tectonics*, *21*(6), 1-18. https://doi.org/10.1029/2002tc902003

Kronbichler, M., Heister, T., & Bangerth, W. (2012). High accuracy mantle convection simulation through modern numerical methods. *Geophys J Int*, *191*(1), 12-29. https://doi.org/10.1111/j.1365-246x.2012.05609.x

Lallemand, S., Heuret, A., Faccenna, C., & Funiciello, F. (2008). Subduction dynamics as revealed by trench migration. *Tectonics*, *27*(3). https://doi.org/10.1029/2007TC002212

Lamb, S., & Davis, P. (2003). Cenozoic climate change as a possible cause for the rise of the Andes. *Nature*, *425*(6960), 792-797. https://doi.org/10.1038/NATURE02049

Liu, S., & Currie, C. A. (2016). Farallon plate dynamics prior to the Laramide orogeny : Numerical models of flat subduction. *Tectonophysics*, *666*, 33-47. https://doi.org/10.1016/J.TECTO.2015.10.010

Liu, S., Sobolev, S. V., Babeyko, A. Y., & Pons, M. (2022). Controls of the Foreland Deformation Pattern in the Orogen-Foreland Shortening System : Constraints From High-Resolution Geodynamic Models. *Tectonics*, *41*(2). https://doi.org/10.1029/2021TC007121

Lossada, A., Giambiagi, L., Hoke, G., AU, & Suriano, J. (2017). *Cenozoic Uplift and Exhumation of the Frontal Cordillera Between 30° and 35° S and the Influence of the Subduction Dynamics in the Flat Slab Subduction Context, South Central Andes*. https://doi.org/10.1007/978-3-319-67774-3_16

Marot, M., Monfret, T., Gerbault, M., Nolet, G., Ranalli, G., & Pardo, M. (2014). Flat versus normal subduction zones : A comparison based on 3-D regional traveltime tomography and petrological modelling of central Chile and western Argentina (29°–35°S). *Geophys J Int*, *199*(3), 1633-1654. https://doi.org/10.1093/gji/ggu355

Mackwell, S. J., Zimmerman, M. E., & Kohlstedt, D. L. (1998a). High-temperature deformation of dry diabase with application to tectonics on Venus. *Journal of Geophysical Research: Solid Earth*, *103*(1), 975-984. https://doi.org/10.1029/97JB02671

Mackwell, S. J., Zimmerman, M. E., & Kohlstedt, D. L. (1998b). High-temperature deformation of dry diabase with application to tectonics on Venus. *Journal of Geophysical Research: Solid Earth*, *103*(1), 975-984. https://doi.org/10.1029/97JB02671

Mahlburg Kay, S., & Mpodozis, C. (2002). Magmatism as a probe to the Neogene shallowing of the Nazca plate beneath the modern Chilean flat-slab. *Journal of South American Earth Sciences*, *15*(1), 39-57. https://doi.org/10.1016/S0895-9811(02)00005-6

Manceda, R., & Figueroa, D. (1995). *Inversion of the Mesozoic Neuquén rift in the Malargüe fold and thrust belt, Mendoza, Argentina*.

Mareschal, J.-C., & Jaupart, C. (2011). Energy Budget of the Earth. In H. K. Gupta (Éd.), *Encyclopedia of Solid Earth Geophysics* (p. 285-291). Springer Netherlands. https://doi.org/10.1007/978-90-481-8702-7_64

Martinod, J., Gérault, M., Husson, L., & Regard, V. (2020). Widening of the Andes : An interplay between subduction dynamics and crustal wedge tectonics. *Earth-Science Reviews*, *204*, 103170. https://doi.org/10.1016/j.earscirev.2020.103170

Martinod, J., Husson, L., Roperch, P., Guillaume, B., & Espurt, N. (2010). Horizontal subduction zones, convergence velocity and the building of the Andes. *Earth and Planetary Science Letters*, *299*(3-4), 299-309. https://doi.org/10.1016/j.epsl.2010.09.010

McGroder, M. F., Lease, R. O., & Pearson, D. M. (2015). Along-strike variation in structural styles and hydrocarbon occurrences, Subandean fold-and-thrust belt and inner foreland, Colombia to Argentina. *Memoir of the Geological Society of America*, *212*, 79-113. https://doi.org/10.1130/2015.1212(05)

Melnick, D., Charlet, F., Echtler, H. P., & De Batist, M. (2006). Incipient axial collapse of the Main Cordillera and strain partitioning gradient between the central and Patagonian Andes, Lago Laja, Chile. *Tectonics*, *25*(5). https://doi.org/10.1029/2005TC001918

Mescua, J. F., Giambiagi, L. B., Tassara, A., Gimenez, M., & Ramos, V. A. (2014). Influence of pre-Andean history over Cenozoic foreland deformation : Structural styles in the Malargüe fold-and-thrust belt at 35 S, Andes of Argentina. *Geosphere*, *10*(3), 585-609. https://doi.org/10.1130/GES00939.1

Mescua, J. F., Giambiagi, L., Barrionuevo, M., Tassara, A., Mardonez, D., Mazzitelli, M., & Lossada, A. (2016). Basement composition and basin geometry controls on upper-crustal deformation in the Southern Central Andes (30-36°S). *Geological Magazine*, *153*(5-6), 945-961. https://doi.org/10.1017/S0016756816000364

Molnar, P., & Tapponnier, P. (1975). Cenozoic Tectonics of Asia : Effects of a Continental Collision. *Science*, *189*(4201), 419-426. https://doi.org/10.1126/science.189.4201.419

Mon, R., & Salfity, J. (1995). Tectonic evolution of the Andes of northern Argentina. In *Petroleum Basins of South America* (Vol. 62). AAPG Special Volumes.

Mouthereau, F., Watts, A. B., & Burov, E. (2013). Structure of orogenic belts controlled by lithosphere age. *Nat Geosci*, *6*(9), 785-789. https://doi.org/10.1038/ngeo1902

Mpodozis, C., & Kay, S. M. (1990). Provincias magmáticas ácidas y evolución tectónica de Gondwana : Andes chilenos (28-31 S). *Andean Geology*, *17*(2), 153-180. http://dx.doi.org/10.5027/andgeoV17n2-a03

Muldashev, I. A., & Sobolev, S. V. (2020). What Controls Maximum Magnitudes of Giant Subduction Earthquakes? *Geochemistry, Geophysics, Geosystems*, *21*(9). https://doi.org/10.1029/2020GC009145

Murnaghan, F. D. (1944). The Compressibility of Media under Extreme Pressures. *Proceedings of the National Academy of Sciences*, *30*(9), 244-247. https://doi.org/10.1073/pnas.30.9.244

Neuharth, D., Brune, S., Glerum, A. C., Morley, C. K., Yuan, X., & Braun, J. (2021). *Flexural strike-slip basins*. https://eartharxiv.org/repository/view/2439/

Oncken, O., Hindle, D., Kley, J., Elger, K., Victor, P., & Schemmann, K. (2006). Deformation of the central Andean upper plate system—Facts, fiction, and constraints for plateau models. In *The Andes* (pp. 3-27). Springer, Berlin, Heidelberg.

Oncken, O., Boutelier, D., Dresen, G., & Schemmann, K. (2012). Strain accumulation controls failure of a plate boundary zone : Linking deformation of the Central Andes and lithosphere mechanics. *Geochemistry, Geophysics, Geosystems*, *13*(12). https://doi.org/10.1029/2012GC004280

Ortiz, G., Stevens Goddard, A. L., Fosdick, J. C., Alvarado, P., Carrapa, B., & Cristofolini, E. (2021). Fault reactivation in the Sierras Pampeanas resolved across Andean extensional and compressional regimes using thermochronologic modeling. *Journal of South American Earth Sciences*, *112*, 103533. https://doi.org/10.1016/j.jsames.2021.103533

Pearson, D. M., Kapp, P., DeCelles, P. G., Reiners, P. W., Gehrels, G. E., Ducea, M. N., & Pullen, A. (2013). Influence of pre-Andean crustal structure on Cenozoic thrust belt kinematics and shortening magnitude : Northwestern Argentina. *Geosphere*, *9*(6), 1766-1782. https://doi.org/10.1130/GES00923.1

Pesicek, J. D., Engdahl, E. R., Thurber, C. H., DeShon, H. R., & Lange, D. (2012). Mantle subducting slab structure in the region of the 2010 M8.8 Maule earthquake (30-40°S), Chile : Mantle subducting slab structure in Chile. *Geophysical Journal International*, *191*(1), 317-324. https://doi.org/10.1111/j.1365-246X.2012.05624.x

Pilger Jr, R. H. (1981). Plate reconstructions, aseismic ridges, and low-angle subduction beneath the Andes. *GSA Bulletin*, *92*(7), 448-456. https://doi.org/10.1130/0016-7606(1981)92<448:PRARAL>2.0.CO;2

Pons, M., Sobolev, S. V., Liu, S., & Neuharth, D. (2022). Hindered Trench Migration Due To Slab Steepening Controls the Formation of the Central Andes. *Journal of Geophysical Research: Solid Earth*, *127*(12), e2022JB025229. https://doi.org/10.1029/2022JB025229

Ramos, V. (2010). The Grenville-age basement of the Andes. *J S Am Earth Sci*, *29*(1), 77-91. https://doi.org/10.1016/j.jsames.2009.09.004

Ramos, V. A., Cristallini, E. O., & Pérez, D. J. (2002a). The Pampean flat-slab of the Central Andes. *Journal of South American Earth Sciences*, *15*(1), 59-78. https://doi.org/10.1016/s0895-9811(02)00006-8

Ramos, V. A., Cristallini, E. O., & Pérez, D. J. (2002b). The Pampean flat-slab of the Central Andes. *Journal of South American Earth Sciences*, *15*(1), 59-78. https://doi.org/10.1016/S0895-9811(02)00006-8

Ramos, V. A., & Folguera, A. (2009). Andean flat-slab subduction through time. *Geological Society Special Publication*, *327*, 31-54. https://doi.org/10.1144/SP327.3

Ramos, V. A., & Scientific, N. (2002). Flat-slab subduction in the Andes. *Journal of South American Earth Sciences*, *15*(1), 1-2. https://doi.org/10.1016/s0895-9811(02)00011-1

Ranalli, G. (1997). Rheology and deep tectonics. *Annals of Geophysics*, *40*(3), 3. https://doi.org/10.4401/ag-3893

Regard, V., Saillard, M., Martinod, J., Audin, L., Carretier, S., Pedoja, K., Riquelme, R., Paredes, P., & Hérail, G. (2010). Renewed uplift of the Central Andes Forearc revealed by coastal evolution during the Quaternary. *Earth and Planetary Science Letters*, *297*(1), 199-210. https://doi.org/10.1016/j.epsl.2010.06.020

Rodriguez Piceda, C., Scheck Wenderoth, M., Gomez Dacal, M. L., Bott, J., Prezzi, C. B., & Strecker, M. R. (2020). Lithospheric density structure of the southern Central Andes constrained by 3D data-integrative gravity modelling. *International Journal of Earth Sciences 2020 110:7*, *110*(7), 2333-2359. https://doi.org/10.1007/S00531-020-01962-1

Rodriguez Piceda, C., Scheck Wenderoth, M., Gomez Dacal, M. L., Bott, J., Prezzi, C. B., & Strecker, M. R. (2021). Lithospheric density structure of the southern Central Andes constrained by 3D data-integrative gravity modelling. *International Journal of Earth Sciences*, *110*(7), 2333-2359. https://doi.org/10.1007/S00531-020-01962-1

Rodriguez Piceda, C., Scheck-Wenderoth, M., Bott, J., Gomez Dacal, M. L., Cacace, M., Pons, M., Prezzi, C. B., & Strecker, M. R. (2022). Controls of the Lithospheric Thermal Field of an Ocean-Continent Subduction Zone : The Southern Central Andes. *Lithosphere*, *2022*(1), 2237272. https://doi.org/10.2113/2022/2237272

Rodriguez Piceda, C., Scheck-Wenderoth, M., Cacace, M., Bott, J., & Strecker, M. R. (2022). Long-Term Lithospheric Strength and Upper-Plate Seismicity in the Southern Central Andes, 29°–39°S. *Geochemistry, Geophysics, Geosystems*, *23*(3), 22. https://doi.org/10.1029/2021GC010171

Rose, I., Buffett, B., & Heister, T. (2017). Stability and accuracy of free surface time integration in viscous flows. *Physics of the Earth and Planetary Interiors*, *262*, 90-100. https://doi.org/10.1016/J.PEPI.2016.11.007

Rosenau, M., Melnick, D., & Echtler, H. (2006). Kinematic constraints on intra-arc shear and strain partitioning in the southern Andes between 38°S and 42°S latitude. *Tectonics*, *25*(4). https://doi.org/10.1029/2005TC001943

Scarfi, L., & Barbieri, G. (2019). New insights on the tectonic structure of the Southern Central Andes – Western Argentina – from seismic tomography. *Geology, Earth & Marine Sciences*, *1*(1). https://doi.org/10.31038/GEMS.2019113

Schaeffer, A., & Lebedev, S. (2013). Global shear speed structure of the upper mantle and transition zone. *Geophysical Journal International*, *194*(1), 417-449.

Sdrolias, M., & Müller, R. D. (2006). Controls on back-arc basin formation. *Geochemistry, Geophysics, Geosystems*, *7*(4). https://doi.org/10.1029/2005GC001090

Sippel, J., Meeßen, C., Cacace, M., Mechie, J., Fishwick, S., Heine, C., Scheck-Wenderoth, M., & Strecker, M. R. (2017). The Kenya rift revisited : Insights into lithospheric strength through data-driven 3-D gravity and thermal modelling. *Solid Earth*, *8*(1), 45-81. https://doi.org/10.5194/se-8-45-2017

Sobolev, S. V., & Babeyko, A. Y. (1994). Modeling of mineralogical composition, density and elastic wave velocities in anhydrous magmatic rocks. *Surveys in Geophysics*, *15*(5), 515-544. https://doi.org/10.1007/BF00690173

Sobolev, S. V., & Babeyko, A. Y. (2005). What drives orogeny in the Andes? *Geology*, *33*(8), 617-620. https://doi.org/10.1130/G21557.1

Sobolev, S. V., Babeyko, A. Y., Koulakov, I., & Oncken, O. (2006). Mechanism of the Andean Orogeny : Insight from Numerical Modeling. In *The Andes* (p. 513-535). Springer Berlin Heidelberg. https://doi.org/10.1007/978-3-540-48684-8_25

Stalder, N. F., Herman, F., Fellin, M. G., Coutand, I., Aguilar, G., Reiners, P. W., & Fox, M. (2020). The relationships between tectonics, climate and exhumation in the Central Andes (18–36°S) : Evidence from low-temperature thermochronology. *Earth-Science Reviews*, *210*, 103276. https://doi.org/10.1016/j.earscirev.2020.103276

Stüwe, K. (2007). *Geodynamics of the Lithosphere*. Springer-Verlag Berlin Heidelberg.

Tassara, A. (2005). Interaction between the Nazca and South American plates and formation of the Altiplano–Puna plateau : Review of a flexural analysis along the Andean margin (15°–34°S). *Andean Geodynamics:*, *399*(1), 39-57. https://doi.org/10.1016/j.tecto.2004.12.014

Tassara, A., & Yáñez, G. (2003). Relación entre el espesor elástico de la litosfera y la segmentación tectónica del margen andino (15-47°S). *Revista geológica de Chile*, *30*(2), 159-186. https://doi.org/10.4067/S0716-02082003000200002

Tesauro, M., Kaban, M. K., & Mooney, W. D. (2015). Variations of the lithospheric strength and elastic thickness in North America : Lithospheric Strength and Te variations. *Geochemistry, Geophysics, Geosystems*, *16*(7), 2197-2220. https://doi.org/10.1002/2015GC005937

Uliana, M. A., Arteaga, M. E., Legarreta, L., Cerdán, J. J., & Peroni, G. O. (1995). Inversion structures and hydrocarbon occurrence in Argentina. *Geological Society, London, Special Publications*, *88*(1), 211-233. https://doi.org/10.1144/GSL.SP.1995.088.01.13

Uyeda, S., & Kanamori, H. (1979). Back-arc opening and the mode of subduction. *Journal of Geophysical Research: Solid Earth*, *84*(B3), 1049-1061. https://doi.org/10.1029/JB084iB03p01049

van Keken, P. E., Wada, I., Sime, N., & Abers, G. A. (2019). Thermal Structure of the Forearc in Subduction Zones : A Comparison of Methodologies. *Geochemistry, Geophysics, Geosystems*, *20*(7), 3268-3288. https://doi.org/10.1029/2019GC008334

Vietor, T., & Echtler, H. (2006). Episodic Neogene Southward Growth of the Andean Subduction Orogen between 30°S and 40°S — Plate Motions, Mantle Flow, Climate, and Upper-Plate Structure. In O. Oncken, G. Chong, G. Franz, P. Giese, H.-J. Götze, V. A. Ramos, M. R. Strecker, & P. Wigger (Éds.), *The Andes* (p. 375-400). Springer Berlin Heidelberg. https://doi.org/10.1007/978-3-540-48684-8_18

Völker, D., Geersen, J., Contreras-Reyes, E., & Reichert, C. (2013). Sedimentary fill of the Chile Trench (32–46°S) : Volumetric distribution and causal factors. *Journal of the Geological Society*, *170*(5), 723-736. https://doi.org/10.1144/jgs2012-119

Wada, I., & Wang, K. (2009). Common depth of slab-mantle decoupling : Reconciling diversity and uniformity of subduction zones. *Geochemistry, Geophysics, Geosystems*, *10*(10). https://doi.org/10.1029/2009GC002570

Wagner, L. S., Beck, S., & Zandt, G. (2005). Upper mantle structure in the south central Chilean subduction zone (30° to 36°S). *Journal of Geophysical Research: Solid Earth*, *110*(B1). https://doi.org/10.1029/2004JB003238

Wimpenny, S. (2022). Weak, Seismogenic Faults Inherited From Mesozoic Rifts Control Mountain Building in the Andean Foreland. *Geochemistry, Geophysics, Geosystems*, *23*(3), e2021GC010270. https://doi.org/10.1029/2021GC010270

Xu, Y., Shankland, T. J., Linhardt, S., Rubie, D. C., Langenhorst, F., & Klasinski, K. (2004). Thermal diffusivity and conductivity of olivine, wadsleyite and ringwoodite to 20 GPa and 1373 K. *Physics of the Earth and Planetary Interiors*, *143-144*, 321-336. https://doi.org/10.1016/j.pepi.2004.03.005

Yáñez, G. A., Ranero, C. R., Von Huene, R., & Díaz, J. (2001). Magnetic anomaly interpretation across the southern central Andes (32°-34°S) : The role of the Juan Fernández Ridge in the late Tertiary evolution of the margin. *Journal of Geophysical Research: Solid Earth*, *106*(B4), 6325-6345. https://doi.org/10.1029/2000JB900337

Figure 1.

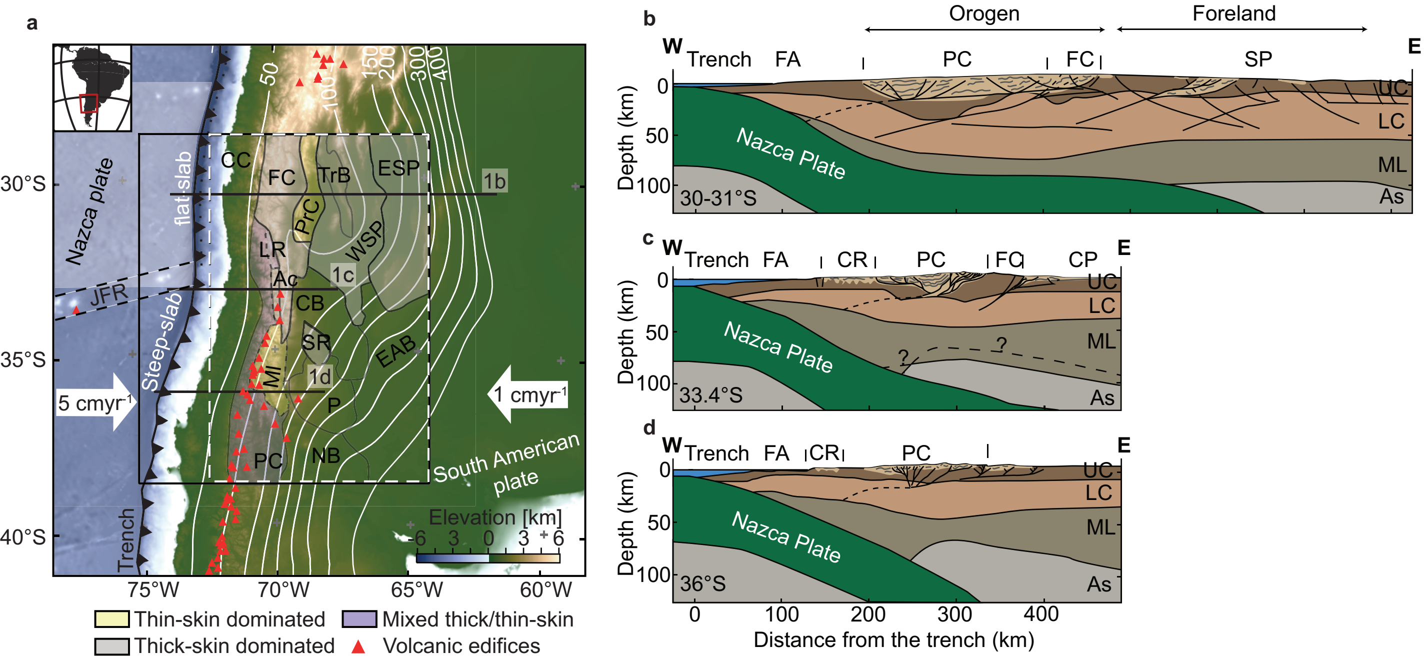
a
Nazca plate
flat-slab
Steep-slab
JFR
Trench
5 cmyr-1
1 cmyr-1
South American plate
CC
FC
TrB
ESP
PrC
LR
WSP
Ac
CB
SR
EAB
MI
P
PC
NB
1b
1c
1d
50
100
150
200
300
400
30°S
35°S
40°S
75°W
70°W
65°W
60°W
Elevation [km]
-6 3 0 3 6
Thin-skin dominated
Mixed thick/thin-skin
Thick-skin dominated
Volcanic edifices
b
Orogen
Foreland
W
E
Trench
FA
PC
FC
SP
UC
LC
ML
As
Nazca Plate
Depth (km)
0
50
100
30-31°S
c
Trench
FA
CR
PC
FC
CP
UC
LC
ML
As
Nazca Plate
33.4°S
d
Trench
FA
CR
PC
UC
LC
ML
As
Nazca Plate
36°S
0
100
200
300
400
Distance from the trench (km)

Figure 2.

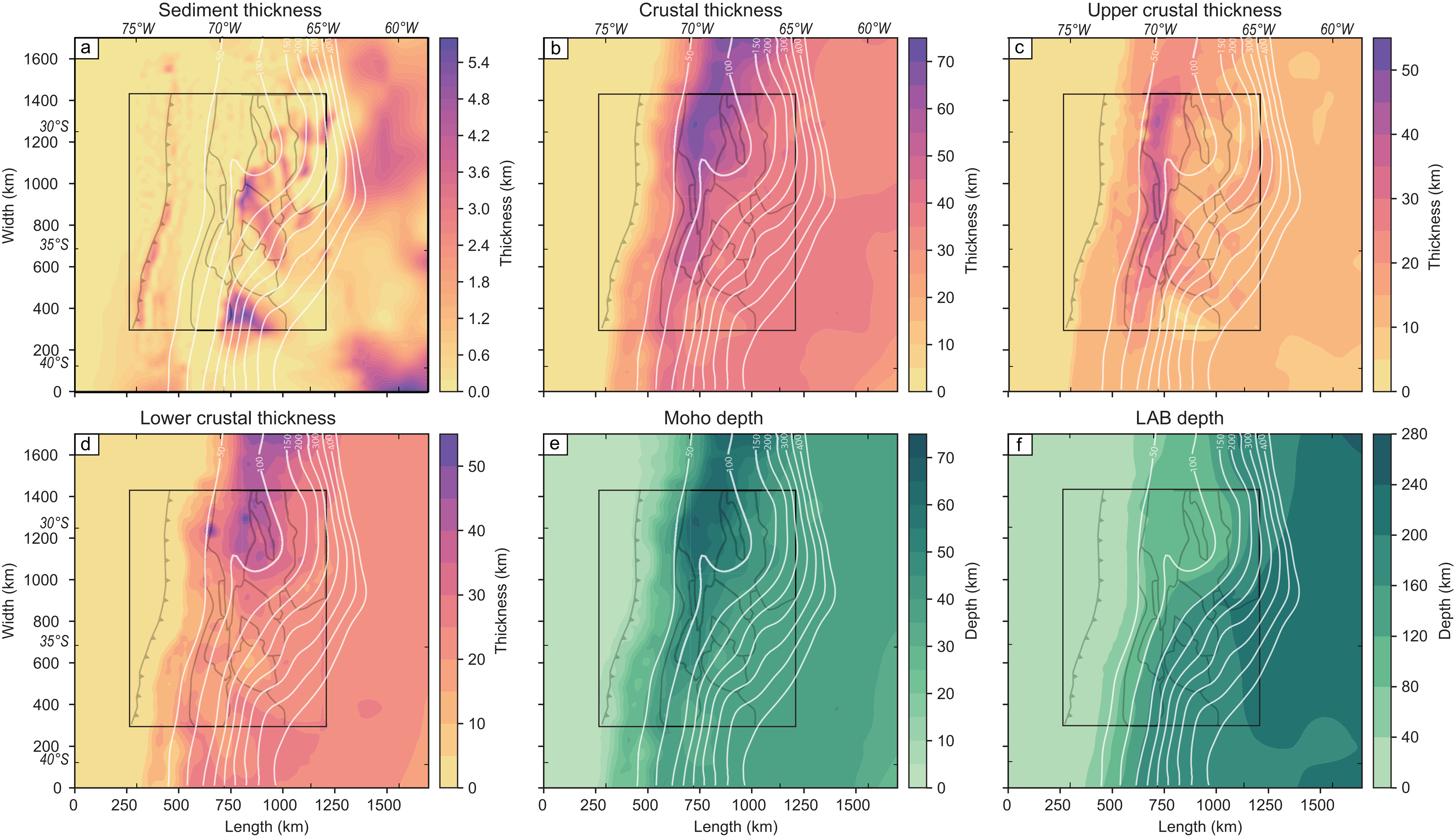
Sediment thickness
Crustal thickness
Upper crustal thickness
Lower crustal thickness
Moho depth
LAB depth
a
b
c
d
e
f
75°W
70°W
65°W
60°W
30°S
35°S
40°S
50
100
150
200
300
400
Width (km)
Length (km)
Thickness (km)
Depth (km)
0
250
500
750
1000
1250
1500
200
400
600
800
1200
1400
1600
0.0
0.6
1.2
1.8
2.4
3.0
3.6
4.2
4.8
5.4
10
20
30
40
50
60
70
40
80
120
160
200
240
280

Figure 3.

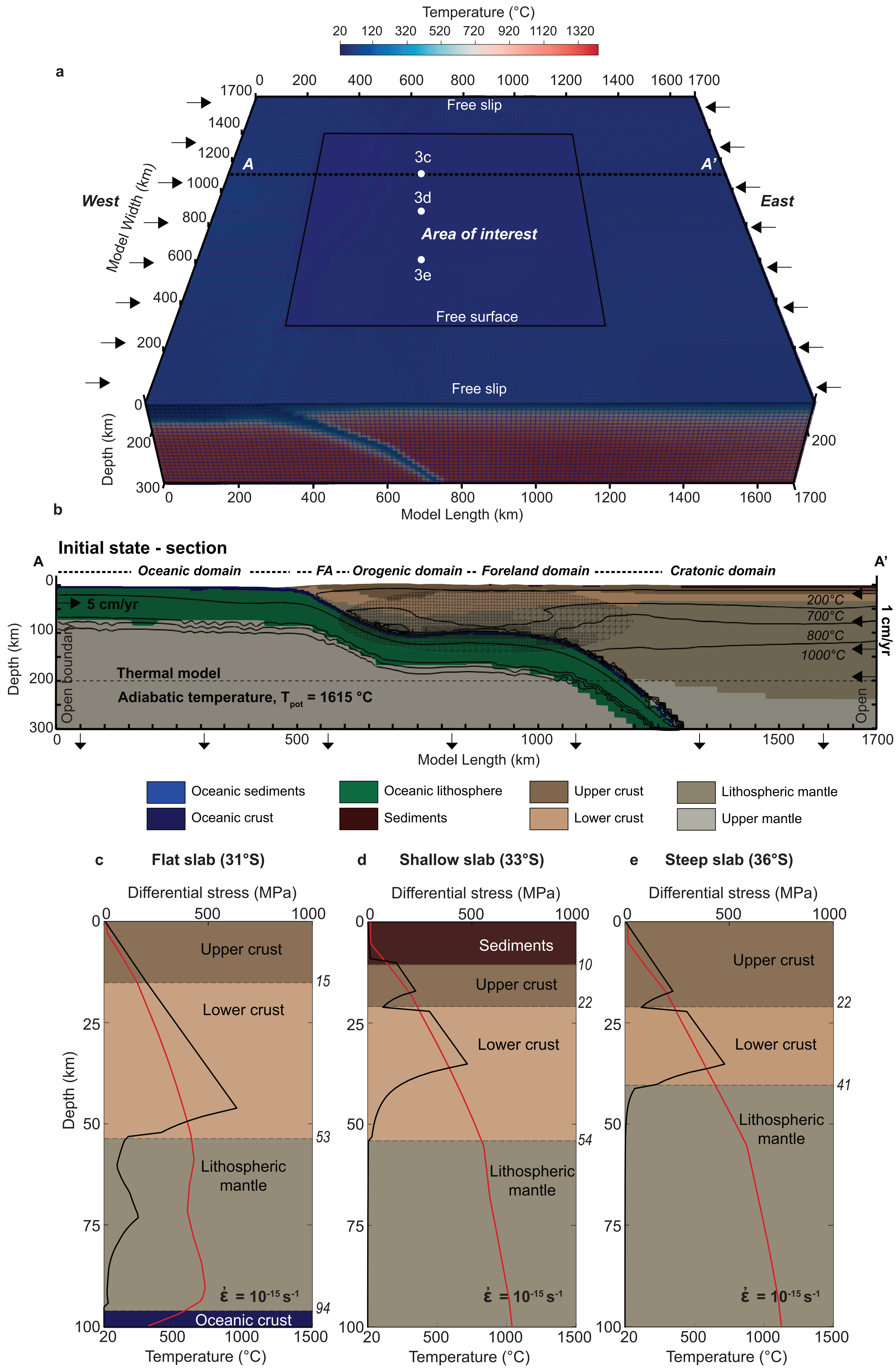

a
Temperature (°C)
20 120 320 520 720 920 1120 1320
Free slip
A
A'
3c
3d
3e
West
East
Area of interest
Free surface
Free slip
Model Width (km)
Depth (km)
Model Length (km)
b
Initial state - section
A
A'
Oceanic domain
FA
Orogenic domain
Foreland domain
Cratonic domain
5 cm/yr
1 cm/yr
200°C
700°C
800°C
1000°C
Thermal model
Adiabatic temperature, T_{pot} = 1615 °C
Open boundary
Open
Depth (km)
Model Length (km)
Oceanic sediments
Oceanic crust
Oceanic lithosphere
Sediments
Upper crust
Lower crust
Lithospheric mantle
Upper mantle
c Flat slab (31°S)
d Shallow slab (33°S)
e Steep slab (36°S)
Differential stress (MPa)
Depth (km)
Temperature (°C)
Upper crust
Lower crust
Lithospheric mantle
Oceanic crust
Sediments
15
53
94
10
22
54
41
$\dot{\varepsilon}$ = 10^{-15} s^{-1}

Figure 4.

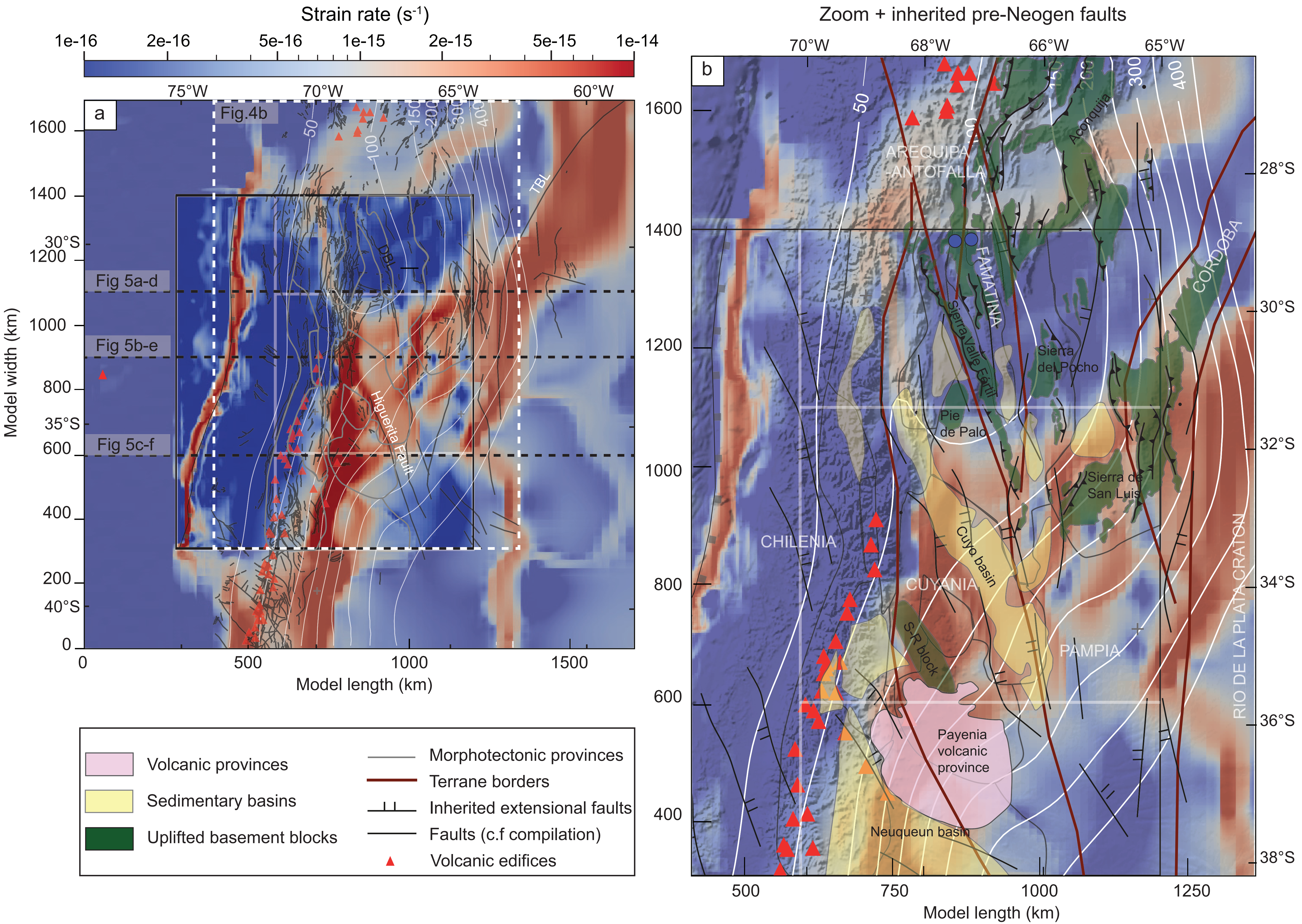

Strain rate (s-1)
1e-16
2e-16
5e-16
1e-15
2e-15
5e-15
1e-14
a
Fig.4b
Fig 5a-d
Fig 5b-e
Fig 5c-f
75°W
70°W
65°W
60°W
30°S
35°S
40°S
TBL
DBL
Higuerita Fault
Model width (km)
Model length (km)
Volcanic provinces
Sedimentary basins
Uplifted basement blocks
Morphotectonic provinces
Terrane borders
Inherited extensional faults
Faults (c.f compilation)
Volcanic edifices
Zoom + inherited pre-Neogen faults
b
70°W
68°W
66°W
65°W
28°S
30°S
32°S
34°S
36°S
38°S
AREQUIPA -ANTOFALLA
FAMATINA
Aconquija
CORDOBA
Sierra Valle Fértil
Sierra del Pocho
Pie de Palo
Sierra de San Luis
CHILENIA
Cuyo basin
CUYANIA
S-R block
PAMPIA
RIO DE LA PLATA CRATON
Payenia volcanic province
Neuqueun basin
Model length (km)

Figure 5.

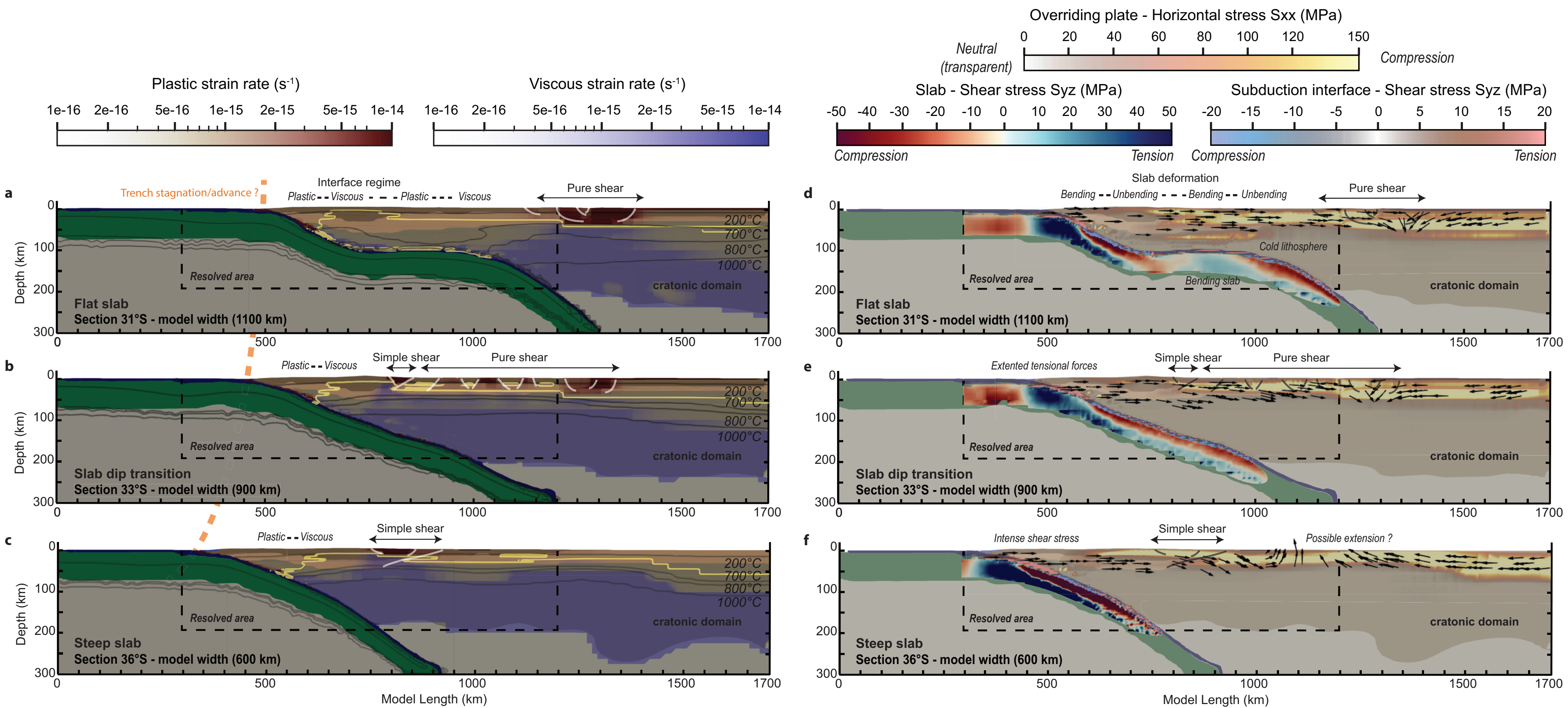

Overriding plate - Horizontal stress Sxx (MPa)
Neutral (transparent)
Compression
Plastic strain rate (s-1)
Viscous strain rate (s-1)
Slab - Shear stress Syz (MPa)
Subduction interface - Shear stress Syz (MPa)
Compression
Tension
Compression
Tension
Trench stagnation/advance ?
Interface regime
Plastic - - Viscous - - Plastic - - Viscous
Pure shear
Depth (km)
Resolved area
cratonic domain
Flat slab
Section 31°S - model width (1100 km)
Simple shear
Slab dip transition
Section 33°S - model width (900 km)
Plastic - - Viscous
Steep slab
Section 36°S - model width (600 km)
Model Length (km)
Slab deformation
Bending - - Unbending - - Bending - - Unbending
Cold lithosphere
Bending slab
Extented tensional forces
Intense shear stress
Possible extension ?

Figure 6.

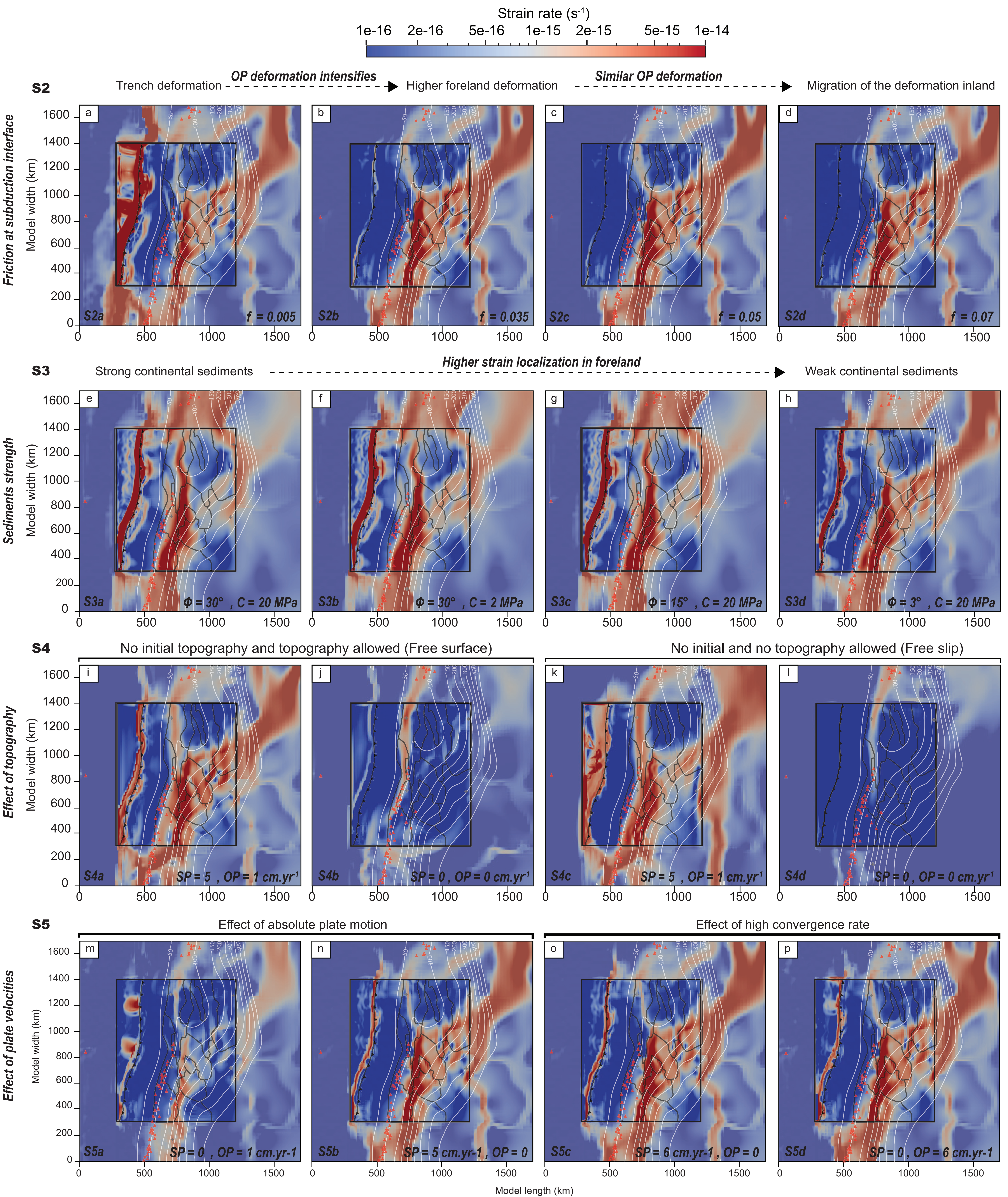

Strain rate (s-1)
1e-16 2e-16 5e-16 1e-15 2e-15 5e-15 1e-14
S2
Trench deformation
OP deformation intensifies
Higher foreland deformation
Similar OP deformation
Migration of the deformation inland
Friction at subduction interface
Model width (km)
S2a f = 0.005
S2b f = 0.035
S2c f = 0.05
S2d f = 0.07
S3
Strong continental sediments
Higher strain localization in foreland
Weak continental sediments
Sediments strength
S3a Φ = 30° , C = 20 MPa
S3b Φ = 30° , C = 2 MPa
S3c Φ = 15° , C = 20 MPa
S3d Φ = 3° , C = 20 MPa
S4
No initial topography and topography allowed (Free surface)
No initial and no topography allowed (Free slip)
Effect of topography
S4a SP = 5 , OP = 1 cm.yr-1
S4b SP = 0 , OP = 0 cm.yr-1
S4c SP = 5 , OP = 1 cm.yr-1
S4d SP = 0 , OP = 0 cm.yr-1
S5
Effect of absolute plate motion
Effect of high convergence rate
Effect of plate velocities
S5a SP = 0 , OP = 1 cm.yr-1
S5b SP = 5 cm.yr-1 , OP = 0
S5c SP = 6 cm.yr-1 , OP = 0
S5d SP = 0 , OP = 6 cm.yr-1
Model length (km)

Figure 7.

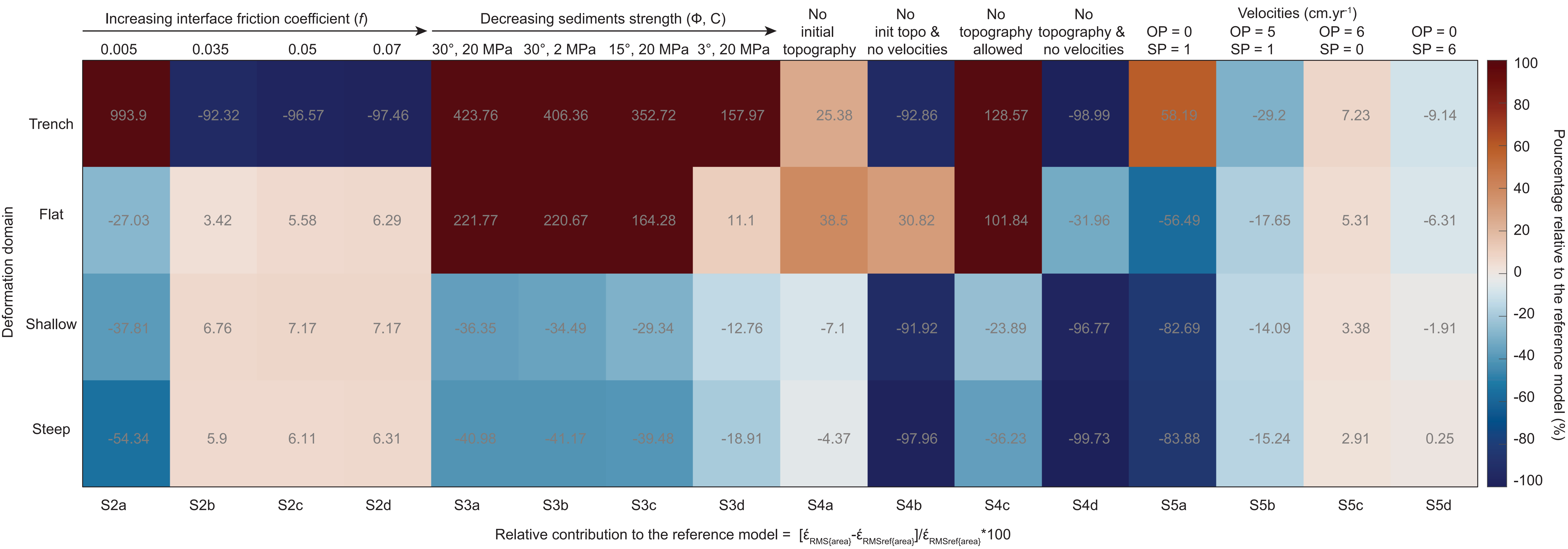
Increasing interface friction coefficient (f)
Decreasing sediments strength (Φ, C)
0.005
0.035
0.05
0.07
30°, 20 MPa
30°, 2 MPa
15°, 20 MPa
3°, 20 MPa
No initial topography
No init topo & no velocities
No topography allowed
No topography & no velocities
Velocities (cm.yr-1)
OP = 0 SP = 1
OP = 5 SP = 1
OP = 6 SP = 0
OP = 0 SP = 6
Deformation domain
Trench
993.9 -92.32 -96.57 -97.46 423.76 406.36 352.72 157.97 25.38 -92.86 128.57 -98.99 58.19 -29.2 7.23 -9.14
Flat
-27.03 3.42 5.58 6.29 221.77 220.67 164.28 11.1 38.5 30.82 101.84 -31.96 -56.49 -17.65 5.31 -6.31
Shallow
-37.81 6.76 7.17 7.17 -36.35 -34.49 -29.34 -12.76 -7.1 -91.92 -23.89 -96.77 -82.69 -14.09 3.38 -1.91
Steep
-54.34 5.9 6.11 6.31 -40.98 -41.17 -39.48 -18.91 -4.37 -97.96 -36.23 -99.73 -83.88 -15.24 2.91 0.25
S2a S2b S2c S2d S3a S3b S3c S3d S4a S4b S4c S4d S5a S5b S5c S5d
100 80 60 40 20 0 -20 -40 -60 -80 -100
Pourcentage relative to the reference model (%)
Relative contribution to the reference model = [έRMS{area}-έRMSref{area}]/έRMSref{area}*100

Figure 8.

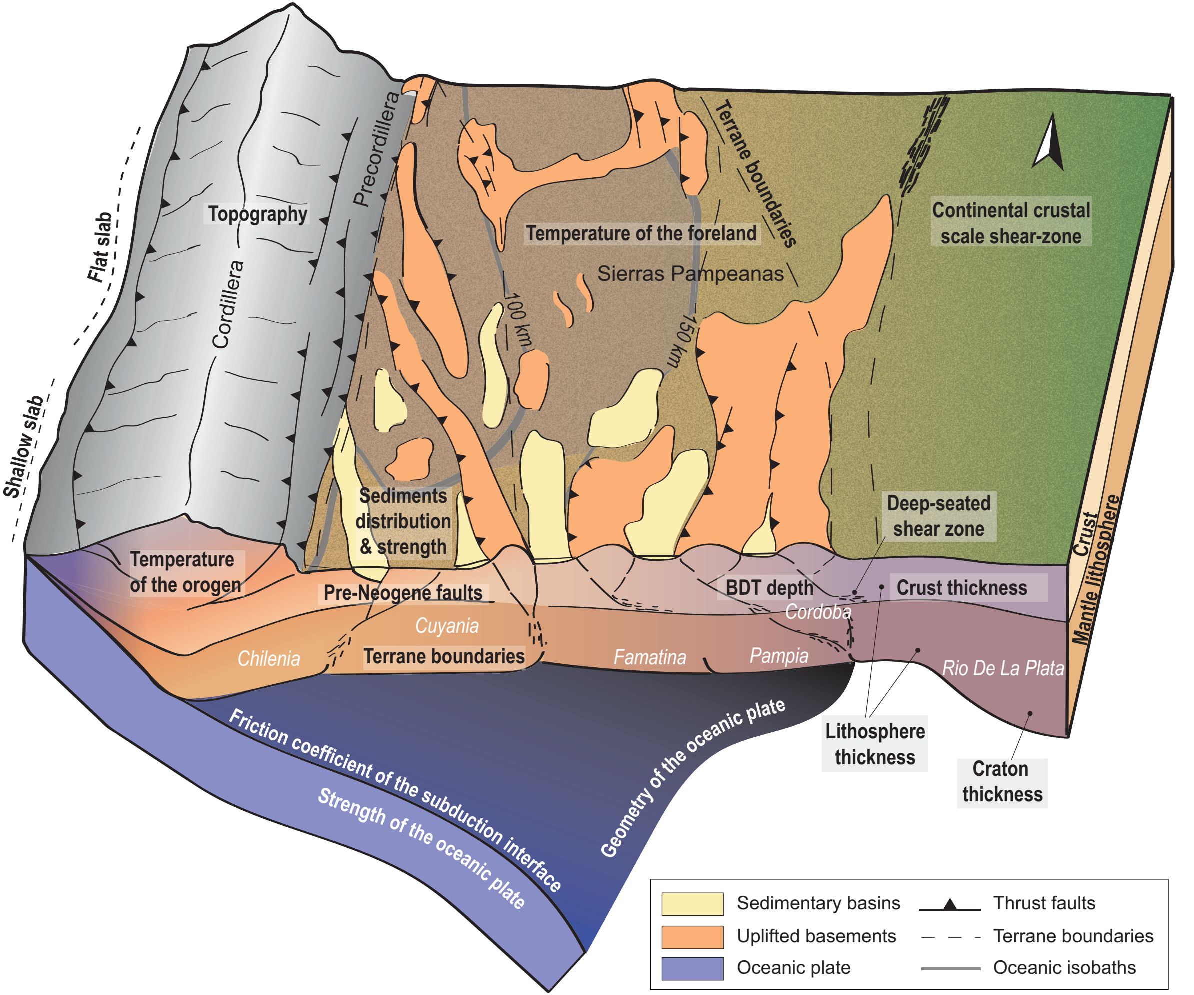
Flat slab
Shallow slab
Topography
Cordillera
Precordillera
Temperature of the foreland
Sierras Pampeanas
Terrane boundaries
Continental crustal scale shear-zone
100 km
150 km
Sediments distribution & strength
Deep-seated shear zone
Temperature of the orogen
Pre-Neogene faults
BDT depth
Crust thickness
Cordoba
Cuyania
Chilenia
Terrane boundaries
Famatina
Pampia
Rio De La Plata
Crust
Mantle lithosphere
Lithosphere thickness
Craton thickness
Friction coefficient of the subduction interface
Strength of the oceanic plate
Geometry of the oceanic plate
Sedimentary basins
Uplifted basements
Oceanic plate
Thrust faults
Terrane boundaries
Oceanic isobaths

Figure 9.

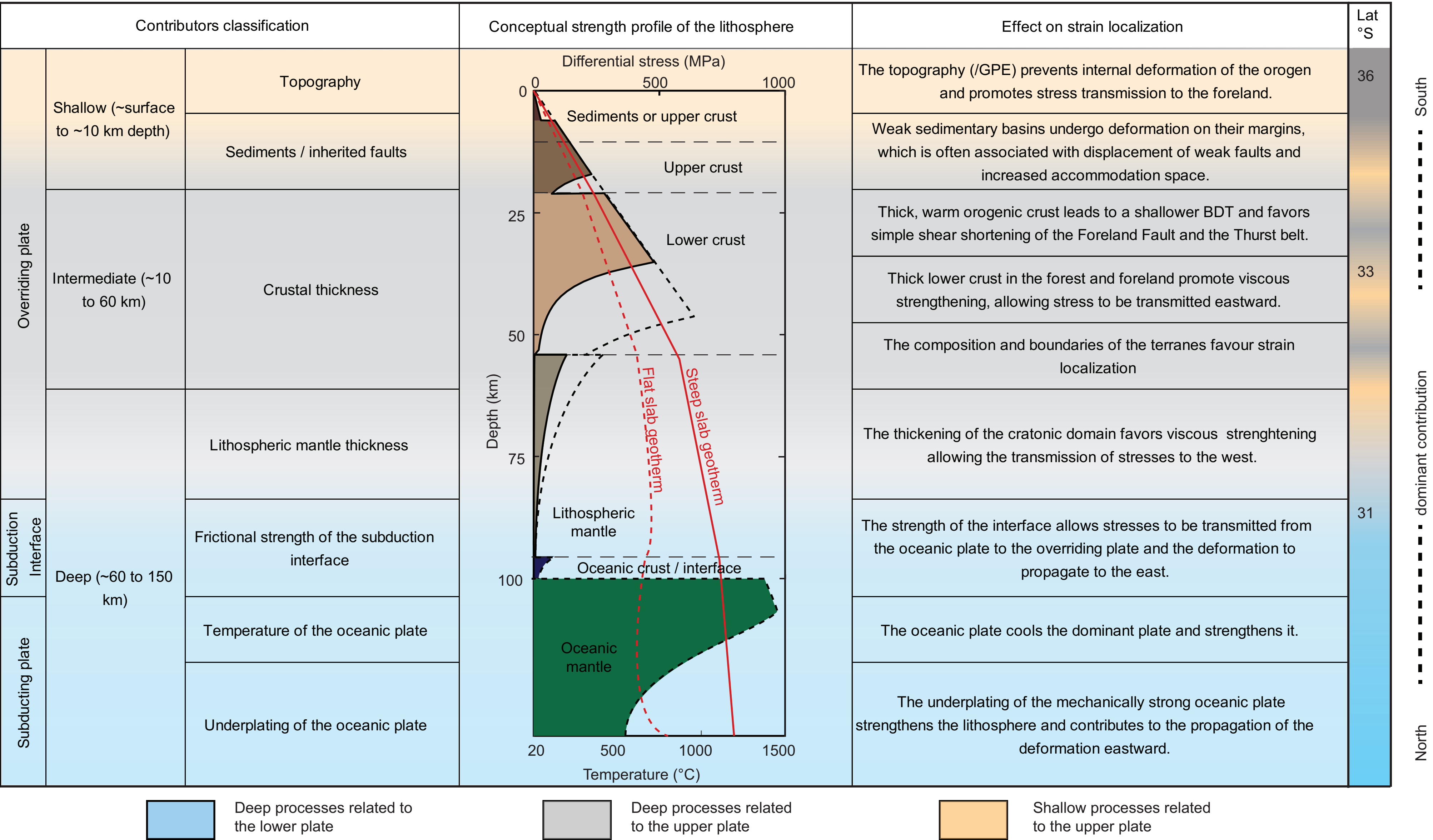

Contributors classification
Conceptual strength profile of the lithosphere
Effect on strain localization
Lat °S
Overriding plate
Subduction Interface
Subducting plate
Shallow (~surface to ~10 km depth)
Intermediate (~10 to 60 km)
Deep (~60 to 150 km)
Topography
Sediments / inherited faults
Crustal thickness
Lithospheric mantle thickness
Frictional strength of the subduction interface
Temperature of the oceanic plate
Underplating of the oceanic plate
Differential stress (MPa)
0
500
1000
Depth (km)
0
25
50
75
100
Sediments or upper crust
Upper crust
Lower crust
Lithospheric mantle
Oceanic crust / interface
Oceanic mantle
Flat slab geotherm
Steep slab geotherm
20
500
1000
1500
Temperature (°C)
The topography (/GPE) prevents internal deformation of the orogen and promotes stress transmission to the foreland.
Weak sedimentary basins undergo deformation on their margins, which is often associated with displacement of weak faults and increased accommodation space.
Thick, warm orogenic crust leads to a shallower BDT and favors simple shear shortening of the Foreland Fault and the Thurst belt.
Thick lower crust in the forest and foreland promote viscous strengthening, allowing stress to be transmitted eastward.
The composition and boundaries of the terranes favour strain localization
The thickening of the cratonic domain favors viscous strenghtening allowing the transmission of stresses to the west.
The strength of the interface allows stresses to be transmitted from the oceanic plate to the overriding plate and the deformation to propagate to the east.
The oceanic plate cools the dominant plate and strengthens it.
The underplating of the mechanically strong oceanic plate strengthens the lithosphere and contributes to the propagation of the deformation eastward.
36
33
31
South
dominant contribution
North
Deep processes related to the lower plate
Deep processes related to the upper plate
Shallow processes related to the upper plate

Localization of deformation in a non-collisional subduction orogen: the roles of dip geometry and plate strength on the evolution of the broken Andean foreland, Sierras Pampeanas, Argentina

Michaël Pons*,** (1,2), Constanza Rodriguez Piceda* (1,2,3), Stephan V. Sobolev (1.2), Magdalena Scheck-Wenderoth (1,4), Manfred R. Strecker (1)

(1) Universität Potsdam, Institut für Geowissenschaften, Germany, (2) Helmholtz-Zentrum Potsdam GFZ - Deutsches GeoForschungsZentrum, Germany (3) Plymouth University, School of Geography Earth and Environmental Sciences, United Kingdom (4) RWTH Aachen University, Aachen, Germany

these authors contributed equally to this work

*** Corresponding author: Michaël Pons (ponsm@gfz-potsdam.com)*

Abstract

The non-collisional subduction margin of South America is characterized by different geometries of the subduction zone and upper-plate tectono-magmatic provinces. The localization of deformation in the southern Central Andes (29°S–39°S) has been attributed to numerous factors that combine the properties of the subducting oceanic Nazca plate and the continental South American plate. In this study, the present-day configuration of the subducting oceanic plate and the continental upper plate were integrated in a data-driven geodynamic workflow to assess their role in determining strain localization within the upper plate of the flat slab and its southward transition to a steeper segment. The model predicts two fundamental processes that drive deformation in the Andean orogen and its foreland: eastward propagation of deformation in the flat-slab segment by a combined bulldozing mechanism and pure-shear shortening that affects the broken foreland and simple-shear shortening in the fold-and-thrust belt of the orogen above the steep slab segment. The transition between the steep and subhorizontal subduction segments is characterized by a 370-km-wide area of diffuse shear, where deformation transitions from pure to simple shear, resembling the transition from thick to thin-skinned foreland deformation in the southern Sierras Pampeanas. This pattern is controlled by the change in dip geometry of the Nazca plate and the presence of mechanically weak sedimentary basins and inherited faults.

Plain language summary

The deformation in the Sierras Pampeanas in the foreland of the southern Central Andes involves sedimentary cover rocks and the underlying crust. The mechanisms driving this style of deformation are debated between two schools of thought, with one group proposing that the subhorizontal subduction of the oceanic

Nazca Plate beneath the continent (also known as the flat-slab area) allows stresses to be propagated away from the oceanic trench into the Sierras Pampeanas, far away from the oceanic trench. Conversely, another group proposes that shear zones and faults in the South American continental crust and lithosphere that are inherited from previous tectonic regimes contribute to weaken the crust, and deformation and uplift of basement blocks follow closely through the reactivation of pre-existing structures such as terrane boundaries or extensional faults. These discontinuities would be responsible for the localization and style of deformation in the foreland. In this study, we numerically simulate the present kinematic and thermomechanical conditions of the Sierras Pampeanas to deduce the factors controlling deformation.

1. Introduction

Flat subduction occurs at 10% of presently active convergent margins (Gutscher et al., 2000) and fundamentally influences the tectono-magmatic evolution of tectonically active orogens; similar configurations have repeatedly existed in the geological past as well (Dickinson & Snyder, 1978; Jordan et al., 1983; Jordan & Allmendinger, 1986; Haines et al., 2001; Mahlburg Kay & Mpodozis, 2002) highlighting the importance of this geodynamic process in governing the distribution of seismicity, volcanism and orogenic growth. The western continental margin of South America hosts the Cenozoic Andes, the type example of a non-collisional Cenozoic mountain belt. The more than 6000-km-long Andes include the Altiplano-Puna Plateau, the second largest orogenic plateau on Earth; segments without a volcanic arc; thick- and thin-skinned thrust belts, whose deformation and uplift have been linked with the characteristics of the subducting Nazca Plate; and inherited, crustal-scale heterogeneities of the upper plate (Jordan et al., 1983). In South America, the Nazca and the Pampean flat slabs are thought to be associated with the subduction of bathymetric anomalies of the Nazca and Juan-Fernandez Ridge (JFR), respectively (Figure 1; Kley et al., 1999; Gutscher et al., 2000; Yáñez et al., 2001; Bello-González et al., 2018). Due to the oblique subduction and form of these anomalies, it has been suggested that the Pampean flat slab in the southern Central Andes (SCA) has migrated from ~20°S lat to its present-day position at ~32°S lat within the last 35 Ma, accompanied by an increase in the magnitude of shortening in the Central Andes (Ramos et al., 2002b; Oncken, 2006; Oncken et al., 2012; Pilger, 1981). Therefore, examining the interaction between the subducting oceanic plate and the continental upper plate in light of inherited heterogeneities and different subduction geometries is vital for our understanding of the different factors that influence strain localization in a convergent-margin setting. In this study, we explore the role of different shortening contributors in the Southern Central Andes (SCA, ~27°S–40°S) by integrating the previously constrained structural and thermal configurations of the plates (Rodriguez Piceda et al., 2021; 2022). According to these configurations the flat slab domain also has a spatial correlation with a portion of the upper plate that has a thick mafic lower crustal unit. This region of the upper plate therefore is relatively colder and rheologically stronger than other parts of the upper plate (Rodriguez

Piceda et al., 2022a,b). Above the flat-slab segment, deformation extends across an a really extensive broken foreland and localizes at the border of the reverse-faulted, thick-skinned Sierras Pampeanas (Ramos et al., 2002b). This style of deformation contrasts with a thin-skinned deformation style in fold-and-thrust belts (FTB), where the sedimentary cover rocks of the foreland sectors are involved in the deformation (Isacks et al., 1982; Jordan, 1984; Jordan & Allmendinger, 1986; Kay & Abbruzzi, 1996; Ramos et al., 2002b). The SCA foreland is characterized by a transition from dominantly thick-skinned (~27°S–33°S) to thin-skinned deformation (>~36°S, Manceda & Figueroa, 1995; Giambiagi et al., 2012; Fuentes, 2016). Between ~33°S and 36°S, both styles of deformation occur together. The eastward propagation and localization of deformation away from the trench through time can be explained by two main mechanisms: The first one involves a bulldozing process of the flat slab directed at the keel of the continental lithosphere (e.g., Jordan, 1984; Ramos & Folguera, 2009; Horton, 2018; Gutscher, 2018), where shear stresses are transmitted from the subduction interface at the trench to the eastern edge of the flat-slab segment. The second mechanism involves the compressional reactivation of steeply dipping crustal faults inherited from previous tectonic regimes (Figure 1d, Mon & Salfity, 1995; Kley & Monaldi, 1998; Cristallini & Ramos, 2000; Mescua et al., 2014; Giambiagi et al., 2014; Lossada et al., 2017)). By investigating the relative importance of the key contributors to strain localization, we discuss the viability of each mechanism in the SCA.

We distinguish between shallow and deep-seated contributors that affect the deformation of the crust or the entire lithosphere, respectively. At the surface, topography and the strength of the sedimentary rocks and their distribution is primarily a function of the formation of individual sedimentary basins that developed during Mesozoic extensional processes; the normal faults that once bounded these sedimentary basins were subsequently reactivated during Cenozoic Andean compression (Mpodozis & Kay, 1990; Uliana et al., 1995; Kley, 1999; 2002; Hongn et al., 2007; Del Papa et al., 2013; Fennell et al., 2019). Low frictional strength of unconsolidated sediments or poorly lithified sedimentary rocks may favor strain localization and thin-skinned deformation (Allmendinger, 1997; Allmendinger & Gubbels, 1996; Kley, 1999; Babeyko & Sobolev, 2005; Liu et al., 2022). Therefore, by including these sedimentary units in our model, we examined the role of crustal-scale heterogeneities. At greater depths, strain localization can be affected by lithospheric-scale heterogeneities, which can be classified as inherited discrete discontinuities, such as suture zones that developed during the amalgamation of Paleozoic terranes (e.g., Ramos, 2010). Alternatively, they may constitute volumetric discontinuities associated with inherited variations in the composition and/or thickness of the layers of the continental lithosphere (i.e., crystalline crust and lithospheric mantle), which reflect the tectono-magmatic evolution of different sectors within the orogen and its foreland (Ibarra et al., 2018, 2019; Liu et al., 2022; Rodriguez Piceda et al., 2021). Overall, structural and geometric parameters may influence lithospheric strength and the localization of deformation (Horton et al., 2022, Ramos et al., 2002, 2010, GIambiagi et al., 2022, Barrionuevo et al, 2021).

Using data-driven geodynamic modelling we developed a numerical modeling workflow that integrated data-driven three-dimensional structural, density, and thermal models (Rodriguez Piceda et al., 2021; 2022) into a geodynamic model to simulate shortening in the lithosphere of the SCA. Ultimately, our analysis sheds new light on the long-standing debate on the role and degree of influence of flat-slab geometry and inherited crustal-scale heterogeneities on deformation styles in orogenic forelands (Ramos et al., , 2002; Ramos & Folguera, 2009; Horton, 2016; Lossada et al., 2017).

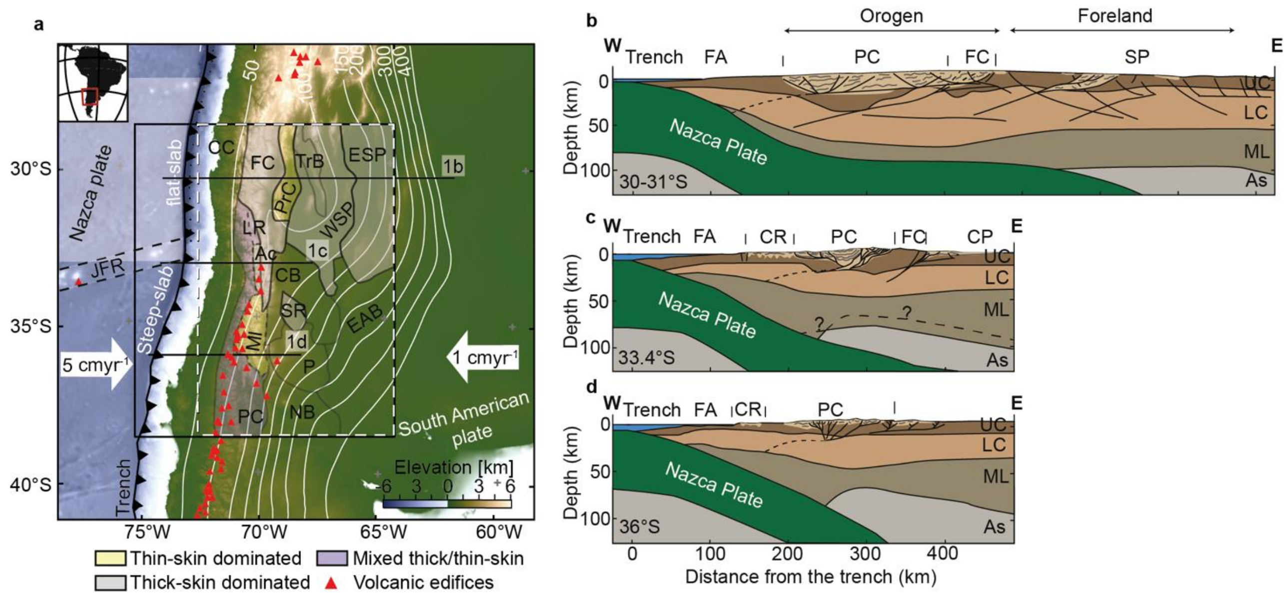

Figure 1 Structural cross sections and map of the Southern Central Andes. **a** topography and bathymetry of the model area based on ETOPO1 global relief model (Amante & Eakins, 2009), indicating the higher modelled resolved area (black rectangle) and the borders of the morphotectonic provinces (modified from Rodriguez Piceda et al., 2021) color-coded by the dominant style of deformation. The white-dashed rectangle outlines the extent of the gravity-constrained structural model (Rodriguez Piceda et al., 2021). Red triangles depict Cenozoic volcanic edifices. Depth contours of the top slab (Hayes et al., 2018) are shown in white lines. Dashed black lines in the oceanic domain delimit the Juan Fernandez Ridge (JFR). Oceanic and continental plate velocities are indicated by white arrows (Sdrolias & Müller, 2006; Becker et al., 2015). Abbreviations of main morphotectonic provinces: CB: Cuyo basin, CC: Coastal Cordillera, CP: Cerrilladas Pedemontanas, ESP: Eastern Sierras Pampeanas, NB: Neuquén basin; P: Payenia, PC: Principal Cordillera (LR= La Ramada fold-thrust belt, Ac: Aconcagua fold-thrust belt, Ml: Malargüe fold-thust belt), FC: Frontal Cordillera, FA: forearc, PrC: Precordillera, SR: San Rafael Block, TrB: Triassic basins, WSP: Western Sierras Pampeanas, EAB: Extra-Andean basins.. **b** Transect between 30-31°S (modified from Ramos et al., 2002b; Gans et al., 2011; Lossada et al., 2017; Stalder et al., 2020) **c** Transect at 33.4°S (modified from Barrionuevo

et al., 2021). **c** Transect at 36°S (modified from Barrionuevo et al., 2021). Abbreviations of lithospheric and asthenospheric units: UC: upper crust, LC: lower crust, ML: mantle listosphere, Ast: asthenosphere. Light-brown colored area indicates crustal regions with pronounced deformation. Slab dip based on CRUST 2.0 (Hayes et al., 2018).

2. Methods

2.1 Governing equations

We used the finite element code ASPECT (Advanced Solver for Problems in Earth's ConvecTion, version 2.3.0-pre, Kronbichler et al., 2012; Rose et al., 2017; Heister et al., 2017; Bangerth et al., 2021) to simulate brittle and ductile deformation. This code solves for conservation of the momentum (eq. 1), mass (eq. 2) and energy (eq. 3), together with the advection and reaction equations (eqs. 4-5).

$$-\nabla \cdot (2\eta\dot{\varepsilon}) + \nabla p = \rho g \,, \tag{2}$$

$$\nabla \cdot \boldsymbol{u} = 0 \,, \tag{2}$$

$$\varrho C p \left(\frac{\partial T}{\partial t} + \boldsymbol{u} \cdot \nabla T\right) - \nabla \cdot k \nabla T = \varrho H + (2\eta\dot{\varepsilon}) : \dot{\varepsilon} - \alpha T \boldsymbol{u} \cdot g \,, \tag{3}$$

$$\frac{\partial ci}{\partial t} + \boldsymbol{u} \cdot \nabla ci = qi \,, \tag{4}$$

Where $\dot{\varepsilon} = \frac{1}{2}.(\nabla \boldsymbol{u} + (\nabla \boldsymbol{u})^T$, is the deviatoric strain rate tensor, $u = u(\vec{x}, t), p = p(\vec{x}, t)$ and $T = T(\vec{x}, t)$ are the velocity, pressure and thermal fields, respectively. Cp is the heat capacity, ρ and ϱ are the density and the reference density (see eq. 5), k is the thermal conductivity, α is the thermal expansivity, η is the viscosity, t is time, ci is the composition, and qi is the reaction rate. The energy equation (eq. 3) includes shear heating and adiabatic heating, while the contribution of radiogenic heating to the temperatures is already included in the initial thermal condition.

To simulate realistic densities, we used the equation of state of Murnaghan (1944, eq. 5) which takes into account pressure, although the latter is neglected in the mass-conservation conversion equation (eq. 2). This assumption can be considered as an acceptable approximation since in subduction models compressibility is considered to have a negligible effect (Fraters, 2015).

$$\rho f = \rho ref i \left(1 + \left(P - \left(\frac{\alpha i}{\beta i}\right)(T - Tref)\right) ki\beta i\right)^{\frac{1}{ki}} \,, \tag{5}$$

ρf and $\rho refi$ are the final and reference density for each composition at reference temperature (Tref = 293 K) and surface pressures. αi is the thermal expansivity, βi is the isothermal compressibility and ki is the isothermal bulk-modulus pressure derivative.

The dominant mechanism of deformation depends on the yield stress, which is defined as the maximum differential stress that a rock is able to withstand without experiencing permanent deformation (Goetze & Evans, 1979). Viscous (ductile) deformation is simulated by harmonic averaging of dislocation and diffusion-creep mechanisms (eq. 6, Glerum et al., 2018):

$$\eta_{\mathrm{diff|disl}} = 0.5\, A_{\mathrm{diff|disl}}^{\left(-\frac{1}{\mathrm{n}}\right)}\, d^{m} \dot{\varepsilon}_{\mathrm{e}}^{\frac{1.-\mathrm{n}}{\mathrm{n}}}\ \exp\left(\frac{Q_{\mathrm{diff|disl}} + P.V_{\mathrm{diff|disl}}}{nRT}\right), \quad (6)$$

where A is the prefactor rescaled from uniaxial experiments, n is the stress exponent, d and m are the grain size and grain size exponent, $\dot{\varepsilon}_e$ is the square root of deviatoric strain rate, Q is the energy of activation, V is the volume of activation, P the pressure, R the gas constant, and T the temperature. Dislocation creep is grain-size independent, therefore the term d^m is removed from eq. (6) for n_{disl}. In turn, plastic (brittle) deformation is described by the Drucker-Prager criterion (eq. 7):

$$in\ 3D:\ \sigma y = \frac{6C.cos\Phi}{\sqrt{3(3-sin\Phi)}} + \frac{6P.sin\Phi}{\sqrt{3(3-sin\Phi)}}, \quad (7)$$

where C, P and F hold for the cohesion, the pressure and the internal friction angle (radians), respectively. Additionally, we included a linear plastic strain softening for the crustal layers which depends on the integrated strain accumulation (Table 1).

Finally, the effective plastic viscosity is given by:

$$\eta = \frac{\sigma y}{2\dot{\varepsilon}}, \quad (8)$$

The material and temperature fields used as input were defined on the basis of 3D lithospheric-scale models of the SCA (Rodriguez Piceda et al., 2021, 2022) and are described along the mechanical properties corresponding to the lithospheric layers in Section 2.2. Since each conservation equation is solved using the continuity equation, the deformation takes the appearance of shear zones in numerical geodynamic modeling. Therefore, highly deformed areas may potentially represent highly “faulted areas”.

2.2 Model setup

The geometries of the lithospheric layers were adopted from the 3D structural model of Rodriguez Piceda et al. (2021). This model is built upon the integration of geophysical and geological data and models, including the gravity field, and covers a region of 700 km x 1100 km x 200 km (Figure 1). Eight layers constituting the model were defined based on the principal density contrasts in the lithosphere: (1-2) oceanic and continental sediments ('sediments', Figure 2a); (3) upper continental crystalline crust ('upper crust', Figure 2c) ; (4) lower continental crystalline crust ('lower crust', Figure 2d); (5) continental lithospheric mantle ('continental mantle', Figure 2f); (6) oceanic crust; (7) oceanic lithospheric mantle ('oceanic mantle'), and (8) asthenospheric mantle. For the geodynamic simulations, two main modifications were introduced to change the original model of Rodriguez Piceda et al. (2021). First, the model was extended 200 km in depth, 500 km in the E-W direction, and 200 km in the N-S direction. The resulting box model is 1700 x 1700 x 400 km, with a central area of interest of 600 x 600 x 400 km (Figure 3). Second, we introduced an interface representing the lithosphere-asthenosphere boundary (LAB) in the continental plate based on the thermal LAB model of Hamza & Vieira (2012). The main features of the model are depicted (Figure 2) in terms of the: (a) thickness of sediments; (b) thickness of the continental crust; (c) thickness of the upper crust; (d) thickness of the lower crust; (e) Moho depth, and (f) LAB depth.

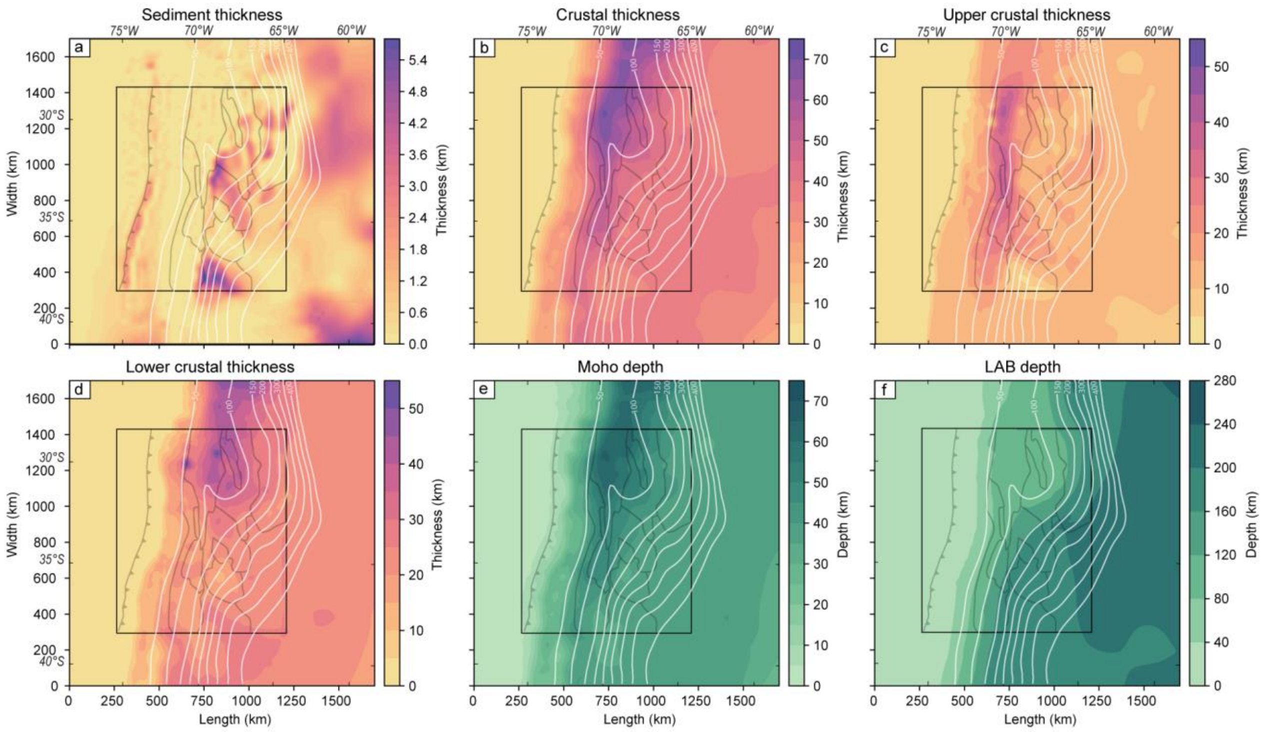

Figure 1 Layer thickness and depth map of the SCA. Main structural features of the SCA lithosphere from the model of Rodriguez Piceda et al. (2021). **a**, total crystalline crustal thickness; **b** upper continental crustal thickness; **c** lower continental crustal thickness; **d** sediment thickness; **e** Moho depth and **f** LAB depth taken from Hamza and Vieira (2012). The black rectangle shows the most refined model area.

The initial temperature field is based on a 3D thermal model of the SCA (Rodriguez Piceda et al., 2022), covering the same region as the structural model of Rodriguez Piceda et al. (2021). Temperatures were derived from the conversion of S-wave tomography (Schaeffer & Lebedev, 2013) together with steady-state conductive modeling, and were additionally validated by borehole temperatures and surface heat-flow data

(Rodriguez Piceda et al., 2022). One caveat of this model is related to the determination of the thermal structure of the oceanic slab through the conversion of S-wave tomography to temperature. The lack of seismic tomography resolution (0.5° longitudinally and 25km in depth) does not allow us to properly resolve the oceanic plate boundaries, which results in relatively high temperatures in comparison to the temperatures predicted by numerical solutions (Wada & Wang, 2009; van Keken et al., 2019). For this reason, we have assigned a conductive geotherm between 273 K and 1573 K from the top to the base of the oceanic plate as initial condition.

The thermomechanical properties of each model unit were assigned according to its lithological composition (Rodriguez Piceda et al., 2021; 2022). These lithologies were inferred from the comparison between gravity-constrained densities (Rodriguez Piceda et al., 2021) and mean *P*-wave velocities (Araneda et al., 2003; Contreras-Reyes et al., 2008; Pesicek et al., 2012; Marot, 2014; Scarfi & Barbieri, 2019), combined with rock-properties compiled from literature (Sobolev & Babeyko, 1994; Christensen & Mooney, 1995; Brocher, 2005) and other seismic properties (Wagner et al., 2005; Gilbert et al., 2006; Alvarado et al., 2007; Ammirati et al., 2013; 2015; 2018). The reference density for each composition was recalculated, so the estimated final density of each composition (i.e., after correcting for pressure and temperature, eq. 5, Table 1), is in the range of the density predicted by the structural model of Rodriguez Piceda et al (2021), and the resulting topography was compared to the present-day topography (Text B.S1 and Figure 1). The thermal properties used in the initial thermal field are from published average values for the lithology of each model unit (see references in Rodriguez Piceda et al., 2022a;

We assigned rheological properties to each composition for the viscous regime, dry olivine (Hirth & Kohlstedt, 2004, H&K2004) to the oceanic mantle (3321 kg/m³), diabase (Mackwell et al., 1998, Mck1998) to the lower crust (3129 kg/m³), wet olivine (Hirth & Kohlstedt, 2004) to the continental mantle (3388 kg/m³), wet quartzite (Gleason & Tullis, 1995, G&T1995) to the upper crust (2812 kg/m³), the oceanic and continental sedimentary layer (2300 and 2400 kg/m³) , and wet olivine (Hirth & Kohlstedt, 2004) to the upper mantle to represent the hydrated mantle wedge.

For the oceanic crust (2857 kg/m³), we prescribed a weak quartzite rheology (Ranalli, 1997) to simulate the visco-plastic behavior of a quartz-dominated "mélange", which is characteristic of the subduction interface (Sobolev et al., 2006; Muldashev & Sobolev, 2020), with a relatively low friction coefficient of 0.015, which produces an appropriate maximum shear stress of 20 to 40 MPa, depending on the temperature and the dip of the oceanic plate (Figure S4; Lamb & Davis, 2003; Sobolev et al., 2006).

For the plastic regime, we set a cohesion of 40 MPa and a friction angle of 30° to the mantle layers. The short model runtime prevents the layers from weakening by accumulating plastic strain, thus we assigned a weak plastic rheology to the sedimentary layer (i.e., a friction angle of 3° and a cohesion of 2 MPa). The minimum viscosity was set to 1e19 Pas during the first 100 ka of model run, and subsequently changed to 2.5e18 Pas.

Here, we refer to the second invariant of the square root of the deviatoric strain rate in the plastic and viscous domains as plastic strain rate and viscous strain rate, respectively. The plastic strain represents the integrated plastic strain rate over time and allows us to see the regions of the model that have been deformed and weakened during the model run. We used adaptive mesh refinement (Figure 3) to resolve the central and outer domains, with a resolution of ~6km and 12.5km, respectively. We ran the model simulation for ~250 ka while applying velocities of 5 cm/yr and 1 cm/yr to the oceanic and continental plates, respectively (Sdrolias & Müller, 2006), whereas the left and right asthenosphere borders were left open. To fulfill the volume conservation constraint, we prescribed an equivalent volume outflow to the bottom boundary equal to the prescribed inflow from the plate velocity. We use the advantages of the ASPECT code by prescribing a dynamically deformable mesh in order to simulate present-day topography. In particular, the topography in the model is uplifted and advected using the ASPECT-FastScape coupling (Braun & Willett, 2013; Bovy, 2021; Neuharth et al., 2021).

		Asthenosphere (AST)	Oceanic plate			Continental plate			
	Units	Upper mantle	Weak Gabbro	Lithomantle	Oceanic sediments	Continental Sediments	UpperCrust	LowerCrust	Lithomantle
Lithology	/	Harzburgite	Gabbro +melange (serpentinite)	Moderately depleted Lherzolite	Siliclastic	Siliclastic	Diorite	Mafic Granulite	Wet olivine
Reference	/	H&K2004	Ranalli, 1997	H&K2004	G&T1995	G&T1995		Mck1998	H&K2004
Composition used in the model	/	Dry olivine	Wet quartzite	Dry olivine	Wet quartzite	Wet quartzite		Maryland diabase	Wet olivine
Grain size	m	1e-3	1e-3	1e-3	1e-3	1e-3		1e-3	1e-3
Creep pre-exponential factor Bd / Bn	$Pa^{-ndiff/ndisl}. s^{-1}$	1e-9 / 8.49e-15	- / 2.25e-17	2.25e-15 / 2.96e-16	- / 8.57e-28	- / 8.57e-28		- / 7.13e-18	1e-9 / 2.96e-14
Grain-size exponents	mm	0	-	3	-	-		-	0
Activation energies Ed / En	kJ/mol	335 / 540	- / 154	375 / 535	- / 223	- / 223		- / 345	335 / 515
Activation volume Vd / Vn	m^3/mol	4.8e-6 / 12e-6	- / 0	10e-6 / 14e-6	- / 0	- / 0		- / 0	4.8e-6 / 14e-6
Stress exponents	n	3.5	2.3	3.5	4	4		3	3.5
Internal angle of friction	degree	30	0.8594	30	30 -> 6	3	30 -> 6	30 -> 6	30
Cohesion	MPa	40	0.1	40	20 -> 10	2	20	40 -> 20	40
Plastic strain weakening interval	none	-	0 - 0.3	-	0.5 - 1.5	0 - 1.5	0.5 - 1.5	0 - 1.5	0 - 1.5
Thermal conductivity	W/K/m	3.3	2.5	3.3	2.2	2.2	2.5	2.6	3.3
Densities	kg/m^3	3347	2857	3321	2300	2400	2812	3129	3388

Table 1 Model parameters for each composition. G&T1995 : Gleason & Tullis, 1995. Mck1998 : Mackwell et al., 1998. H&K2004.Hirth & Kohlstedt, 2004. Lithology corresponds to the one defined in Rodriguez Piceda et al., (2020) whereas representative compositions in the model are defined based on deformation experiments. Prefactors (A) were scaled from uniaxial compression experiments (Dannberg et al., 2017). We applied wet olivine (Hirth & Kohlstedt, 2004) to the upper mantle to be representative of the hydrated mantle wedge and mantle lithosphere caused by the long-term subduction at the Chile margin (Babeyko et al., 2006).

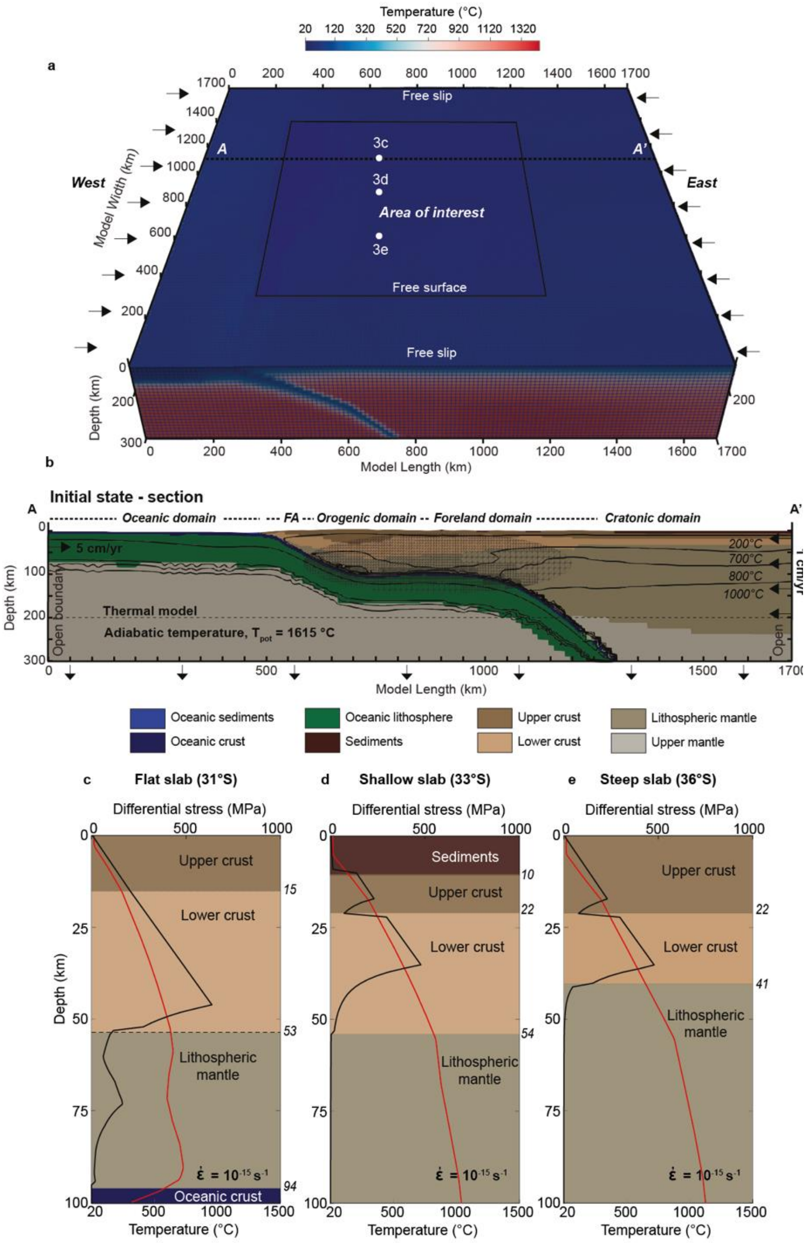

Figure 2 Model setup. **a** 3d model geometry, mesh refinement and temperature. **b** 2D W-E cross section long with location indicated in **a**, showing: boundary and initial conditions, refinement of the interface, composition of the lithospheric layers and temperature. T_{pot} indicates the mantle potential temperature and FA the forearc domain. **c-e** yield strength (black line) and temperature (red line) profiles of the upper plate at: **c** flat-slab. **d** shallow slab. **e** steep slab.

First, we computed the reference model (S1) using the parametrization discussed above (section 2.2). Subsequently, we ran a series of models (S2, S3, S4 and S5, Table 2) with varying multiple parameters to investigate the relative contribution of key factors with respect to the strain localization in the upper plate.

3. Modeling results

3.1 Reference model (S1)

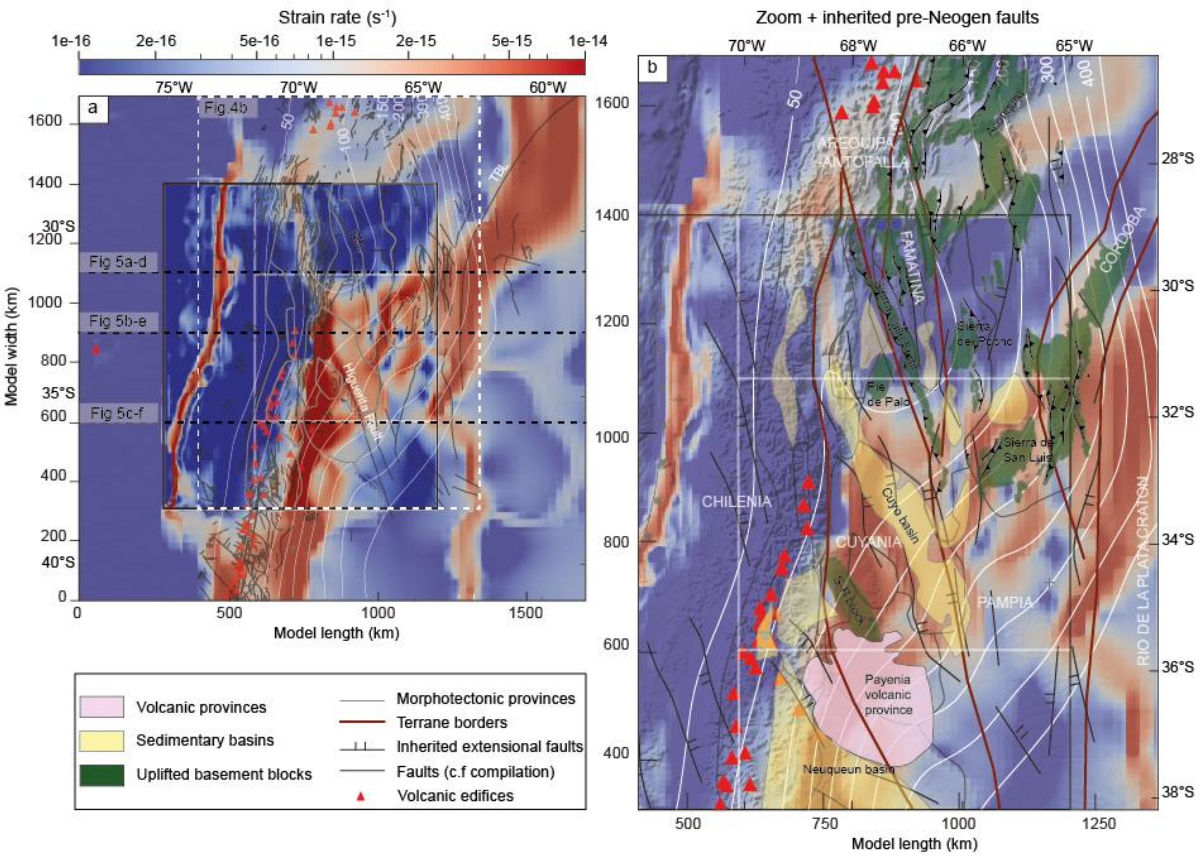

Figure 1 Surface-strain rate of the Reference model. **a.** Strain rate superposed with compiled faults (Moscoso & Mpodozis, 1988; García, 2001; Giambiagi et al., 2003; Broens & Pereira, 2005; Folguera & Zárate, 2011; Martino et al., 2016; Litvak et al., 2018; Martínez et al., 2017; Sánchez et al., 2017; Meeßen et al., 2018; Riesner et al., 2018; Olivar et al., 2018; Jensen, 2018; Melnick et al., 2020; Costa et al., 2020; Eisermann et al., 2021). **b.** Close-up of the Sierras Pampeanas morphotectonic province and extensional faults and terrane sutures in red (Ramos et al., 2002a; Wimpenny, 2022). Green structures indicate uplifted Sierras Pampeanas ranges. The timing of uplift is indicated by filled coloured circles (Table B.S1). White lines are isobaths of the top of the subducting oceanic plate. Red triangles indicate the position of known volcanic edifices. Major structures and morphotectonic provinces are highlighted by different colours in the legend.

Reference model S1 is built upon the known values for plate convergence, subduction-interface coefficient, sediment strength, and present-day topography (see Methods section). From south to north, deformation migrates to the east, with the strain localizing in the southern part, while in the northern part it is distributed over multiple faults (Figures 4 and 5). This shift is related to a change in the shortening mode from simple shear to pure shear. When considered in a strain-rate snapshot, simple-shear shortening occurs when the plastic strain-rate band in the upper crust connects with the viscous strain-rate band in the lower crust to form a shear zone (Figure 5c–d), which is expressed by thin-skinned deformation in the FTBs. Conversely, if no connection occurs between the plastic and viscous strain-rate localization zones, pure-shear shortening involving multiple faults is favored, leading to distributed deformation within the crystalline basement, which corresponds to a thick-skinned foreland-deformation style. The resulting surface strain-rate field indicates three distinct north-to-south oriented branches (Figure 4a) characterized by a distinct shortening mode:

(i) ***A Western branch between 75°W and 73°W***, which corresponds to the trench. At the trench, both plates are decoupled by the weak subduction interface, where most of the deformation localizes. Conversely, the crust of the adjacent cold and mechanically strong forearc is virtually undeformed.

(ii) ***A Central branch between* 73*°W and 70°W,*** which comprises the orogen and the adjacent foreland. Strain distribution varies from north to south. In the flat-slab segment, the strain localizes in the eastern front of the orogen and intensifies southward and the foreland crust is almost undeformed. In the shallow-slab segment, the strain distributes in the foreland over multiple oblique or en échelon, crustal-scale structures that connect to the Eastern branch and which are associated with pure-shear shortening. In the steep-slab segment, strain localizes in front of the orogen and in the foreland by simple-shear shortening.

(iii) An Eastern branch between* 60*°W and 65°W, where deformation localizes in front of the flat slab by pure-shear shortening, as well as along regions that spatially correlate with Pre-Andean cratonic structures related to the amalgamation of terranes during the formation of Gondwana, such as the Transbrazilian Lineament (Fairhead & Maus, 2003; Ramos, 2010). In the south, the deformation localizes within smaller structures that straddle the Rio de la Plata craton.

On a lithospheric scale, these three branches interact spatially. The Sierras Pampeanas morphotectonic province appears as a large-scale shear zone that accommodates deformation via en-échelon structures associated with the uplift of isolated rigid basement blocks. The deformation at the borders of these blocks is accommodated by diffuse dextral strike-slip deformation (Pons et al., 2023, will be submitted with this paper).

We also distinguish three slab segments of the subducting Nazca Plate (Figure 5): a flat segment (27°W to 32°W, 1000–1400 km model width-coordinates), a shallow segment (32°W to 35°W , a 600–1000 km model width-coordinates), and a steep segment (35°W to 41°W, 0–600 km model width-coordinates). The E-W-oriented cross sections across the reference model (Figure 5) illustrate how the plastic (brittle) and viscous deformation is accommodated in the continental plate along the segments with different slab geometry (Figure 5a–c), and how stresses are distributed within the plates (Figure 5d–f). Above the steep segment, the upper plate is characterized by simple-shear shortening at the front of the orogenic thrust wedge (Figure 5c). Above the shallow subduction segment, the model predicts a mixture of simple and pure-shear shortening

(Figure 5b). No significant deformation occurs above the flat-slab segment, while pure-shear deformation takes place at its eastern edge (Figure 5a).

The greatest horizontal stress is effectively transmitted throughout the continental plate to weak regions where the deformation localizes. In the flat-slab section (Figure 5a), deformation takes place more than ~700 km away from the trench and is localized over a 200-km-wide band in the eastern broken foreland of the Sierras Pampeanas. The model predicts local plastic (equivalent to brittle in reality) deformation (Figure 5a) on top of the colder flat-slab segment at a 100 km depth (Figure 5c), which also correlates with the bending of the slab (i.e., internal shear stress, Figure 5a, d). Horizontal stresses of > 200 MPa are generated locally in the crust and in the colder lithospheric mantle of the forearc, where the BDT is deeper, but they are not sufficiently large to cause significant deformation. The thick and warmer orogen shows no significant deformation despite being weaker, which is illustrated by the shallower BDT (Figure 5a). On top of the flat-slab segment, the greatest horizontal stress is mainly generated by the subducting plate as shown by the eastward-pointing velocity vectors (Figure 5d). The horizontal stresses also build up within the cold and strong lithospheric mantle of the foreland. Despite the presence of a weak sedimentary basin at the surface, deformation does not localize and stresses are partially transmitted eastward from the base of the upper crust to the Eastern Sierras Pampeanas. Finally, crustal shortening results in a stress drop in the eastern Sierras Pampeanas, and the polarity of the velocity field switches from east to west, indicating that velocity is now determined by the upper plate (Figure 5d).

Shortening is distributed over multiple faults within a relatively wide area (~200 km), similar to pure-shear shortening. In the shallow-slab section (Figure 5b), the plastic and viscous strain rates merge in front of the orogen (at ~800 km model coordinates) to form a deep shear zone dominated by simple-shear shortening. In the foreland, the deformation distributes over multiple faulted areas along a wide area, with rigid crustal blocks with a shallower BDT. Similarly to the previous section the deformation terminates in the transition with the cratonic domain and a thick-skinned style of deformation, which results from pure-shear shortening. The horizontal stress also builds up locally in the cold forearc (>~200 MPa; Figure 5e), where the great mechanical strength of the rocks prevents failure and causes a transmission of stresses to the orogen. Additionally, the horizontal stress builds up in the lower crust and partially transmitted to the Eastern Sierras Pampeanas. Strain localizes at the orogenic front by simple-shear shortening and is accommodated y pure-shear shortening in the foreland and at the transition with the cratonic domain. In the steep-slab section, the deformation strongly localizes in front of the orogen (~800 km model length; Figure 5c).

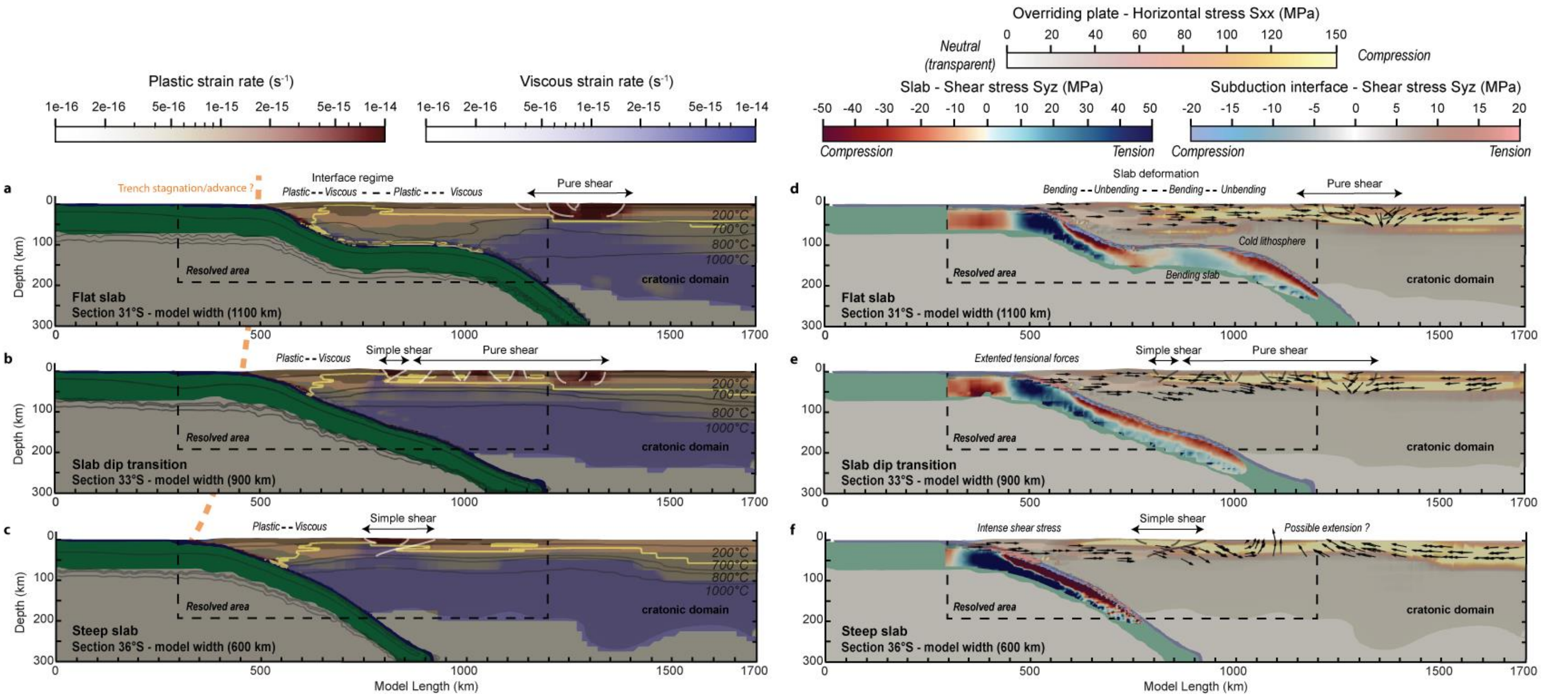

Figure 2 Representative cross sections of the subduction segments for the reference model (see location in Figure 1): Strain rate **(a-c)** and stress (**d-f**). **a-d** Flat-slab (31°S). **b-e** Shallow slab (33°S) and **c-f** Steep slab (36°S). **a-c** white lines are interpreted faults, yellow lines show the depth of the brittle-ductile transition (BDT), and dark lines indicate isotherms. **d-f** black lines indicate the interpreted faults, arrows indicate the sense of the velocity for the crust.

297

3.2 Model variations

In this section, we test the relative contribution of four key parameters on the resulting surface strain-rate distribution: (1) the friction coefficient at the oceanic plate interface, (2) the strength of continental sediments, (3) the topography, and (4) the velocity applied to the model boundaries. The friction coefficient at the oceanic plate interface is varied between 0.005 and 0.05 (models S2a-c) in agreement with the models of the long-term evolution of the Central Andes (Sobolev et al., 2006; Sobolev & Babeyko, 2005). The internal friction angle (Φ) and cohesion (C) of the sediments is varied from 3° to 30° (friction coefficient 0.05 to 0.5) and from 2 to 20 MPa, respectively (Figure 6, models S3a-d). In addition, we tested the effect of topography on the strain distribution by removing the topographic relief in the initial configuration with and without applied velocities at the boundaries (Figure 6, models S4a-d). Finally, the oceanic and continental plate velocities are varied between 0 cm/yr and 6 cm/yr, covering the range of possible velocities (Figure 6, models S5a-d). Table 2 summarizes the alternative model runs. In order to discuss the relative effect of each key parameter to the strain localization we computed the residual surface strain rate between the model variant and the reference model (Figure S3). To estimate the variation in strain localization above the trench related to flat, shallow, and steep subduction, we divided the surface of each model into sub-domains. For each domain, we calculated an average of the strain rate using the root mean square. Finally, we calculated the relative change between the domains of the model variants and of the reference model. Thus, we obtained a summary of the relative percentage of contribution of each key parameter to the reference model for each domain (Figure 7). Note that for a similar budget of force between the reference model and the model variants, if the strain at the surface localizes further in one of the branches (section 3.1), it may decrease in another one to keep the balance. Because part of the forces might be redistributed outside of the area of interest, the net percentage of the domains might not be equal to 100%.

Group	**Name**	**Variation**
Friction coefficient of the subduction interface (μ_{int})	S2a	μ_{int} = 0.005
	S2b	μ_{int} = 0.035
	S2c	μ_{int} = 0.05
	S2d	μ_{int} = 0.07
Sediment strength (internal friction angle Φ and cohesion C)	S3a	Φ = 30° ,C = 20 MPa
	S3b	Φ = 30°, C = 2 MPa
	S3c	Φ = 15°, C = 20 MPa
	S3d	Φ = 3°, C = 20 MPa
Model with variation of the topography	S4a	no initial topography w/ boundary velocity
	S4b	no initial topography, w/o boundary velocity
	S4c	no topography w/ boundary velocity
	S4d	no topography w/o boundary velocity
Velocities of the subducting plate (SP) and the overriding plate (OP)	S5a	SP= 0 cm/yr , OP= 1 cm/yr
	S5b	SP= 5 cm/yr, OP = 0 cm/yr
	S5c	SP = 6 cm/yr, OP = 0 cm/yr
	S5d	SP = 0 cm/yr, OP = 6 cm/yr

Table 1 Model variations with respect to the reference model.

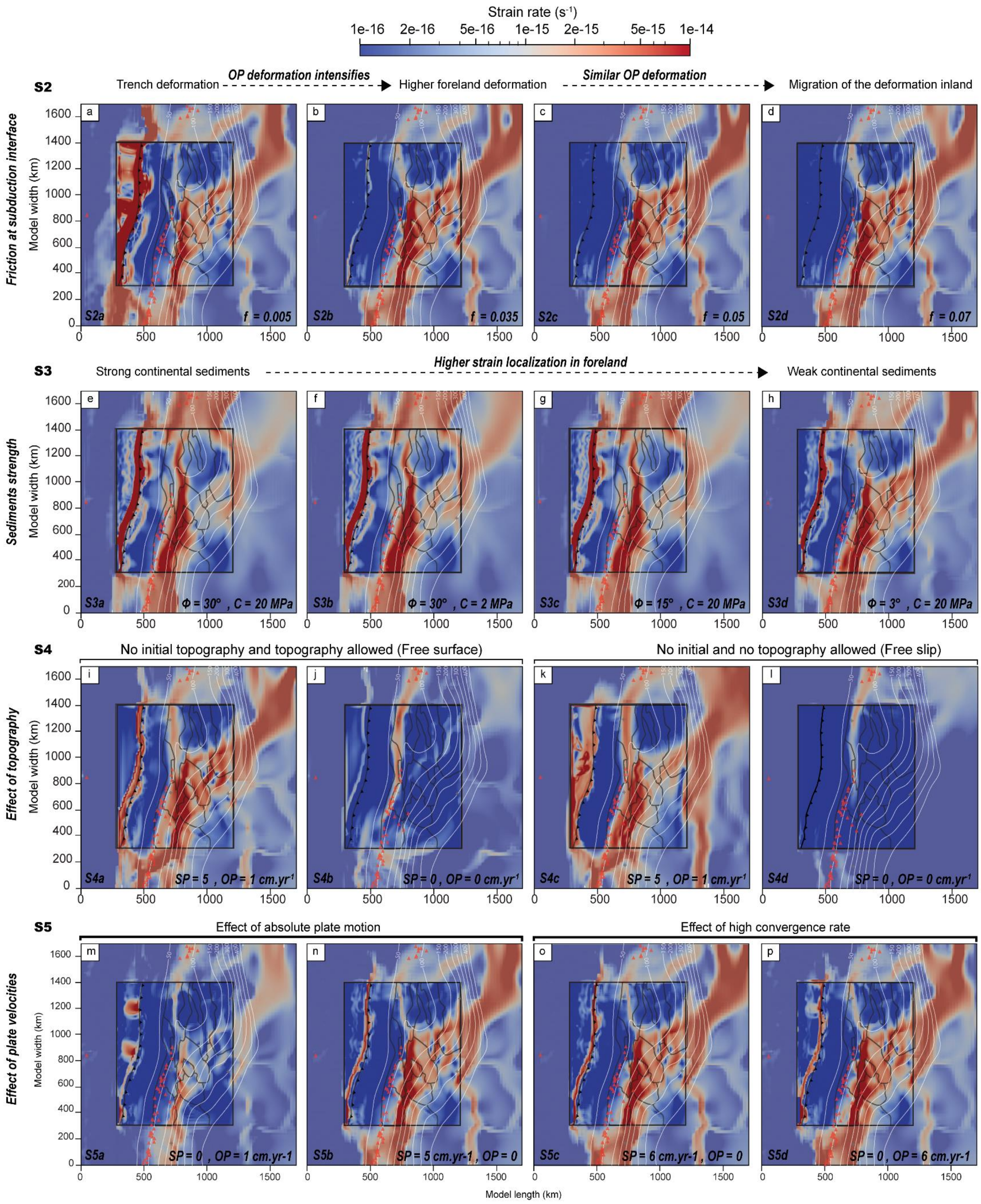

Figure 3 Strain-rate distribution in various models. **a-d** Models with variable friction coefficients (f) at the subduction interface: **a** S2a, f 0.005. **b** S2b, f 0.035. **c** S2c, f 0.05. **d** S2d, f 0.07. **e-h** Models with alternative strength (Φ internal friction angle, and C cohesion) of the sedimentary layer. **e** S3a, Φ = 30° C = 20 MPa. **f** S3b, Φ = 30° C= 2 MPa. **g** S3c, Φ = 15° C= 20 MPa. **h** S3d Φ =3° C=20 MPa. **i-l** Models without prescribing initial topography. **i-j** Free surface with advection of the topography allowed. **k-l**

Free-slip, no advection of topography allowed. **I, k** models with plate velocity, SP = 5 cmyr-1 and OP =1 cmyr-1 . **j,l** models without velocity, SP and OP = 0 cmyr-1. For abbreviations of plate velocities, see table 2. **m-p** Models with variations of prescribed plate velocity. **m** Absolute overriding plate velocity orthogonal to the trench, no subducting plate velocity. **n** Absolute subducting plate velocity orthogonal to the trench, no overriding plate velocity. **o** Convergence velocity, applied only to the subducting plate. **p** Convergence velocity, applied only to the overriding plate. Black rectangle is the resolved area; dark line indicates the boundaries of the morphotectonic provinces, red triangles denote position of volcanic edifices.

3.2.1 Models with variable slab-interface friction (S2a-d)

The greatest differences between the reference and alternative models related to the slab interface friction occurs along the trench (Figure 6). With low slab interface friction (S2a; Figure 6a), the strain strongly localizes more at the trench (x18 or +994%, Figure 7). Less strain localizes within the overriding plate (-27 to -54%), including the orogen and the back-arc. Conversely, higher interplate friction (S2b-c; Figure 6b-d) translates into a twofold lower strain localization at the trench (-92 to 97%), and slightly higher overriding plate deformation (+6%, Figure 7). Therefore, for these short simulations the increase of friction at the interface results in similar intensity of upper-plate deformation with respect to the reference model S1.

3.2.2 Strength of continental sediments (S3a-d)

Modifying sediment strength results in a significant change in strain-rate distribution. Weaker sediments lead to a higher degree of strain localization adjacent to the orogen and the foreland basins (S3a-d, Figure 6e-h). A decrease in the internal friction angle (S3c and S3d, Figure 6f and h) decreases the strength significantly more than a decrease of cohesion (S3b and S1, Figure 6g and Figure 4), promoting the compressional reactivation of foreland structures. With high friction and cohesion (S3a, Figure 6e), the strain rate in the foreland appears to be more diffuse and less localized (-35 and -40%), causing strain to localize closer to the orogen and the trench (+220%) compared to the reference model (Figure 7). With weaker continental sediments, the major component of deformation switches from the orogen interior outward to its front. Overall, stronger sediments result in more active shallow deformation near the trench and in the orogen above the flat slab (S3a, 423%), and less pronounced deformation in the foreland above the shallower and steeper domains (~-40%, Figure 7).

3.2.3 Models with topography variations (S4a-d)

By initializing the model without present-day topography, we aim to look at the effect of internal forces related to the density and thickness configuration of the overriding plate layers. In models S4a and S4b, we allow for the topography to evolve with and without plate velocities, respectively (Figure 6i-j). S4a exhibits a strain-rate distribution similar to S1 (cf. Figure 6a), but with higher strain localization at the trench and in the orogen on top of the flat-slab (+25 and 38%, Figure 7). In S4b, although no horizontal velocity is prescribed, the strain rate is higher in the orogen on top of the flat slab (+30%) and lower elsewhere. To investigate the effect of topography on the strain distribution, we ran two alternative models inhibiting topographic growth, with and without plate velocities (models S4b-c; Figure 6j-l). In the model with plate velocities (S4c) the strain rate is higher at the trench and the orogen on top of the flat-slab (+128 and 101%), and it is more diffuse and lower in the foreland of the shallow and steep-subduction domains (-23% and -36%). Without plate velocities (S4d), the strain rate only localizes in a narrow corridor along the orogen and otherwise decreases elsewhere.

3.2.4 Velocity boundary conditions (S5a-d)

Varying the prescribed boundary velocity allows us to determine the contribution of each plate to the intensity of strain localization in the overriding plate. In model S5a (Figure 6m), where velocities are only prescribed to the overriding plate (1cm yr^{-1}; Figure 6m), the intensity of the deformation in the foreland is lower by 58 to 83% in all domains compared to model S1 (Figure 7) because the deformation slightly localizes at the trench in specific places. In model S5b, where the overriding plate does not advance trenchward, the deformation decreases everywhere by 15 to 30%, likely because the strain efficiently localizes in the orogen and the foreland (Figure 6n). Models S5c and S5d (Figure 6n-o) show that a deformation intensity similar to the reference model can be reached if the total convergence velocity is applied to either the lower or the upper plates. Overall, a fast convergence rate controls the intensity of the deformation and its localization. In these models, the contribution of the subducting plate velocity seems more important than that of the overriding plate, although a fast overriding plate velocity (S5d) can lead to similar degree of deformation as in the reference model. The strain-rate distribution in the overriding plate does not depend on the side of the prescribed velocity. The models that prescribe velocity from the west with the subducting plate (S5c) or from the east with the overriding upper plate (S5d) show similar structures and patterns (Figure 6o-p).

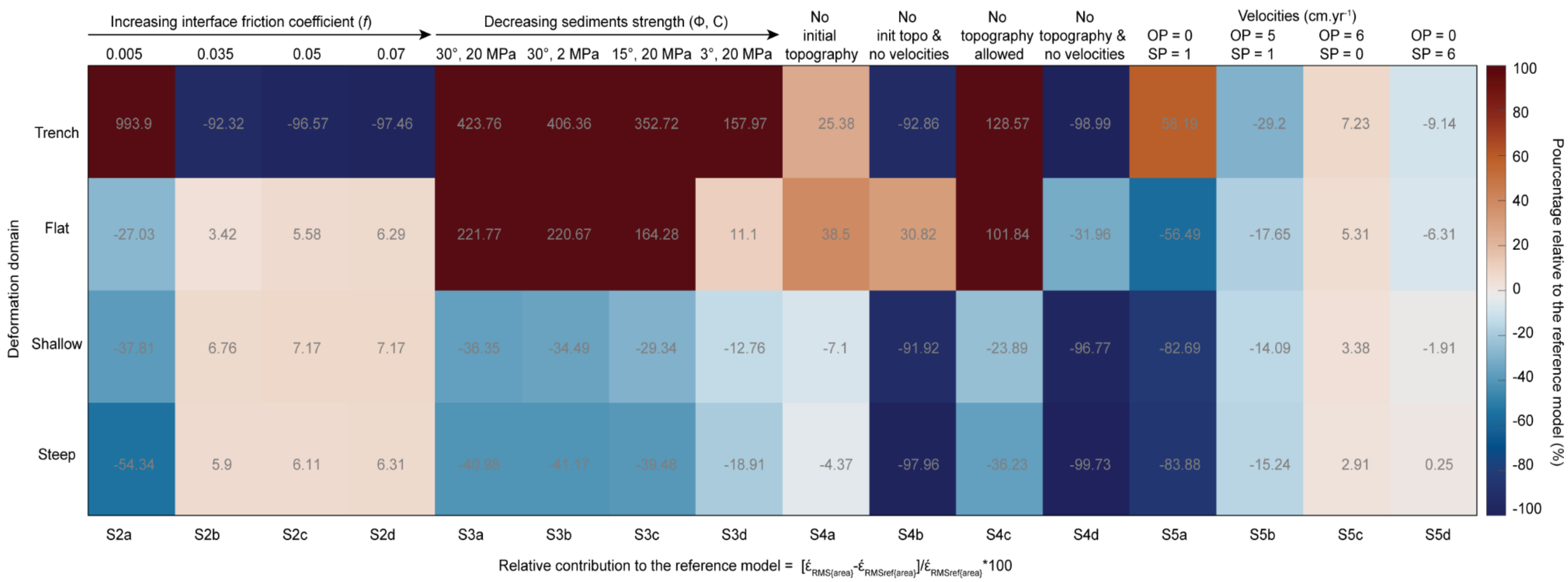

Figure 4 Relative surface strain-rate difference between the reference and the model variants. Relative change of strain rate in percentage $[\acute{\varepsilon}\mathrm{RMS(area)} - \acute{\varepsilon}\mathrm{RMSref(area)}] \,/\, \acute{\varepsilon}\mathrm{RMSref(area)} * 100$ with respect to the reference model in each deformation domain for each model variant.

4. Discussion

To analyze the roles of inherited heterogeneities in the continental plate and oceanic plate geometry we assess the relative contribution of the overriding plate strength with respect to strain localization along-strike. We first compare the distribution of modeled strain-rate patterns with the mapped structures (Section 4.1). Next, we discuss each of the tested key factors and how they affect the strength in our model, and their contribution to strain localization. We then discuss the role of shallow and deep-seated structures (e.g., sediment strength, topography, and the thermal state and thickness of the lithosphere, section 4.2, Figure 8). Finally, we examine the effect of slab geometry (flat, shallow, and steep subduction) regarding the distribution and style of deformation in the foreland (section 4.3).

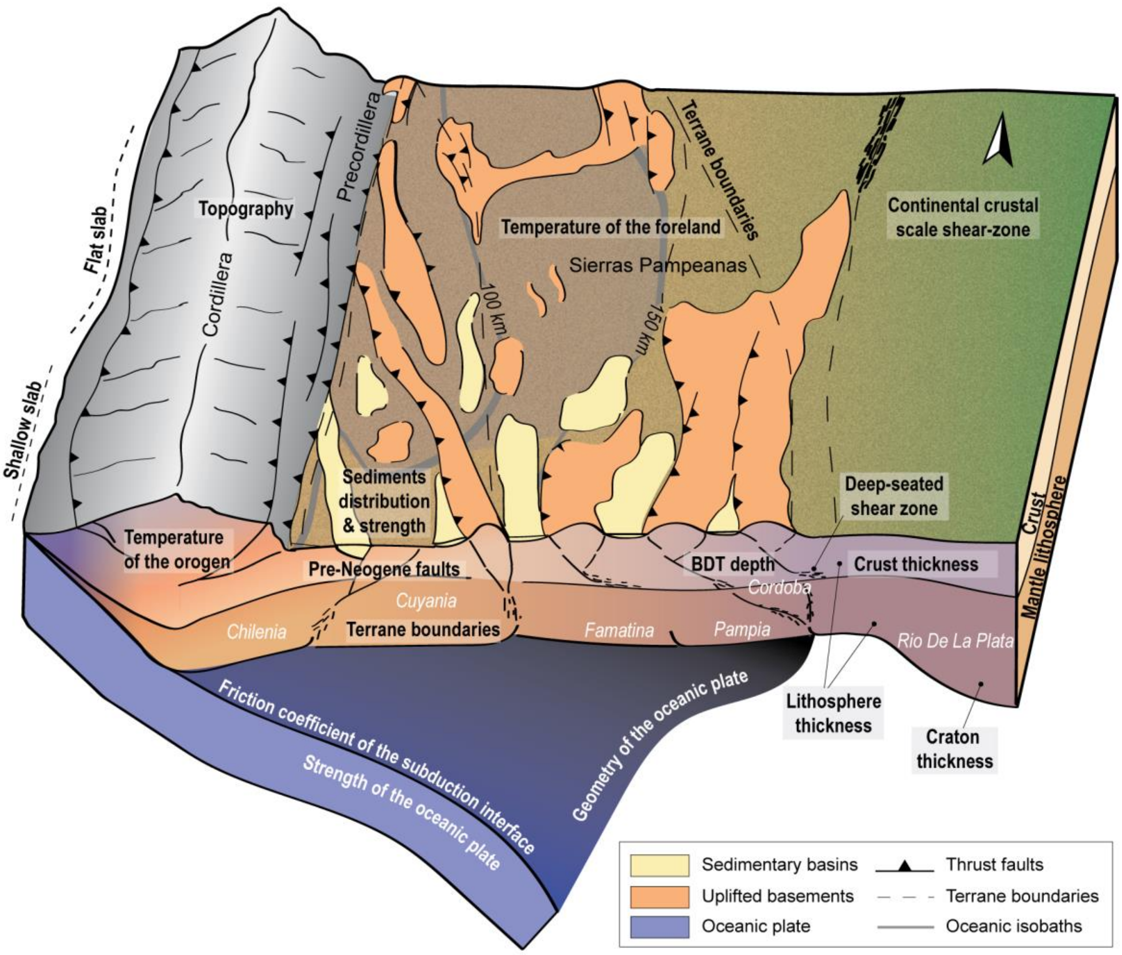

Figure 8 Schematic 3D diagram showing the possible processes (in bold) and inherited structures that can affect strain localization and the tectonic foreland deformation style in the Sierras Pampeanas.

4.1 Correlation with mapped structures

Our modelling results can be compared with observed surface faulting. Although we do not implement faults in the models explicitly, sediment accumulation is partly associated with their activity. In the investigated area, Mesozoic deposits are controlled by normal-fault bounded, extensional basins, while reverse faults cause sediment accumulation at their footwalls. Therefore, sediment strength and pre-existing faults related to a different kinematic regime may strongly affect the location of deformation and the reactivation of shallow inherited faults, which explains why structures resulting from the strain-rate map of the reference model are spatially well correlated with exposed faults (Figure 4a-b). In particular, the strain-rate distribution in the reference model correlates with Quaternary faults located at the front of the orogen in the foreland fold-and-thrust belts (e.g., Malargue, San Rafael FTB), at the borders of the basins (e.g., Cuyo Basin), and with the faults uplifiting the Sierras Pampeanas basement blocks. In some cases, inherited Pre-Andean structures have been reactivated that were associated with the amalgamation of Paleozoic crustal terranes at the western margin of Gondwana (Introcaso & Ruiz, 2001; Vietor & Echtler, 2006; Ortiz et al., 2021). For instance, faults associated with the Desaguadero-Bermejo lineament (DBL) close to the Sierra Valle Fértil in the western Sierras Pampeanas (Figure 4b, Introcaso & Ruiz, 2001) are associated with structures related to the Ordovician collision of the Cuyania and Pampia terranes (Ramos, 2010). This strike-slip fault was reactivated during the Neogene (Introcaso & Ruiz, 2001). The model also predicts the reactivation of the Transbrazilian lineament (TBL), a major Proterozoic transpressive shear zone that borders the thicker mantle lithosphere of the Rio de la Plata craton (Figure 4b, Cordani et al., 2013; Casquet et al., 2018). In contrast, the forearc is subjected to a low degree of deformation and acts as a rigid body (Tassara & Yáñez, 2003; Tassara, 2005; Hackney et al., 2006), although previous studies have shown that the forearc experienced a certain degree of Quaternary deformation (González et al., 2003; Melnick et al., 2006; Regard et al., 2010). The mobility of the forearc is controlled by the long-term weakening associated with strain partitioning that is caused by oblique plate convergence (Melnick et al., 2006; Rosenau et al., 2006; Eisermann et al., 2021), which is not considered in our model. Other regions that exhibit a low degree of deformation include the foreland above the flat-slab segment (Figure 5a) and the back-arc in the steep-slab segment (Figure 5c). In the latter case, most of the deformation is related to pre-Neogene structures (e.g., Folguera & Zárate, 2009).

4.2 Upper-plate control on strain localization

The strength of the overriding plate controls strain localization and results from contributions exerted by the frictional (brittle) and viscous (ductile) strength (Babeyko et al., 2006; Mouthereau, 2013; Jammes & Huismans, 2012; Liu et al., 2022). Several processes may weaken the plate and influence the localization of deformation. In our study we distinguished between shallow and deep-seated contributors, depending on their control on the frictional and viscous strength, respectively.

An important component of the stress is transmitted through the frictional regime (Figure 5), thus shallow contributors can significantly affect strain localization through frictional weakening. The variations in frictional strength are related to the tectonic history of the region, and are modulated by several features. These include the sediment strength relative to the underlying structures (Babeyko et al., 2006; Erdős et al., 2015; Mescua et al., 2016; Liu et al., 2022), the presence of inherited (Pre-Andean) faults and fabrics and their orientation with respect to the convergence direction (Allmendinger et al., 1983; Kley, 1999; Kley & Monaldi, 2002), and topography (Molnar & Tapponnier, 1975; Chen & Molnar, 1983; Stüwe, 2007; Mareschal & Jaupart, 2011; Liu et al., 2022). In turn, the deep-seated contributors are those affecting the strength of the crust and the lithospheric mantle through temperature variations. The extent to which shallow and deep-seated contributors interact and affect the strength of the overriding plate in the SCA, is discussed in the following sections.

4.2.1 Shallow structures

Previous studies have shown the important role of the thickness and strength of sediments in shallow strain localization (Babeyko et al., 2006; Erdős et al., 2015; Mescua et al., 2016; Liu et al., 2022). In the Central Andes, the presence of mechanically weak and porous Palaeozoic sediments in the foreland spatially correlates with a change of deformational style from thin-skinned to thick-skinned deformation in strain rate map the transition between the Subandean FTB and the broken foreland province of the Santa Barbara System of northwestern Argentina (Allmendinger et al., 1983; McGroder et al., 2015; Pearson et al., 2013). Previous numerical models have shown that a low friction coefficient of the sediments (<0.05) promotes asymmetric deformation, a simple-shear shortening and thin-skinned deformation style, which may constitute a necessary condition to initiate foreland underthrusting of the Brazilian Shield (Sobolev et al., 2006; Liu et al., 2022; Pons et al., 2022). Additionally, Ibarra et al. (2019) have proposed that deformation tends to localize within the areas with large lateral variations of crustal strength, such as the foreland where a thick sedimentary layer is present. Our results show that the distribution of sediments inherited from past tectonic events largely control shallow strain localization (Figure 2d, Figure 6 and 7, S3a-c). Sediments tend to accumulate at the footwall of the faults or close to uplifted basement blocks. In addition, some of these depocenters had already formed during Palaeozoic to early Mesozoic extension, which could also have weakened the basement (Mescua et al., 2016). In our model, efficient simple-shear shortening is favored by the thick sedimentary layer of the foreland basin, which generates a detachment fault connecting plastic (brittle) and viscous strain rates in the upper and lower crust, respectively (Figure 5). In case that such a connection is not possible, shortening is accommodated by pure shear and deformation distributes along multiple symmetrical faults (Figure 5). Model variations S3a-d show that weaker sediments are required to localize the deformation along specific discrete faults and structures (e.g., at the borders of the uplifted basement blocks or the Bermejo basin; Figure 6, S3c). Conversely, strong sediments (e.g. model S3a) with a small strength contrast with respect to the upper crust lead to a broad, diffuse shear zone in the foreland above the flat-slab segment (Figure 6e-h).

An additional factor that is proposed to exert major control on strain localization is topography. In the orogen, the gravitational potential energy constitutes an important resistive force to orogenic growth (Molnar & Tapponnier, 1975; Chen & Molnar, 1983; Stüwe, 2007; Mareschal & Jaupart, 2011; Liu et al., 2022). If horizontal forces are not sufficiently strong to overcome gravitational stresses exerted by the topography of the orogen, the horizontal stresses migrate laterally to the periphery of the orogen and strain localized in the foreland. This effect is highlighted in Model S4c (Figure 6k), where no topography is allowed to grow, thus the deformation is less efficiently transmitted and localized in the weak areas of the foreland. Topography can also exert an indirect effect on deformation localization if the uplifted foreland basement blocks are bounded by faults and adjacent sediment depocenters, which promotes the localization of deformation as discussed previously in this section. In the alternative models without initial topography (Model S4a, Figure 6i) or where no topography is allowed to grow (Model S4c, Figure 6k), the removal of the orogenic load fosters strain localization in the orogen. Additionally, the models without prescribed velocities (Models S4b, Figs. 6j and l) indicate that a low portion of the strain rate in the northern orogen in the model could result from some dynamic effect of the flowing mantle asthenosphere.

4.2.2 Effect of deep-seated inherited structures.

The viscous strength of the continental crust and mantle lithosphere strongly depends on their composition, inherited thickness and on their thermal state because of the strong dependence of viscosity on temperature (Sippel et al., 2017; Anikiev et al., 2020; Ibarra et al., 2021; Rodriguez Piceda et al., 2022b). In the orogen, higher temperatures decrease the depth of the brittle-ductile transition favoring viscous deformation and crustal flow which may facilitate the connection with the plastically deforming foreland sediments, ultimately promoting simple-shear deformation (Liu et al., 2022). Additionally, for an orogenic crust of more than 60 km thickness, simple shear is almost always the preferred mode of foreland deformation (Liu et al., 2022). In contrast, a cold, rigid lithosphere can act as an indenter by transmitting horizontal stresses to its front, localizing the deformation at the transition between strong and weak domains (Calignano et al., 2015; Tesauro et al., 2015; Rodriguez Piceda et al., 2022b, Ibarra et al., 2021).

The lithospheric thermal field in the SCA is the result of the contributions from the compositional and thickness configuration of the lithospheric layers and the basal lithospheric heat flow (Rodriguez Piceda et al., 2022a). The crustal thermal field mainly depends on the volumetric heat capacity of the radiogenic upper crust, whereas the thermal field of the mantle is strongly perturbed by the cooling effect of the subducting slab, which changes as a function of the slab dip and geometry (Rodriguez Piceda et al., 2022a). In the northern part of the orogen, the effect of the thick felsic radiogenic crust (Figure 2) overprints the cooling effect of the flat slab (Rodriguez Piceda et al., 2022a). Therefore, the northern part of the orogen would be expected to deform actively, which contradicts our model results and the lack of observed seismicity in the area (ISC catalog, Rodriguez Piceda et al., 2022b; Figure S2). To explain this apparent contradiction (i.e., no deformation of the upper plate), an additional mechanism must be invoked (further discussed in Section 4.3). Conversely, the lithosphere in the northern foreland is characterized by a thinner radiogenic upper crust (Figure 2) which does not overprint the cooling effect of the flat-slab, thus resulting in a colder and stronger lithosphere. This strengthening allows for an efficient stress transmission from the oceanic plate to the continental plate between western and eastern domain above the flat-slab segment. Additionally, the strong, thick cratonic domain (Figure 2f) allows for an efficient transmission of stresses to the west. Consequently, the deformation localizes at the eastern edge of the broken foreland where the effects of forces applied from the subducted plate and the cratonic part of the continental plate meet (Figure 5a). Finally, the deformation is intensified by the overlying weak sediments.

Other deep lithospheric processes, such as eclogitization of the crust and delamination of the lithospheric mantle, are not considered in our models, they could also weaken the overriding plate and facilitate strain localization (Babeyko et al., 2006; Sobolev et al., 2006). However, in the southern Central Andes, there is no evidence of delamination and extensive eclogitization below the Western Sierras Pampeanas and Precordillera (Alvarado et al., 2007, 2009; Ammirati et al., 2013; 2015; 2018; Gilbert et al., 2006b; Marot et al., 2014). Thick, warm orogenic crust (>~45 km) can also be subjected to intracrustal convection and partial melting, further weakening the overriding plate (Babeyko et al., 2006). Nevertheless, such thickness values are only reached (Assumpção, 2013; Rodriguez Piceda et al., 2021) where the lack of volcanism between ~27°S - 33°S (Figure 1) indicates a decrease in the lithospheric basal heat flux during the last ~6 Ma (Barazangi & Isacks, 1976; Isacks et al., 1982; Jordan et al., 1983; Kay et al., 1987; 1991; Jordan et al., 1993; Ramos et al., 2002a; Ramos & Folguera, 2009; Rodriguez Piceda et al., 2022b), preventing partial melting and crustal convection in the southern Central Andes.

4.3 Lower-plate control on strain localization

In the SCA, the role of the flat-slab on the stress regime and the localization of deformation in the upper plate is a matter of ongoing debate (Jordan et al., 1983; Gutscher et al., 2000; Folguera et al., 2009; Gutscher, 2018; Horton, 2018; Martinod et al., 2020). Along the tectonically active Pacific rim steep subduction is associated with a low degree of coupling, upper-plate extension, and back-arc spreading (Mariana type), while low-angle subduction cause close plate coupling, upper-plate compression and shortening (Chile type) (Barazangi & Isacks, 1976; Uyeda & Kanamori, 1979; Ramos & Folguera, 2009; Horton, 2018). Eastward-directed compression in the Central Andes is driven by basal shear stress exerted by the underlying flat-slab (Gutscher et al., 2000). Additionally, the passage of the flat-slab weakens the overriding plate mechanically by scraping the continental lithospheric mantle, ('bulldozed mantle-keel' model, Liu & Currie, 2016; Gutscher, 2018; Axen et al., 2018) and thermally by exposing the remaining lithosphere to the warmer asthenosphere (Isacks, 1988). More recent studies, however, have emphasized that the stress regime of the overriding plate is probably more influenced by the velocity difference between the overriding plate and the trench rather than by the subduction angle (Lallemand et al., 2008; Faccenna et al., 2017, 2021). The velocity of trench retreat can be perturbed by a rapid change in the subduction angle, which can be caused by the interaction between the slab and the mantle transition zone (Čížková & Bina, 2013; Cerpa et al., 2015; Briaud et al., 2020; Pons et al., 2022). The absolute motion of the South American plate prescribed in model S1 is considered to be the driving force of the Andean orogeny (Sobolev and Babeyko, 2005; Husson et al., 2008; Martinod et al., 2010); nevertheless, when viewed at shorter geological timescales, model variants such as model S5b-d, illustrate that a similar strain rate as in model S1 can be achieved with a different redistribution of plate velocities while maintaining a similar convergence rate (Figure 6 and 7). This implies that at shorter timescales, the parameter convergence rate is potentially more important than absolute plate velocity.

In our simulations, the subduction angle of the oceanic slab also controls the distribution of strain localization in the upper plate. The flat slab propagates stresses eastward causing shortening to take place in front of the flat slab, as proposed by the 'bulldozed mantle-keel' models ('slab bulldozing', Gutscher, 2018; Axen et al., 2018). Strain localization could be favoured by inherited crustal-scale structures such as the Transbrazilian lineament in the SCA (see Section 4.2.1). Conversely, the cratonic domain also transmits horizontal stresses westward across the continental plate and amplifies the intensity of deformation (Figure 5). Interestingly, our results predict almost no deformation in the upper plate overlying the flat-slab segment (27°S–32°S). This is consistent with limited seismic activity observed in the orogenic domain overlying the flat slab segment (Figure S2). We suggest that this is the result of upper-plate strengthening at these latitudes due to cooling as discussed above (cf. section 4.2.2) and caused by the underplated oceanic slab at the base of the continental lithosphere. The notion that the upper plate is shielded from deformation in the flat-slab segment is also supported by the decrease in shortening in the Precordillera at ~9Ma at 30°S following the arrival of the Juan Fernandez Ridge at 12 Ma (Yáñez et al., 2001; Allmendinger & Judge, 2014; Bello-González et al., 2018).

The colder subduction interface along the flat-slab segment (Figure 5a) also contributes to an increase in the coupling between the plates, and can locally reach shear stresses >35 MPa (Figure S4). Moreover, the low temperatures of the subduction interface combined with its low frictional strength could deepen the BDT of this discontinuity to 100 km depth (Figure 5a). The shear stresses at the plate interface decrease southward, which is supported by the increased thickness of the trench-fill sediments south of 33°S (Bangs & Cande, 1997; Völker et al., 2013). A comparison with the average shear stress at the plate interface suggested by Lamb & Davis (2003; Figure S4) shows that our reference model (f=0.015) may underestimate the shear stress at the flat-slab interface, whereas model S2d (f=0.07) may overestimate it.

In contrast to the flat-slab segment, deformation in the steep-slab segment (36°S–40°S) localizes along the front of the orogen, which shows that deformation cannot be efficiently propagated to the eastern domain if the oceanic slab is steeply dipping. Alternatively, the transition between the steep and flat-slab geometry results in the formation of an intermediary shallow segment (32°S–36°S). Above this segment a large crustal shear zone develops in the broken foreland that results from the offset of strain localization between the flat and steep slabs. In such a scenario deformation takes place via multiple faults that border the basement ranges of the Sierras Pampeanas (Figure 5d), and the strain localization along these faults is enhanced by the presence of weak sediments (Models S2, Figure 6a-d). From a dynamic point of view, we suggest that the shallowing of the slab generates crustal contraction prior to slab flattening in response to a large transpressive shear zone in the southern Sierras Pampeanas. Accordingly, deformation could be accommodated by a combination of strike-slip deformation at the borders of the uplifted basement blocks and block rotation. This mechanism, that we name "flat-slab conveyor", is further investigated in a related publication (Pons et al., 2023, related manuscript).

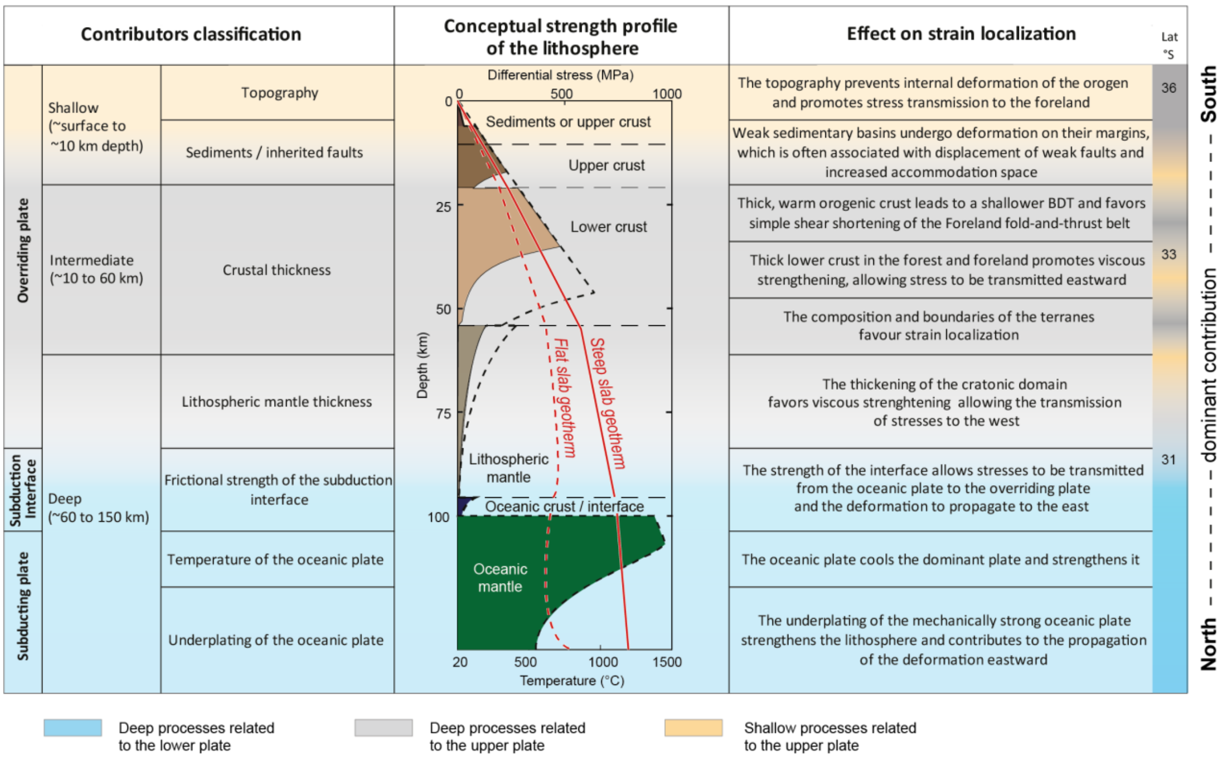

Figure 9 Summary of the main contributors to strain localization in the Southern Central Andes indicates a north-south-directed switch from deep to shallow-seated factors.

5. Conclusions

Using 3D data-driven geodynamic subduction modeling, we analyzed the relative contribution of subducting plate geometry and shallow and deep-seated crustal-scale and lithospheric structures of the overriding plate on strain localization in the SCA. Our modelling results provide a better understanding the Cenozoic interaction between the Pampean flat slab and the South American plate in the region of the southern Central Andes between 27° and 32°S and within the transition to a steeper subduction segment farther south. The flat slab controls upper-plate deformation in the northern part of the SCA by strengthening the lithosphere of the upper-plate and by cooling the overriding plate through underplating, thus shielding the upper plate of the flat-slab subduction system from pronounced deformation. Consequently, deformation propagates toward the eastern edge of the flat slab by a bulldozing effect. This deformation is accommodated in the eastern broken foreland, where the slab is already dipping steeply.

The inherited structures in the overriding plate contribute to the strain localization in multiple different ways. (i) In the compressional Cenozoic setting of the flat-slab region sediment distribution can be viewed as a proxy for the distribution of major faults, because depocenters usually form at their footwalls. Weaker sediments, and therefore weaker faults, significantly intensify deformation in the flat-slab segment. (ii) Inherited crustal-scale fault zones, such as the TBL located within the transition to the cratonic domain, may be preferentially reactivated and localize deformation as seen in the eastern Sierras Pampeanas. (iii) The localization of deformation in the forearc may be controlled by strain partitioning and long-term strain weakening related to the obliquity of convergence. (iv) A thick crust may control the temperature of the continental crust due to the contribution of radiogenic heating, thus affecting the depth of the brittle-ductile transition (BDT). For a thicker felsic crust the BDT is shallower, which promotes the development of deep-seated, asymmetric décollements and simple-shear shortening in the fold-and-thrust belts. In contrast, a thinner upper continental crust causes a deeper BDT as observed in the Sierras Pampeanas and fosters the activity of multiple symmetric faults and pure-shear shortening. (v) Surface topography may also exert a significant influence on strain localization within the orogen by transmitting horizontal stresses toward the foreland.

6. Acknowledgements

This research was funded by the DeutscheForschungsgemeinschaft (DFG) and the Federal State of Brandenburg under the guidance of the International Research Training Group IGK2018 “SuRfAce processes, TEctonics and Georesources: The Andean foreland basin of Argentina” (STRATEGy DFG 373/34-1). The authors thank the Computational Infrastructure for Geodynamics (geodynamics.org), which is funded by the National Science Foundation under award EAR-0949446 and EAR-1550901, for supporting the development of ASPECT. The computations of this work were supported by the North-German Supercomputing Alliance (HLRN). Stephan V Sobolev was funded by the ERC Synergy Grant Project MEET (Monitoring Earth Evolution through Time, Grant 856555). The authors thank Corinna Kallich for her comments and suggestions on the design of the figures.

7. Data availability

The input files to reproduce the results of this paper are available at the following link https://dataservices.gfz-potsdam.de/panmetaworks/review/ff12e9fd34522339dfaf9c7e6bb578a085072f2addfc921cf09b47010c4213ee/ (https://doi.org/10.5880/GFZ.2.5.2023.001, Temporary link for review from the GFZ metadata service). Figures in the paper were made with Paraview and Illustrator. The color scales were taken from Crameri (10.5281/zenodo.5501399).

8. Code availability

The ASPECT code is open source and hosted on github https://github.com/geodynamics/aspect. The models were run with the ASPECT version 2.3.0-pre built with the 9.2.0 version of Deal.ii. We have modified the main ASPECT branch to implement new custom plugins necessary for the model set up and the postprocessing accessible at https://github.com/Minerallo/aspect/tree/Paper_Data_driven_model_Southern_Andes.

9. Author contributions

Michaël Pons: Conceptualization, software, Formal Analysis, Data curation, Investigation, Visualization, Writing - original draft, Writing - review & editing, Constanza Rodriguez Piceda : Conceptualization, Formal Analysis, Data curation, Investigation, Visualization, Writing - original draft, Writing - review & editing, Stephan V Sobolev: Methodology, Supervision, Validation, Writing - review & editing, Magdalena Scheck-Wenderoth : Methodology, Supervision, Validation, Writing - review &

editing, Manfred Strecker : Project administration, Funding acquisition, Supervision, Validation, Writing - review & editing

10. Supplementary information

Supplementary text S1, Supplementary figures 1 to 4.

11. References

Allmendinger, R. W., & Gubbels, T. (1996). Pure and simple shear plateau uplift, Altiplano-Puna, Argentina and Bolivia. *Tectonophysics*, *259*(1-3 SPEC. ISS.), 1-13. https://doi.org/10.1016/0040-1951(96)00024-8

Allmendinger, R. W., Jordan, T. E., Kay, S. M., & Isacks, B. L. (1997). The evolution of the Altiplano-Puna plateau of the Central Andes. *Annu Rev Earth Planet Sci*, *25*, 139-174. https://doi.org/10.1146/annurev.earth.25.1.139

Allmendinger, R. W., & Judge, P. A. (2014). The Argentine Precordillera : A foreland thrust belt proximal to the subducted plate. *Geosphere*, *10*(6), 1203-1218. https://doi.org/10.1130/GES01062.1

Allmendinger, R. W., Ramos, V. A., Jordan, T. E., Palma, M., & Isacks, B. L. (1983). Paleogeography and Andean structural geometry, northwest Argentina. *Tectonics*, *2*(1), 1-16. https://doi.org/10.1029/TC002i001p00001

Alvarado, P., Barrientos, S., Saez, M., Astroza, M., & Beck, S. (2009). Source study and tectonic implications of the historic 1958 Las Melosas crustal earthquake, Chile, compared to earthquake damage. *Physics of the Earth and Planetary Interiors*, *175*(1), 26-36. https://doi.org/10.1016/j.pepi.2008.03.015

Alvarado, P., Beck, S., & Zandt, G. (2007). Crustal structure of the south-central Andes Cordillera and backarc region from regional waveform modeling. *Geophysical Journal International*, *170*(2), 858-875. https://doi.org/10.1111/j.1365-246x.2007.03452.x

Amante, C., & Eakins, B. (2009). *ETOPO1 1 Arc-Minute Global Relief Model : Procedures, data sources and analysis*. https://doi.org/10.7289/V5C8276M

Ammirati, J. B., Alvarado, P., & Beck, S. (2015). A lithospheric velocity model for the flat slab region of Argentina from joint inversion of Rayleigh wave phase velocity dispersion and teleseismic receiver functions. *Geophysical Journal International*, *202*(1), 224. https://doi.org/10.1093/gji/ggv140

Ammirati, J.-B., Alvarado, P., Perarnau, M., Saez, M., & Monsalvo, G. (2013). Crustal structure of the Central Precordillera of San Juan, Argentina (31°S) using teleseismic receiver functions. *Journal of South American Earth Sciences*, *46*, 100-109. https://doi.org/10.1016/j.jsames.2013.05.007

Ammirati, J.-B., Venerdini, A., Alcacer, J. M., Alvarado, P., Miranda, S., & Gilbert, H. (2018). New insights on regional tectonics and basement composition beneath the eastern Sierras Pampeanas (Argentine back-arc region) from seismological and gravity data. *Tectonophysics*, *740-741*, 42-52. https://doi.org/10.1016/j.tecto.2018.05.015

Anikiev, D., Cacace, M., Bott, J., Gomez Dacal, M. L., & Scheck-Wenderoth, M. (2020). Influence of Lithosphere Rheology on Seismicity in an Intracontinental Rift : The Case of the Rhine Graben. *Frontiers in Earth Science*, *8*, 492. https://doi.org/10.3389/feart.2020.592561

Araneda, M., Asch, G., Bataille, K., Bohm, M., Bruhn, C., Giese, P., Lüth, S., Quezada, J., Rietbrock, A., & Wigger, P. (2003). A crustal model along 39° S from a seismic refraction profile-ISSA 2000. *Revista geológica de Chile*, *30*(1), 83-101. http://dx.doi.org/10.4067/S0716-02082003000100006

Assumpção, M., Feng, M., Tassara, A., & Julià, J. (2013). Models of crustal thickness for South America from seismic refraction, receiver functions and surface wave tomography. *Tectonophysics*, *609*, 82-96. https://doi.org/10.1016/j.tecto.2012.11.014

Axen, G. J., van Wijk, J. W., & Currie, C. A. (2018). Basal continental mantle lithosphere displaced by flat-slab subduction. *Nature Geoscience*, *11*(12), Art. 12. https://doi.org/10.1038/s41561-018-0263-9

Babeyko, A. Y., & Sobolev, S. V. (2005). Quantifying different modes of the late Cenozoic shortening in the central Andes. *Geology*, *33*(8), 621-624. https://doi.org/10.1130/G21126.1

Babeyko, A. Y., Sobolev, S. V., Vietor, T., Oncken, O., & Trumbull, R. B. (2006a). Numerical Study of Weakening Processes in the Central Andean Back-Arc. *The Andes - Active subduction orogeny*, 495-512. https://doi.org/10.1007/978-3-540-48684-8

Bangerth, W., Dannberg, J., Fraters, M., Gassmoeller, R., Glerum, A., Heister, T., & Naliboff, J. (2021). *ASPECT v2.3.0*. Zenodo. https://doi.org/10.5281/zenodo.5131909

Bangs, N. L., & Cande, S. C. (1997). Episodic development of a convergent margin inferred from structures and processes along the southern Chile margin. *Tectonics*, *16*(3), 489-503. https://doi.org/10.1029/97TC00494

Barazangi, M., & Isacks, B. L. (1976). Spatial distribution of earthquakes and subduction of the Nazca plate beneath South America. *Geology*, *4*(11), 686-692. https://doi.org/10.1130/0091-7613(1976)4<686:SDOEAS>2.0.CO;2

Barrionuevo, M., Liu, S., Mescua, J., Yagupsky, D., Quinteros, J., Giambiagi, L., Sobolev, S. V., Piceda, C. R., & Strecker, M. R. (2021). The influence of variations in crustal composition and lithospheric strength on the evolution of deformation processes in the southern Central Andes : Insights from geodynamic models. *International Journal of Earth Sciences 2021 110:7*, *110*(7), 2361-2384. https://doi.org/10.1007/S00531-021-01982-5

Becker, T. W., Schaeffer, A. J., Lebedev, S., & Conrad, C. P. (2015). Toward a generalized plate motion reference frame. *Geophysical Research Letters*, *42*(9), 3188-3196. https://doi.org/10.1002/2015GL063695

Bello-González, J. P., Contreras-Reyes, E., & Arriagada, C. (2018). Predicted path for hotspot tracks off South America since Paleocene times : Tectonic implications of ridge-trench collision along the Andean margin. *Gondwana Research*, *64*, 216-234. https://doi.org/10.1016/j.gr.2018.07.008

Bovy, B. (2021). *fastscape-lem/fastscape : Release v0.1.0beta3*. Zenodo. https://doi.org/10.5281/zenodo.4435110

Braun, J., & Willett, S. D. (2013). A very efficient O(n), implicit and parallel method to solve the stream power equation governing fluvial incision and landscape evolution. *Geomorphology*, *180-181*, 170-179. https://doi.org/10.1016/j.geomorph.2012.10.008

Briaud, A., Agrusta, R., Faccenna, C., Funiciello, F., & van Hunen, J. (2020). Topographic Fingerprint of Deep Mantle Subduction. *Journal of Geophysical Research: Solid Earth*, *125*(1), e2019JB017962. https://doi.org/10.1029/2019JB017962

Brocher, T. (2005). Empirical relations between elastic waves peeds and density in the Earth's crust. *Bull Seismol Soc Am*, *95*(6), 2081-2092. https://doi.org/10.1785/0120050077

Calignano, E., Sokoutis, D., Willingshofer, E., Gueydan, F., & Cloetingh, S. (2015). Strain localization at the margins of strong lithospheric domains : Insights from analog models. *Tectonics*, *34*(3), 396-412. https://doi.org/10.1002/2014TC003756

Casquet, C., Dahlquist, J. A., Verdecchia, S. O., Baldo, E. G., Galindo, C., Rapela, C. W., Pankhurst, R. J., Morales, M. M., Murra, J. A., & Mark Fanning, C. (2018). Review of the Cambrian Pampean orogeny of Argentina; a displaced orogen formerly attached to the Saldania Belt of South Africa? *Earth-Science Reviews*, *177*, 209-225. https://doi.org/10.1016/j.earscirev.2017.11.013

Cermak, V., & Rybach, L. (1982). 4.1.1 Introductory remarks. In G. Angenheister (Éd.), *Subvolume A: Vol. c* (p. 305-310). Springer-Verlag. https://doi.org/10.1007/10201894_62

Cerpa, N. G., Araya, R., Gerbault, M., & Hassani, R. (2015). Relationship between slab dip and topography segmentation in an oblique subduction zone : Insights from numerical modeling. *Geophysical Research Letters*, *42*(14), 5786-5795. https://doi.org/10.1002/2015GL064047

Chen, W.-P., & Molnar, P. (1983). Focal depths of intracontinental and intraplate earthquakes and their implications for the thermal and mechanical properties of the lithosphere. *Journal of Geophysical Research: Solid Earth*, *88*(B5), 4183-4214. https://doi.org/10.1029/JB088iB05p04183

Christensen, N. I., & Mooney, W. D. (1995). Seismic velocity structure and composition of the continental crust : A global view. *Journal of Geophysical Research: Solid Earth*, *100*(B6), 9761-9788. https://doi.org/10.1029/95JB00259

Čížková, H., & Bina, C. R. (2013). Effects of mantle and subduction-interface rheologies on slab stagnation and trench rollback. *Earth and Planetary Science Letters*, *379*, 95-103. https://doi.org/10.1016/j.epsl.2013.08.011

Contreras-Reyes, E., Grevemeyer, I., Flueh, E. R., & Reichert, C. (2008). Upper lithospheric structure of the subduction zone offshore of southern Arauco peninsula, Chile, at ∼38°S. *Journal of Geophysical Research*, *113*(B7), B07303. https://doi.org/10.1029/2007JB005569

Cordani, U., Pimentel, M., Ganade, C., & Fuck, R. (2013). The significance of the Transbrasiliano-Kandi tectonic corridor for the amalgamation of West Gondwana. *Brazilian Journal of Geology*, *43*, 583-597. https://doi.org/10.5327/Z2317-48892013000300012

Cristallini, E. O., & Ramos, V. A. (2000). Thick-skinned and thin-skinned thrusting in the La Ramada fold and thrust belt. *Tectonophysics*, *317*(3-4), 205-235. https://doi.org/10.1016/s0040-1951(99)00276-0

Dannberg, J., Eilon, Z., Faul, U., Gassmöller, R., Moulik, P., & Myhill, R. (2017). The importance of grain size to mantle dynamics and seismological observations. *Geochemistry, Geophysics, Geosystems*, *18*(8), 3034-3061. https://doi.org/10.1002/2017GC006944

Del Papa, C., Hongn, F., Powell, J., Payrola, P., Do Campo, M., Strecker, M. R., Petrinovic, I., Schmitt, A. K., & Pereyra, R. (2013). Middle Eocene-Oligocene broken-foreland evolution in the Andean Calchaqui Valley, NW Argentina : Insights from stratigraphic, structural and provenance studies. *Basin Research*, *25*(5), 574-593. https://doi.org/10.1111/BRE.12018

Dickinson, W. R., & Snyder, W. S. (1978). Plate tectonics of the Laramide orogeny. *Memoir of the Geological Society of America*, *151*, 355-366. https://doi.org/10.1130/MEM151-P355

Eisermann, J. O., Göllner, P. L., & Riller, U. (2021). Orogen-scale transpression accounts for GPS velocities and kinematic partitioning in the Southern Andes. *Communications Earth & Environment*, *2*(1), 167. https://doi.org/10.1038/s43247-021-00241-4

Erdős, Z., Huismans, R. S., & van der Beek, P. (2015). First-order control of syntectonic sedimentation on crustal-scale structure of mountain belts. *Journal of Geophysical Research: Solid Earth*, *120*(7), 5362-5377. https://doi.org/10.1002/2014JB011785

Fuentes, F., Horton, B. K., Starck, D., & Boll, A (2016). Structure and tectonic evolution of hybrid thick- and thin-skinned systems in the Malargüe fold-thrust belt, Neuquén basin, Argentina. *Geol Mag*, *153*(5-6), 1066-1084. https://doi.org/10.1017/s0016756816000583

Ibarra, F., Liu, S., Meeßen, C. (2019). 3D data-derived lithospheric structure of the Central Andes and its implications for deformation : Insights from gravity and geodynamic modelling. *Tectonophysics*, *766*, 453-468. https://doi.org/10.1016/j.tecto.2019.06.025

Faccenna, C., Becker, T. W., Holt, A. F., & Brun, J. P. (2021). Mountain building, mantle convection, and supercontinents : Holmes (1931) revisited. *Earth and Planetary Science Letters*, *564*.

Faccenna, C., Oncken, O., Holt, A. F., & Becker, T. W. (2017). Initiation of the Andean orogeny by lower mantle subduction. *Earth and Planetary Science Letters*, *463*, 189-201. https://doi.org/10.1016/J.EPSL.2017.01.041

Fairhead, J. D., & Maus, S. (2003). CHAMP satellite and terrestrial magnetic data help define the tectonic model for South America and resolve the lingering problem of the pre-break-up fit of the South Atlantic Ocean. *The Leading Edge*, *22*(8), 779-783. https://doi.org/10.1190/1.1605081

Fennell, L. M., Iannelli, S. B., Encinas, A., Naipauer, M., Valencia, V., & Folguera, A. (2019). Alternating contraction and extension in the Southern Central Andes (35°–37°S). *American Journal of Science*, *319*(5), 381-429. https://doi.org/10.2475/05.2019.02

Folguera, A., Naranjo, J. A., Orihashi, Y., Sumino, H., Nagao, K., Polanco, E., & Ramos, V. A. (2009). Retroarc volcanism in the northern San Rafael Block (34°-35°30'S), southern Central Andes : Occurrence, age, and tectonic setting. *Journal of Volcanology and Geothermal Research*, *186*(3-4), 169-185. https://doi.org/10.1016/J.JVOLGEORES.2009.06.012

Folguera, A., & Zárate, M. (2009). La sedimentación neógena continental en el sectorextrandino de Argentina central. *Revista de la Asociación Geológica Argentina*, *64*(4), 692-712.

Fraters, M. (2015). *Thermo-mechanically coupled subduction modelling with ASPECT Master ' s thesis by Menno Fraters*. *April*. https://doi.org/10.13140/RG.2.1.1061.0720

Gans, C. R., Beck, S. L., Zandt, G., Gilbert, H., Alvarado, P., Anderson, M., & Linkimer, L. (2011). Continental and oceanic crustal structure of the Pampean flat slab region, western Argentina, using receiver function analysis : New high-resolution results. *Geophysical Journal International*, *186*(1), 45-58. https://doi.org/10.1111/J.1365-246X.2011.05023.X

Giambiagi, L., Mescua, J., Bechis, F., Tassara, A., & Hoke, G. (2012). Thrust belts of the southern Central Andes : Along-strike variations in shortening, topography, crustal geometry, and denudation. *Bulletin of the Geological Society of America*, *124*(7-8), 1339-1351. https://doi.org/10.1130/B30609.1

Giambiagi, L., Mescua, J., Heredia, N., Farías, P., García-Sansegundo, J., Fernández, C., Stier, C., Pérez, D., Bechis, F., Moreiras, M., & Lossada, A. (2014). Reactivation of Paleozoic structures during Cenozoic deformation in the Cordón del Plata and Southern Precordillera ranges (Mendoza, Argentina). *Journal of Iberian Geology*, *40*(2). https://doi.org/10.5209/rev_JIGE.2014.v40.n2.45302

Gilbert, H., Beck, S., & Zandt, G. (2006a). Lithospheric and upper mantle structure of central Chile and Argentina. *Geophysical Journal International*, *165*(1), 383-398. https://doi.org/10.1111/J.1365-246X.2006.02867.X

Gilbert, H., Beck, S., & Zandt, G. (2006b). Lithospheric and upper mantle structure of central Chile and Argentina. *Geophysical Journal International*, *165*(1), 383-398. https://doi.org/10.1111/j.1365-246X.2006.02867.x

Gleason, G. C., & Tullis, J. (1995a). A flow law for dislocation creep of quartz aggregates determined with the molten salt cell. *Tectonophysics*, *247*(1-4), 1-23. https://doi.org/10.1016/0040-1951(95)00011-B

Gleason, G. C., & Tullis, J. (1995b). A flow law for dislocation creep of quartz aggregates determined with the molten salt cell. *Tectonophysics*, *247*(1-4), 1-23. https://doi.org/10.1016/0040-1951(95)00011-B

Glerum, A., Thieulot, C., Fraters, M., Blom, C., & Spakman, W. (2018). Nonlinear viscoplasticity in ASPECT: Benchmarking and applications to subduction. *Solid Earth*, *9*(2), 267-294. https://doi.org/10.5194/SE-9-267-2018

Goetze, C., & Evans, B. (1979). Stress and temperature in the bending lithosphere as constrained by experimental rock mechanics. *Geophysical Journal of the Royal Astronomical Society*, *59*(3), 463-478. https://doi.org/10.1111/J.1365-246X.1979.TB02567.X

González, G., Cembrano, J., Carrizo, D., Macci, A., & Schneider, H. (2003). The link between forearc tectonics and Pliocene–Quaternary deformation of the Coastal Cordillera, northern Chile. *Journal of South American Earth Sciences*, *16*(5), 321-342. https://doi.org/10.1016/S0895-9811(03)00100-7

Gutscher, M. A., Spakman, W., Bijwaard, H., & Engdahl, E. R. (2000). Geodynamics of flat subduction : Seismicity and tomographic constraints from the Andean margin. *Tectonics*, *19*(5), 814-833. https://doi.org/10.1029/1999TC001152

Gutscher, M.-A. (2018). Scraped by flat-slab subduction. *Nature Geoscience*, *11*(12), 889-890. https://doi.org/10.1038/s41561-018-0264-8

Hackney, R. I., Echtler, H. P., Franz, G., Götze, H.-J., Lucassen, F., Marchenko, D., Melnick, D., Meyer, U., Schmidt, S., Tašárová, Z., Tassara, A., & Wienecke, S. (2006). The Segmented Overriding Plate and Coupling at the South-Central Chilean Margin (36–42°S). In O. Oncken, G. Chong, G. Franz, P. Giese, H.-J. Götze, V. A. Ramos, M. R. Strecker, & P. Wigger (Éds.), *The Andes* (p. 355-374). Springer Berlin Heidelberg. https://doi.org/10.1007/978-3-540-48684-8_17

Haines, P. W., Hand, M., & Sandiford, M. (2001). Palaeozoic synorogenic sedimentation in central and northern Australia : A review of distribution and timing with implications for the evolution of intracontinental orogens. *Australian Journal of Earth Sciences*, *48*(6), 911-928. https://doi.org/10.1046/j.1440-0952.2001.00909.x

Hamza, V. M., & Vieira, F. P. (2012). Global distribution of the lithosphere-asthenosphere boundary : A new look. *Solid Earth*, *3*(2), 199-212. https://doi.org/10.5194/se-3-199-2012

Hasterok, D., & Chapman, D. (2011). Heat production and geotherms for the continental lithosphere. *Earth and Planetary Science Letters*, *307*(1-2), 59-70. https://doi.org/10.1016/j.epsl.2011.04.034

Hayes, G. P., Moore, G. L., Portner, D. E., Hearne, M., Flamme, H., Furtney, M., & Smoczyk, G. M. (2018). Slab2, a comprehensive subduction zone geometry model. *Science*, *362*(6410), 58-61. https://doi.org/10.1126/science.aat4723

He, L., Hu, S., Huang, S., Yang, W., Wang, J., Yuan, Y., & Yang, S. (2008). Heat flow study at the Chinese Continental Scientific Drilling site : Borehole temperature, thermal conductivity, and radiogenic heat production. *Journal of Geophysical Research*, *113*(B2), B02404. https://doi.org/10.1029/2007JB004958

Heister, T., Dannberg, J., Gassmöller, R., & Bangerth, W. (2017). High accuracy mantle convection simulation through modern numerical methods—II: realistic models and problems. *Geophys J Int*, *210*(2), 833-851. https://doi.org/10.1093/gji/ggx195

Hirth, G., & Kohlstedt, D. (2004). Rheology of the upper mantle and the mantle wedge : A view from the experimentalists. *Geophysical Monograph Series*, *138*, 83-105. https://doi.org/10.1029/138GM06

Hongn, F., Papa, C. del, Powell, J., Petrinovic, I., Mon, R., & Deraco, V. (2007). Middle Eocene deformation and sedimentation in the Puna-Eastern Cordillera transition (23°-26°S) : Control by preexisting heterogeneities on the pattern of initial Andean shortening. *Geology*, *35*(3), 271-274. https://doi.org/10.1130/G23189A.1

Horton, B. (2018). Tectonic regimes of the Central and Southern Andes : Responses to variations in plate coupling during subduction. *Tectonics*, *37*(2), 402-429. https://doi.org/10.1002/2017tc004624

Horton, B. K., Fuentes, F., Boll, A., Starck, D., Ramirez, S. G., & Stockli, D. F. (2016). Andean stratigraphic record of the transition from backarc extension to orogenic shortening : A case study from the northern Neuquén Basin, Argentina. *J S Am Earth Sci*, *71*, 17-40. https://doi.org/10.1016/j.jsames.2016.06.003

Husson, L., Conrad, C. P., & Faccenna, C. (2008). *Tethyan closure , Andean orogeny , and westward drift of the Paci fi c Basin*. *271*, 303-310. https://doi.org/10.1016/j.epsl.2008.04.022

Ibarra, F., Meeßen, C., Liu, S., Prezzi, C., & Sippel, J. (2018). *Density structure and rheology of northern Argentina : From the Central Andes to the foreland basin*. *20*(April), 16756-16756.

Ibarra, F., Prezzi, C. B., Bott, J., Scheck-Wenderoth, M., & Strecker, M. R. (2021). Distribution of Temperature and Strength in the Central Andean Lithosphere and Its Relationship to Seismicity and Active Deformation. *Journal of Geophysical Research: Solid Earth*, *126*(5). https://doi.org/10.1029/2020JB021231

Introcaso, A., & Ruiz, F. (2001). Geophysical indicators of Neogene strike-slip faulting in the Desaguadero–Bermejo tectonic lineament (northwestern Argentina). *Journal of South American Earth Sciences*, *14*(7), 655-663. https://doi.org/10.1016/S0895-9811(01)00057-8

Isacks, B. (1988). Uplift of the Central Andean Plateau and bending of the Bolivian Orocline. *J Geophys Res*, *93*(B4), 3211. https://doi.org/10.1029/jb093ib04p03211

Isacks, B., Jordan, T., Allmendinger, R., & Ramos, V. (1982). La segmentación tectónica de los Andes Centrales y su relación con la Placa de Nazca subductada. *Congreso Latinoamericano de Geología*, *5*, 587-606.

Jammes, S., & Huismans, R. S. (2012). Structural styles of mountain building : Controls of lithospheric rheologic stratification and extensional inheritance. *Journal of Geophysical Research: Solid Earth*, *117*(B10). https://doi.org/10.1029/2012JB009376

Jordan, T. E., & Allmendinger, R. W. (1986). The Sierras Pampeanas of Argentina : A modern analogue of Rocky Mountain foreland deformation. *American Journal of Science*, *286*(10), 737-764. https://doi.org/10.2475/AJS.286.10.737

Jordan, T. E., Allmendinger, R. W., Damanti, J. F., & Drake, R. E. (1993). Chronology of motion in a complete thrust belt : The Precordillera, 30-31°S, Andes Mountains. *Journal of Geology*, *101*(2), 135-156. https://doi.org/10.1086/648213

Jordan, T. E., Isacks, B. L., Ramos, V. A., & Allmendinger, R. W. (1983). Mountain building in the central Andes. *Episodes*, *1983*(3), 20-26. https://doi.org/10.18814/EPIIUGS/1983/V6I3/005

Jordan, T. E., Ramos, V. A. ,. Allmendinger, R. W. ,. &. Isacks, B. L. (1984). *Andean tectonics related to geometry of subducted Nazca plate : Discussion and reply : Reply*. *July*, 877-880. https://doi.org/10.1130/0016-7606(1984)95<877

Kay, S. M. (1991). Magma source variations for mid-late Tertiary magmatic rocks associated with a shallowing subduction zone and a thickening crust in the central Andes (28 to 33°S). *pecial Paper of the Geological Society of America*, *265*, 113-137. http://dx.doi.org/10.1130/SPE265-p113

Kay, S. M., & Abbruzzi, J. M. (1996). Magmatic evidence for Neogene lithospheric evolution of the central Andean « flat-slab » between 30°S and 32°S. *Tectonophysics*, *259*(1-3 SPEC. ISS.), 15-28. https://doi.org/10.1016/0040-1951(96)00032-7

Kay, S. M., Maksaev, V., Moscoso, R., Mpodozis, C., & Nasi, C. (1987). Probing the evolving Andean Lithosphere : Mid-Late Tertiary magmatism in Chile (29°–30°30'S) over the modern zone of subhorizontal subduction. *Journal of Geophysical Research: Solid Earth*, *92*(B7), 6173-6189. https://doi.org/10.1029/JB092iB07p06173

Kley, J. (1999). Geologic and geometric constraints on a kinematic model of the Bolivian orocline. *Journal of South American Earth Sciences*, *12*(2), 221-235. https://doi.org/10.1016/S0895-9811(99)00015-2

Kley, J., & Monaldi, C. R. (1998). Tectonic shortening and crustal thickness in the Central Andes : How good is the correlation-? *Geology*, *26*(8), 723-726. https://doi.org/10.1130/0091-7613(1998)026<0723:TSACTI>2.3.CO;2

Kley, J., & Monaldi, C. R. (2002). Tectonic inversion in the Santa Barbara System of the central Andean foreland thrust belt, northwestern Argentina. *Tectonics*, *21*(6), 11-1-11-18. https://doi.org/10.1029/2002TC902003

Kley, J., Monaldi, C. R., & Salfity, J. A. (1999). Along-strike segmentation of the Andean foreland : Causes and consequences. *Tectonophysics*, *301*(1-2), 75-94. https://doi.org/10.1016/S0040-1951(98)90223-2

Kley, J., & Monaldi, C. R. (2002). Tectonic inversion in the Santa Barbara System of the central Andean foreland thrust belt, northwestern Argentina. *Tectonics*, *21*(6), 1-18. https://doi.org/10.1029/2002tc902003

Kronbichler, M., Heister, T., & Bangerth, W. (2012). High accuracy mantle convection simulation through modern numerical methods. *Geophys J Int*, *191*(1), 12-29. https://doi.org/10.1111/j.1365-246x.2012.05609.x

Lallemand, S., Heuret, A., Faccenna, C., & Funiciello, F. (2008). Subduction dynamics as revealed by trench migration. *Tectonics*, *27*(3). https://doi.org/10.1029/2007TC002212

Lamb, S., & Davis, P. (2003). Cenozoic climate change as a possible cause for the rise of the Andes. *Nature*, *425*(6960), 792-797. https://doi.org/10.1038/NATURE02049

Liu, S., & Currie, C. A. (2016). Farallon plate dynamics prior to the Laramide orogeny : Numerical models of flat subduction. *Tectonophysics*, *666*, 33-47. https://doi.org/10.1016/J.TECTO.2015.10.010

Liu, S., Sobolev, S. V., Babeyko, A. Y., & Pons, M. (2022). Controls of the Foreland Deformation Pattern in the Orogen-Foreland Shortening System : Constraints From High-Resolution Geodynamic Models. *Tectonics*, *41*(2). https://doi.org/10.1029/2021TC007121

Lossada, A., Giambiagi, L., Hoke, G., AU, & Suriano, J. (2017). *Cenozoic Uplift and Exhumation of the Frontal Cordillera Between 30° and 35° S and the Influence of the Subduction Dynamics in the Flat Slab Subduction Context, South Central Andes*. https://doi.org/10.1007/978-3-319-67774-3_16

Marot, M., Monfret, T., Gerbault, M., Nolet, G., Ranalli, G., & Pardo, M. (2014). Flat versus normal subduction zones : A comparison based on 3-D regional traveltime tomography and petrological modelling of central Chile and western Argentina (29°–35°S). *Geophys J Int*, *199*(3), 1633-1654. https://doi.org/10.1093/gji/ggu355

Mackwell, S. J., Zimmerman, M. E., & Kohlstedt, D. L. (1998a). High-temperature deformation of dry diabase with application to tectonics on Venus. *Journal of Geophysical Research: Solid Earth*, *103*(1), 975-984. https://doi.org/10.1029/97JB02671

Mackwell, S. J., Zimmerman, M. E., & Kohlstedt, D. L. (1998b). High-temperature deformation of dry diabase with application to tectonics on Venus. *Journal of Geophysical Research: Solid Earth*, *103*(1), 975-984. https://doi.org/10.1029/97JB02671

Mahlburg Kay, S., & Mpodozis, C. (2002). Magmatism as a probe to the Neogene shallowing of the Nazca plate beneath the modern Chilean flat-slab. *Journal of South American Earth Sciences*, *15*(1), 39-57. https://doi.org/10.1016/S0895-9811(02)00005-6

Manceda, R., & Figueroa, D. (1995). *Inversion of the Mesozoic Neuquén rift in the Malargüe fold and thrust belt, Mendoza, Argentina*.

Mareschal, J.-C., & Jaupart, C. (2011). Energy Budget of the Earth. In H. K. Gupta (Éd.), *Encyclopedia of Solid Earth Geophysics* (p. 285-291). Springer Netherlands. https://doi.org/10.1007/978-90-481-8702-7_64

Martinod, J., Gérault, M., Husson, L., & Regard, V. (2020). Widening of the Andes : An interplay between subduction dynamics and crustal wedge tectonics. *Earth-Science Reviews*, *204*, 103170. https://doi.org/10.1016/j.earscirev.2020.103170

Martinod, J., Husson, L., Roperch, P., Guillaume, B., & Espurt, N. (2010). Horizontal subduction zones, convergence velocity and the building of the Andes. *Earth and Planetary Science Letters*, *299*(3-4), 299-309. https://doi.org/10.1016/j.epsl.2010.09.010

McGroder, M. F., Lease, R. O., & Pearson, D. M. (2015). Along-strike variation in structural styles and hydrocarbon occurrences, Subandean fold-and-thrust belt and inner foreland, Colombia to Argentina. *Memoir of the Geological Society of America*, *212*, 79-113. https://doi.org/10.1130/2015.1212(05)

Melnick, D., Charlet, F., Echtler, H. P., & De Batist, M. (2006). Incipient axial collapse of the Main Cordillera and strain partitioning gradient between the central and Patagonian Andes, Lago Laja, Chile. *Tectonics*, *25*(5). https://doi.org/10.1029/2005TC001918

Mescua, J. F., Giambiagi, L. B., Tassara, A., Gimenez, M., & Ramos, V. A. (2014). Influence of pre-Andean history over Cenozoic foreland deformation : Structural styles in the Malargüe fold-and-thrust belt at 35 S, Andes of Argentina. *Geosphere*, *10*(3), 585-609. https://doi.org/10.1130/GES00939.1

Mescua, J. F., Giambiagi, L., Barrionuevo, M., Tassara, A., Mardonez, D., Mazzitelli, M., & Lossada, A. (2016). Basement composition and basin geometry controls on upper-crustal deformation in the Southern Central Andes (30-36°S). *Geological Magazine*, *153*(5-6), 945-961. https://doi.org/10.1017/S0016756816000364

Molnar, P., & Tapponnier, P. (1975). Cenozoic Tectonics of Asia : Effects of a Continental Collision. *Science*, *189*(4201), 419-426. https://doi.org/10.1126/science.189.4201.419

Mon, R., & Salfity, J. (1995). Tectonic evolution of the Andes of northern Argentina. In *Petroleum Basins of South America* (Vol. 62). AAPG Special Volumes.

Mouthereau, F., Watts, A. B., & Burov, E. (2013). Structure of orogenic belts controlled by lithosphere age. *Nat Geosci*, *6*(9), 785-789. https://doi.org/10.1038/ngeo1902

Mpodozis, C., & Kay, S. M. (1990). Provincias magmáticas ácidas y evolución tectónica de Gondwana : Andes chilenos (28-31 S). *Andean Geology*, *17*(2), 153-180. http://dx.doi.org/10.5027/andgeoV17n2-a03

Muldashev, I. A., & Sobolev, S. V. (2020). What Controls Maximum Magnitudes of Giant Subduction Earthquakes? *Geochemistry, Geophysics, Geosystems*, *21*(9). https://doi.org/10.1029/2020GC009145

Murnaghan, F. D. (1944). The Compressibility of Media under Extreme Pressures. *Proceedings of the National Academy of Sciences*, *30*(9), 244-247. https://doi.org/10.1073/pnas.30.9.244

Neuharth, D., Brune, S., Glerum, A. C., Morley, C. K., Yuan, X., & Braun, J. (2021). *Flexural strike-slip basins*. https://eartharxiv.org/repository/view/2439/

Oncken, O., Hindle, D., Kley, J., Elger, K., Victor, P., & Schemmann, K. (2006). Deformation of the central Andean upper plate system—Facts, fiction, and constraints for plateau models. In *The Andes* (pp. 3-27). Springer, Berlin, Heidelberg.

Oncken, O., Boutelier, D., Dresen, G., & Schemmann, K. (2012). Strain accumulation controls failure of a plate boundary zone : Linking deformation of the Central Andes and lithosphere mechanics. *Geochemistry, Geophysics, Geosystems*, *13*(12). https://doi.org/10.1029/2012GC004280

Ortiz, G., Stevens Goddard, A. L., Fosdick, J. C., Alvarado, P., Carrapa, B., & Cristofolini, E. (2021). Fault reactivation in the Sierras Pampeanas resolved across Andean extensional and compressional regimes using thermochronologic modeling. *Journal of South American Earth Sciences*, *112*, 103533. https://doi.org/10.1016/j.jsames.2021.103533

Pearson, D. M., Kapp, P., DeCelles, P. G., Reiners, P. W., Gehrels, G. E., Ducea, M. N., & Pullen, A. (2013). Influence of pre-Andean crustal structure on Cenozoic thrust belt kinematics and shortening magnitude : Northwestern Argentina. *Geosphere*, *9*(6), 1766-1782. https://doi.org/10.1130/GES00923.1

Pesicek, J. D., Engdahl, E. R., Thurber, C. H., DeShon, H. R., & Lange, D. (2012). Mantle subducting slab structure in the region of the 2010 M8.8 Maule earthquake (30-40°S), Chile : Mantle subducting slab structure in Chile. *Geophysical Journal International*, *191*(1), 317-324. https://doi.org/10.1111/j.1365-246X.2012.05624.x

Pilger Jr, R. H. (1981). Plate reconstructions, aseismic ridges, and low-angle subduction beneath the Andes. *GSA Bulletin*, *92*(7), 448-456. https://doi.org/10.1130/0016-7606(1981)92<448:PRARAL>2.0.CO;2

Pons, M., Sobolev, S. V., Liu, S., & Neuharth, D. (2022). Hindered Trench Migration Due To Slab Steepening Controls the Formation of the Central Andes. *Journal of Geophysical Research: Solid Earth*, *127*(12), e2022JB025229. https://doi.org/10.1029/2022JB025229

Ramos, V. (2010). The Grenville-age basement of the Andes. *J S Am Earth Sci*, *29*(1), 77-91. https://doi.org/10.1016/j.jsames.2009.09.004

Ramos, V. A., Cristallini, E. O., & Pérez, D. J. (2002a). The Pampean flat-slab of the Central Andes. *Journal of South American Earth Sciences*, *15*(1), 59-78. https://doi.org/10.1016/s0895-9811(02)00006-8

Ramos, V. A., Cristallini, E. O., & Pérez, D. J. (2002b). The Pampean flat-slab of the Central Andes. *Journal of South American Earth Sciences*, *15*(1), 59-78. https://doi.org/10.1016/S0895-9811(02)00006-8

Ramos, V. A., & Folguera, A. (2009). Andean flat-slab subduction through time. *Geological Society Special Publication*, *327*, 31-54. https://doi.org/10.1144/SP327.3

Ramos, V. A., & Scientific, N. (2002). Flat-slab subduction in the Andes. *Journal of South American Earth Sciences*, *15*(1), 1-2. https://doi.org/10.1016/s0895-9811(02)00011-1

Ranalli, G. (1997). Rheology and deep tectonics. *Annals of Geophysics*, *40*(3), 3. https://doi.org/10.4401/ag-3893

Regard, V., Saillard, M., Martinod, J., Audin, L., Carretier, S., Pedoja, K., Riquelme, R., Paredes, P., & Hérail, G. (2010). Renewed uplift of the Central Andes Forearc revealed by coastal evolution during the Quaternary. *Earth and Planetary Science Letters*, *297*(1), 199-210. https://doi.org/10.1016/j.epsl.2010.06.020

Rodriguez Piceda, C., Scheck Wenderoth, M., Gomez Dacal, M. L., Bott, J., Prezzi, C. B., & Strecker, M. R. (2020). Lithospheric density structure of the southern Central Andes constrained by 3D data-integrative gravity modelling. *International Journal of Earth Sciences 2020 110:7*, *110*(7), 2333-2359. https://doi.org/10.1007/S00531-020-01962-1

Rodriguez Piceda, C., Scheck Wenderoth, M., Gomez Dacal, M. L., Bott, J., Prezzi, C. B., & Strecker, M. R. (2021). Lithospheric density structure of the southern Central Andes constrained by 3D data-integrative gravity modelling. *International Journal of Earth Sciences*, *110*(7), 2333-2359. https://doi.org/10.1007/S00531-020-01962-1

Rodriguez Piceda, C., Scheck-Wenderoth, M., Bott, J., Gomez Dacal, M. L., Cacace, M., Pons, M., Prezzi, C. B., & Strecker, M. R. (2022). Controls of the Lithospheric Thermal Field of an Ocean-Continent Subduction Zone : The Southern Central Andes. *Lithosphere*, *2022*(1), 2237272. https://doi.org/10.2113/2022/2237272

Rodriguez Piceda, C., Scheck-Wenderoth, M., Cacace, M., Bott, J., & Strecker, M. R. (2022). Long-Term Lithospheric Strength and Upper-Plate Seismicity in the Southern Central Andes, 29°–39°S. *Geochemistry, Geophysics, Geosystems*, *23*(3), 22. https://doi.org/10.1029/2021GC010171

Rose, I., Buffett, B., & Heister, T. (2017). Stability and accuracy of free surface time integration in viscous flows. *Physics of the Earth and Planetary Interiors*, *262*, 90-100. https://doi.org/10.1016/J.PEPI.2016.11.007

Rosenau, M., Melnick, D., & Echtler, H. (2006). Kinematic constraints on intra-arc shear and strain partitioning in the southern Andes between 38°S and 42°S latitude. *Tectonics*, *25*(4). https://doi.org/10.1029/2005TC001943

Scarfi, L., & Barbieri, G. (2019). New insights on the tectonic structure of the Southern Central Andes – Western Argentina – from seismic tomography. *Geology, Earth & Marine Sciences*, *1*(1). https://doi.org/10.31038/GEMS.2019113

Schaeffer, A., & Lebedev, S. (2013). Global shear speed structure of the upper mantle and transition zone. *Geophysical Journal International*, *194*(1), 417-449.

Sdrolias, M., & Müller, R. D. (2006). Controls on back-arc basin formation. *Geochemistry, Geophysics, Geosystems*, *7*(4). https://doi.org/10.1029/2005GC001090

Sippel, J., Meeßen, C., Cacace, M., Mechie, J., Fishwick, S., Heine, C., Scheck-Wenderoth, M., & Strecker, M. R. (2017). The Kenya rift revisited : Insights into lithospheric strength through data-driven 3-D gravity and thermal modelling. *Solid Earth*, *8*(1), 45-81. https://doi.org/10.5194/se-8-45-2017

Sobolev, S. V., & Babeyko, A. Y. (1994). Modeling of mineralogical composition, density and elastic wave velocities in anhydrous magmatic rocks. *Surveys in Geophysics*, *15*(5), 515-544. https://doi.org/10.1007/BF00690173

Sobolev, S. V., & Babeyko, A. Y. (2005). What drives orogeny in the Andes? *Geology*, *33*(8), 617-620. https://doi.org/10.1130/G21557.1

Sobolev, S. V., Babeyko, A. Y., Koulakov, I., & Oncken, O. (2006). Mechanism of the Andean Orogeny : Insight from Numerical Modeling. In *The Andes* (p. 513-535). Springer Berlin Heidelberg. https://doi.org/10.1007/978-3-540-48684-8_25

Stalder, N. F., Herman, F., Fellin, M. G., Coutand, I., Aguilar, G., Reiners, P. W., & Fox, M. (2020). The relationships between tectonics, climate and exhumation in the Central Andes (18–36°S) : Evidence from low-temperature thermochronology. *Earth-Science Reviews*, *210*, 103276. https://doi.org/10.1016/j.earscirev.2020.103276

Stüwe, K. (2007). *Geodynamics of the Lithosphere*. Springer-Verlag Berlin Heidelberg.

Tassara, A. (2005). Interaction between the Nazca and South American plates and formation of the Altiplano–Puna plateau : Review of a flexural analysis along the Andean margin (15°–34°S). *Andean Geodynamics:*, *399*(1), 39-57. https://doi.org/10.1016/j.tecto.2004.12.014

Tassara, A., & Yáñez, G. (2003). Relación entre el espesor elástico de la litosfera y la segmentación tectónica del margen andino (15-47°S). *Revista geológica de Chile*, *30*(2), 159-186. https://doi.org/10.4067/S0716-02082003000200002

Tesauro, M., Kaban, M. K., & Mooney, W. D. (2015). Variations of the lithospheric strength and elastic thickness in North America : Lithospheric Strength and Te variations. *Geochemistry, Geophysics, Geosystems*, *16*(7), 2197-2220. https://doi.org/10.1002/2015GC005937

Uliana, M. A., Arteaga, M. E., Legarreta, L., Cerdán, J. J., & Peroni, G. O. (1995). Inversion structures and hydrocarbon occurrence in Argentina. *Geological Society, London, Special Publications*, *88*(1), 211-233. https://doi.org/10.1144/GSL.SP.1995.088.01.13

Uyeda, S., & Kanamori, H. (1979). Back-arc opening and the mode of subduction. *Journal of Geophysical Research: Solid Earth*, *84*(B3), 1049-1061. https://doi.org/10.1029/JB084iB03p01049

van Keken, P. E., Wada, I., Sime, N., & Abers, G. A. (2019). Thermal Structure of the Forearc in Subduction Zones : A Comparison of Methodologies. *Geochemistry, Geophysics, Geosystems*, *20*(7), 3268-3288. https://doi.org/10.1029/2019GC008334

Vietor, T., & Echtler, H. (2006). Episodic Neogene Southward Growth of the Andean Subduction Orogen between 30°S and 40°S — Plate Motions, Mantle Flow, Climate, and Upper-Plate Structure. In O. Oncken, G. Chong, G. Franz, P. Giese, H.-J. Götze, V. A. Ramos, M. R. Strecker, & P. Wigger (Éds.), *The Andes* (p. 375-400). Springer Berlin Heidelberg. https://doi.org/10.1007/978-3-540-48684-8_18

Völker, D., Geersen, J., Contreras-Reyes, E., & Reichert, C. (2013). Sedimentary fill of the Chile Trench (32–46°S) : Volumetric distribution and causal factors. *Journal of the Geological Society*, *170*(5), 723-736. https://doi.org/10.1144/jgs2012-119

Wada, I., & Wang, K. (2009). Common depth of slab-mantle decoupling : Reconciling diversity and uniformity of subduction zones. *Geochemistry, Geophysics, Geosystems*, *10*(10). https://doi.org/10.1029/2009GC002570

Wagner, L. S., Beck, S., & Zandt, G. (2005). Upper mantle structure in the south central Chilean subduction zone (30° to 36°S). *Journal of Geophysical Research: Solid Earth*, *110*(B1). https://doi.org/10.1029/2004JB003238

Wimpenny, S. (2022). Weak, Seismogenic Faults Inherited From Mesozoic Rifts Control Mountain Building in the Andean Foreland. *Geochemistry, Geophysics, Geosystems*, *23*(3), e2021GC010270. https://doi.org/10.1029/2021GC010270

Xu, Y., Shankland, T. J., Linhardt, S., Rubie, D. C., Langenhorst, F., & Klasinski, K. (2004). Thermal diffusivity and conductivity of olivine, wadsleyite and ringwoodite to 20 GPa and 1373 K. *Physics of the Earth and Planetary Interiors*, *143-144*, 321-336. https://doi.org/10.1016/j.pepi.2004.03.005

Yáñez, G. A., Ranero, C. R., Von Huene, R., & Díaz, J. (2001). Magnetic anomaly interpretation across the southern central Andes (32°-34°S) : The role of the Juan Fernández Ridge in the late Tertiary evolution of the margin. *Journal of Geophysical Research: Solid Earth*, *106*(B4), 6325-6345. https://doi.org/10.1029/2000JB900337

Tectonics

Supporting Information for

Localization of deformation in a non-collisional subduction orogen: the roles of dip geometry and plate strength on the evolution of the broken Andean foreland, Sierras Pampeanas, Argentina

*,**Michaël Pons (1,2), Constanza Rodriguez Piceda* (1,2,3), Stephan V. Sobolev (1.2), Magdalena Scheck-Wenderoth (1,4), Manfred Strecker (1)

(1) Universität Potsdam, Institut für Geowissenschaften, Germany

(2) Helmholtz-Zentrum Potsdam GFZ - Deutsches GeoForschungsZentrum, Germany

(3) Plymouth University, School of Geography Earth and Environmental Sciences, United Kingdom

(4) RWTH Aachen University, Aachen, Germany

*these authors contributed equally to this work

** Corresponding author: Michaël Pons (ponsm@gfz-potsdam.com)

Contents of this file

Text S1

Figures S1 to S4

Introduction

This file includes a comparison between the topography resulting from the model and the real topography **(Text S1, Figure S1**). Additionally, the file includes the supplementary figures mentioned in the main text **(Figure S2 to S4).**

Text S1. Checking model densities

One advantage of implementing the data-driven model of Rodriguez Piceda et al. (2021) into a geodynamic simulation is the possibility of testing the evolution of topography as a response to the imposed structural and density configuration (Figure S1b). The thickness, geometry and density of the lithospheric layers were obtained by integration of geological and geophysical data and testing with the gravity field. Then, the densities were inferred with the gravity using an iterative forward modelling approach. The residual gravity (Figure S1d) indicates a good fit between the lithospheric model and the gravity. Using the average temperature for each layer we recalculated their average reference density (Table 1). Subsequently we ran a geodynamic model, without prescribing any velocity and let the model re-equilibrate. The topography is smoothed with a moving filter with a radius of ~50 km in order to avoid local strong topographic gradients (Figure S1b). After 100ka, we calculate the residual topography by subtracting the model to the present-day topography (Figure S1e). The residual topography indicates a consistency in the area covered by data. Whereas the modelled topography is underestimated on the eastern border (+1 km) and overestimated locally at the trench (-1km). The orogenic domain is close to the present-day topography and range between ($\pm$ 0.5 km). Variations on the east suggest that thickness of the layers may vary far from the orogen where additional data are required.

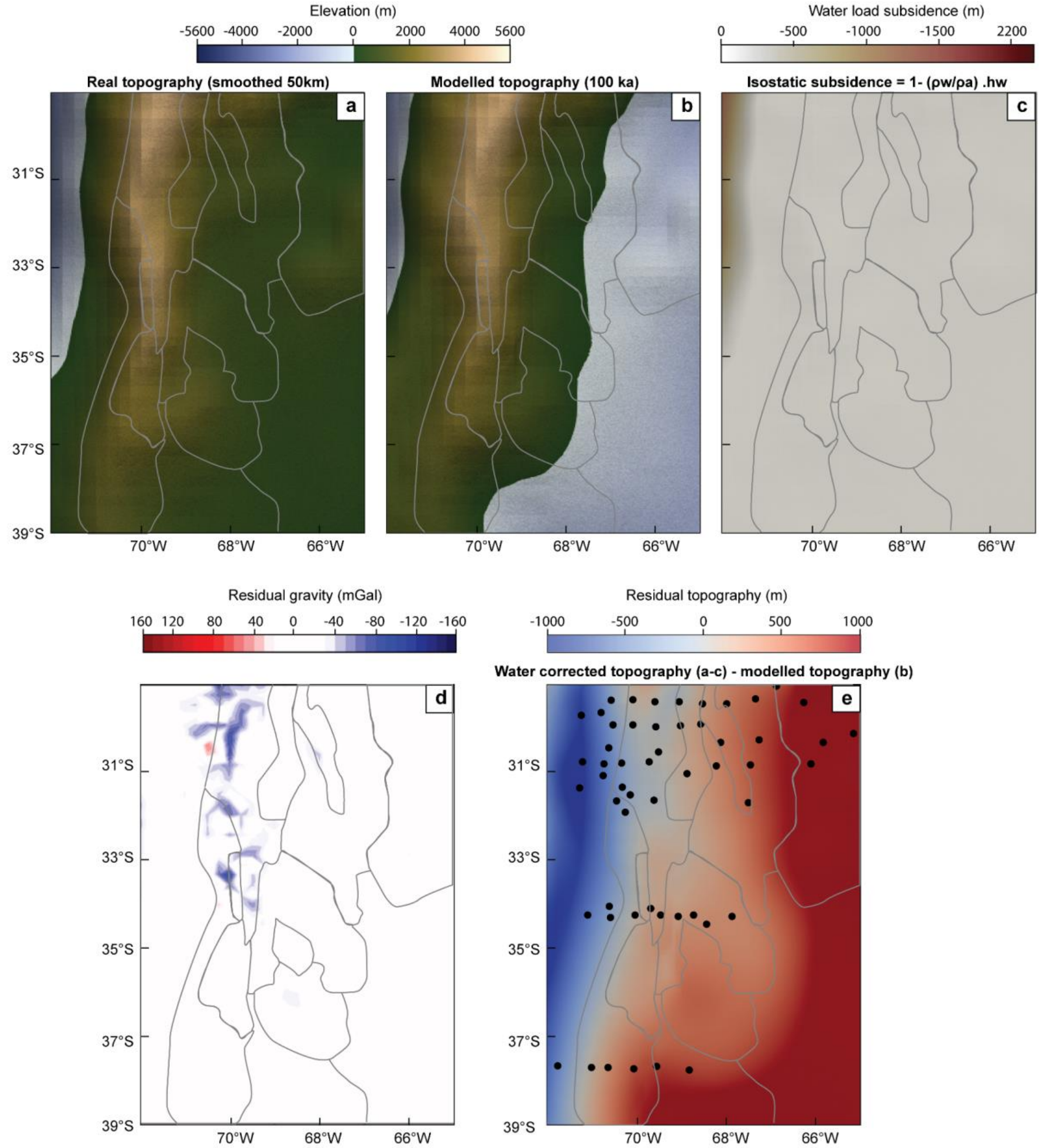

Figure S1 Comparison between the modelled and the real topography. **a** Real topography smoothed with a radial filter of 50 km. **b** Topography altered after 100 kyr of model time. **c** Isostatic contribution of the sea water. **d** Residual gravity of the density model (modified from Rodriguez Piceda et al., 2021). **e** Residual topography. Black circles illustrate local data of the crustal thickness (see references in Rodriguez Piceda et al., 2021). Grey lines denote the boundaries between morphotectonic provinces.

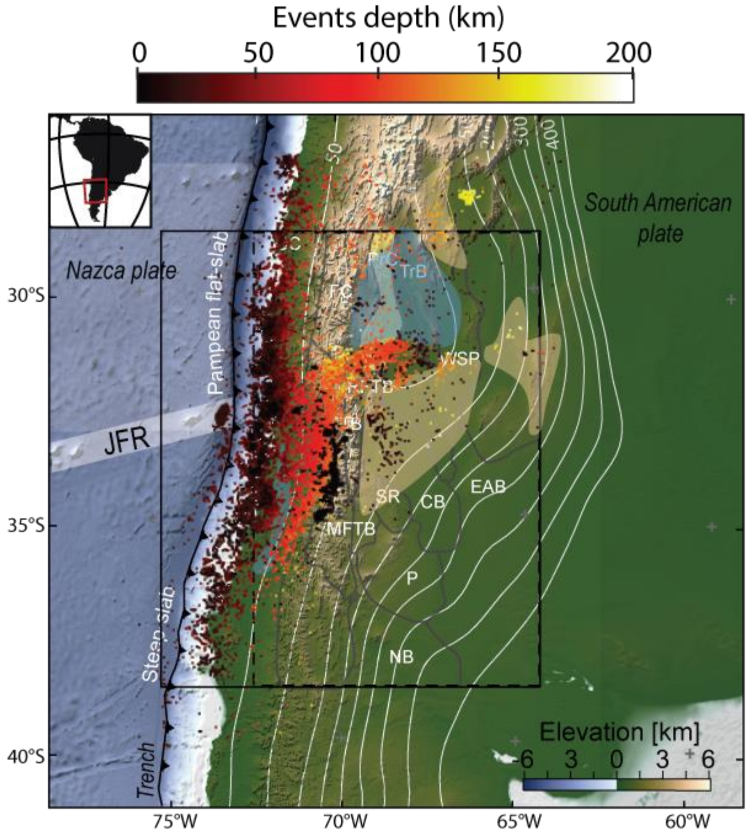

Figure S2 Distribution of seismic events in the Sierras Pampeanas (International Seismological Centre, 2021; Lentas et al., 2019). Few events are recorded on the top of the flat-slab (blue area) compared to the East and South front and the South front (orange area). JFR corresponds to the Juan Fernandez hotspot ridge. A greater density of events occurs in line with the inland extension of the ridge. Also shown are: the extent of the modelled area (black rectangle), the isobaths of the top of the slab (white lines, Hayes et al., 2018), and the boundaries between morphotectonic provinces (grey lines). The labels of these provinces are defined in Figure 1.

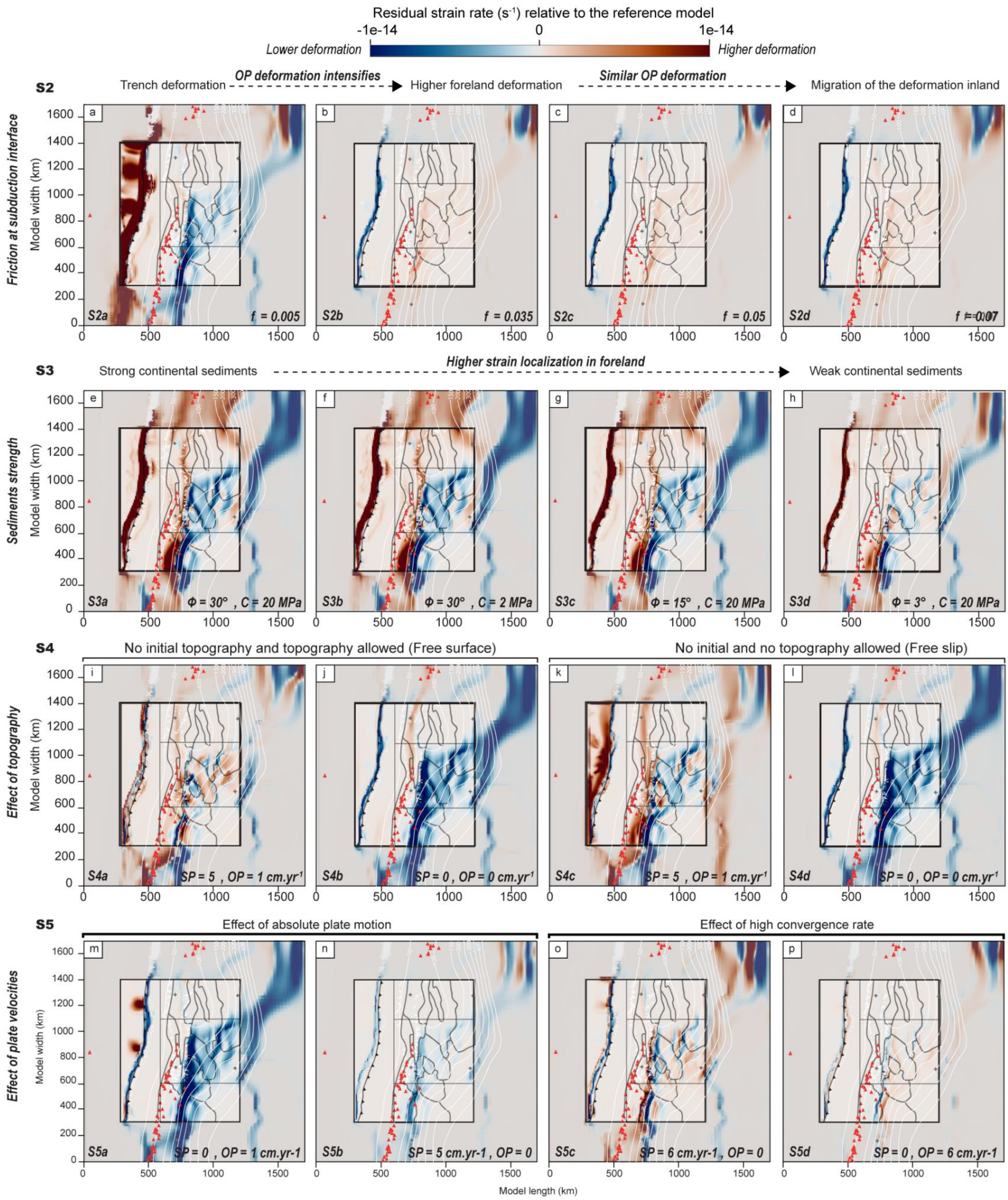

Figure S3 Residual obtained by subtracting the Reference model S1 to the model variants. Black squares delimit the deformational domains (e.g. Trench, flat subduction, shallow subduction and steep subduction). Blue and red colors indicate smaller or higher rate of deformation than in the reference model, respectively.

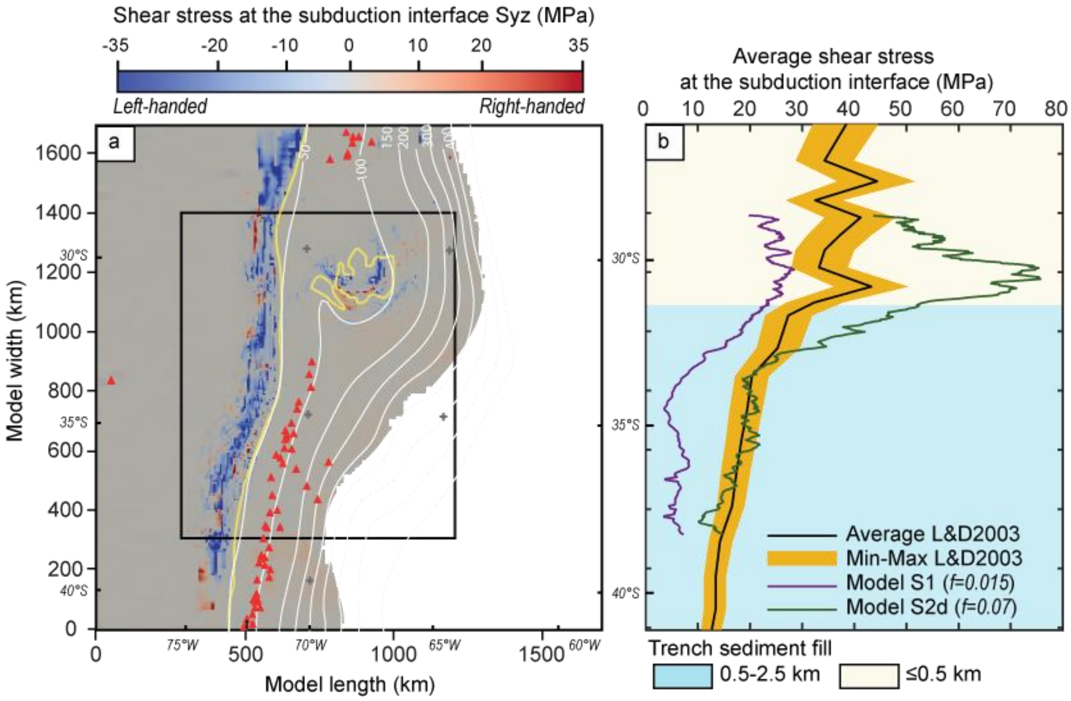

Figure S4 Shear stress at subduction interface**. a** Shear stress (Syz - pressure) from the reference model. Isobaths of the slab (in white, Hayes et al., 2018) and volcanic edifices (red triangles) are represented. The yellow lines indicate the brittle-ductile transition. **b** Modelled shear stress (models S1 and S2d) averaged at each latitude over a plate-interface depth of 120 km and compared to previous estimates by Lamb & Davis (2003, L&D2003).